Chapter 5

Results and Discussion for Steady Measurements

5.1 Steady Skin-Friction Measurements

5.1.1 Data Acquisition and Reduction

A Labview software program was developed for the acquisition of the steady skin-friction data. This software program was used to obtain the raw voltage values from the constant temperature anemometers, each connected to a hot-film sensor mounted on the model surface. In order get a single steady skin-friction C_f value, 10 seconds of voltage data were acquired at a sampling rate of 500 Hz. This gave a total number of 5000 samples per one skin-friction value.

The steady values that were measured or calculated can be defined as arrays of indexed variables for the description of the steady data reduction process. For instance, the voltage value acquired from each anemometer can be written as:

$$E = E(\alpha_j, s_k, \phi_m) \tag{5.1}$$

$$j = 1, ..., 14 \qquad k = 1, ..., 15 \qquad and \qquad m = 1, ..., nroll \tag{5.2}$$

where α_j corresponds to each steady angle of attack; s_k to the sensor number or location; and ϕ_m to the roll angle position of the model. The total number of roll angles $nroll$ is

56 for the barebody case and 117 for the sail-on-side case.

The steps followed during the steady skin-friction data reduction process can be described in the items below:

1. For each roll position and angle of attack, the voltage data of the free-stream temperature $T(\alpha_j, \phi_m)$, the dynamic pressure $q(\alpha_j, \phi_m)$, and the atmospheric pressure $p(\alpha_j, \phi_m)$ are converted to actual values by using the calibration factors.

2. The wall shear stress $\tau_w(\alpha_j, s_k, \phi_m)$ is calculated by using King's Law (equation 4.10) for each sensor, at each angle of attack and model roll position:

$$\tau_w(\alpha_j, s_k, \phi_m) = \left[\frac{E^2(\alpha_j, s_k, \phi_m) - A(s_k, \phi_m)}{B(s_k, \phi_m)}\right]^3 \tag{5.3}$$

   $A(s_k, \phi_m)$ and $B(s_k, \phi_m)$ are the calibration coefficients obtained for each sensor at each roll angle position of the model. The skin-friction coefficient $C_f(\alpha_j, s_k, \phi_m)$ can be calculated simply by dividing the wall shear stress by the dynamic pressure:

$$C_f(\alpha_j, s_k, \phi_m) = \frac{\tau_w(\alpha_j, s_k, \phi_m)}{q(\alpha_j, \phi_m)} \tag{5.4}$$

3. Before the determination of the separation locations, $C_f = C_f(\alpha_j, s_k, \phi_m)$ vs. $\phi = \phi_m$ distributions for each sensor are obtained at each angle of attack. In order to filter out some deviant points in the C_f vs. ϕ distributions of the sail-on-side case, a robust locally weighted regression technique called *loess method* (Cleveland [29]) is used. This smoothing technique uses pre-determined windows of ϕ values in the regression process and gives higher weights to the points near to the location where the smoothed C_f value is sought. Outliers in the data set are detected during the fitting process and not used in the regression. These features enable to smooth the data without changing the original pattern. A mathematical description of the *loess method* and important parameters to be considered in the smoothing process is given in Appendix A. For further details about the method, see Cleveland [30].

4. The separation locations at each sensor location are determined from the graphs of circumferential skin-friction distributions. The local minima in C_f is used to locate the separation.

5.1.2 Results and Discussion for the Barebody Case

For the range of test conditions mentioned in chapter 4, steady results over the barebody show typical characteristics of the crossflow separation. Figure 5.1 shows the oil flow visualization of the near-wall fluid over the constant diameter region of the model at $\alpha = 20\,^\circ$ in the barebody case (Wetzel [20]) and qualitatively describes the crossflow separation topology. Skin-friction lines converge along the separation lines and from this figure two separation lines can be identified on the leeward side of the model. The one closer to the windward side is defined as the primary separation and the other as the secondary separation line.

Figures 5.5 to 5.18 give the skin-friction C_f distribution vs. circumferential location on the model surface ϕ for different x/L stations each at a steady angle of attack α. They show the change of the circumferential C_f distribution as a function of x/L at each α value. Figures 5.19 to 5.32 give the C_f distribution vs. ϕ for all steady angles of attack at each sensor location. From these figures, the change of circumferential C_f distribution as a function of α at each x/L location can be observed. Barebody results are represented by the filled symbols. In these figures, primary separation locations can be detected as the most windward minima of the C_f distribution and the secondary separation location can be obtained by finding the second minimum. Figures 5.33 and 5.34 show the primary separation locations as a function of α for each sensor location. The primary separation locations can be first detected at the last five stations $x/L = 0.638$, 0.706, 0.774, 0.819, and 0.863 for $\alpha = 3.1\,^\circ$. However, the primary separation locations can be seen more clearly at angles of attack starting from $\alpha = 5.1\,^\circ$. From figures 5.33 and 5.34, it can be seen that as x/L increases, the primary separation location moves towards the windward side at a specific angle of attack. The same behavior can also be seen as the angle of attack increases: the primary separation location moves towards the windward side at a specific x/L location. At $x/L = 0.266$, $\phi = 150\,^\circ$ can be located as the first primary separation at $\alpha = 11.3\,^\circ$. For this station, the primary separation location moves to $\phi = 134\,^\circ$ at $\alpha = 27.6\,^\circ$. At $x/L = 0.819$, the primary separation location starts from $\phi = 147\,^\circ$ at $\alpha = 3.1\,^\circ$ and moves to $\phi = 111\,^\circ$ at $\alpha = 27.6\,^\circ$. Figures 5.35 and 5.36 show the secondary separation locations vs. α for different x/L stations. The secondary separation can be first detected at $\alpha = 11.3\,^\circ$. For this angle of attack, the secondary separation location is $\phi = 141\,^\circ$ at $x/L = 0.774$ and $\phi = 143\,^\circ$ at $x/L = 0.819$. In general, at a certain angle of attack, the secondary separation location moves leeward as

x/L increases. Although no data between the measurement stations are available, the separation location at each x/L location can be used to interpolate the values in-between and this may give an estimate of the primary and secondary separation lines on the model surface.

From the circumferential skin-friction distributions, a nearly flat profile can be seen (figure 5.31) at the vicinity of the minimum point for the last station, $x/L = 0.863$ located on the stern region. The flat profile extends from $\phi = 100\,^\circ$ to $\phi = 124\,^\circ$ at $\alpha = 15.3\,^\circ$. This profile indicates separated low speed fluid in this complex flow region that makes the identification of the true minimum difficult. The result is consistent with the oil-flow visualization pictures of this region. Figure 5.2 shows the low speed fluid pattern on the stern region at $\alpha = 15\,^\circ$.

Figure 5.19 shows a bump in the C_f distribution on the leeward side of the model at the first station $x/L = 0.110$ starting from $\alpha = 15.3\,^\circ$. In this region, at $\alpha = 27.6\,^\circ$, the increase in C_f starts approximately from $\phi = 124\,^\circ$ and reaches the peak value at around $\phi = 136\,^\circ$ and returns back to regular trend at $\phi = 144\,^\circ$. A similar pattern can be observed also for the stations $x/L = 0.131$ and 0.170. These three stations are located on the nose region of the model. Therefore, this C_f pattern may imply a weak separation and reattachment of the flow on the nose region of the model at relatively high angles of attack.

Figures 5.37 and 5.38 show the comparison of the barebody primary separation locations obtained with the hot-film sensors and the oil-flow visualizations. The angle of attack is approximately $15\,^\circ$ for figure 5.37 and $20\,^\circ$ for the other. In both figures, the oil-flow predicts the separations locations more windward compared to the hot-film results with a difference of approximately 20°. As described in Wetzel et al. [32], the errors associated with the separation locations of the oil-flow visualization can be attributed to the gravity effects or direct interactions between the flowfield and the oil mixture, which tends to pool near separations. As in this study, these errors can be very significant, therefore oil-flows should be used for qualitative interpretations of the flow only.

Steady barebody C_f data obtained with the solid walls are compared with the slotted wall results in figures 5.39 through 5.44 at three x/L stations: 0.345, 0.570, and 0.819. The results are presented for two angles of attack: for the solid wall case, $\alpha = 10\,^\circ$ and $\alpha = 20\,^\circ$ and for the slotted wall case $\alpha = 9.3\,^\circ$ and $\alpha = 19.4\,^\circ$. For all the stations,

the difference between the solid wall and the slotted wall data can be observed on the windward side and on the last part of leeward side starting approximately from $\phi = 150°$. On these regions, the skin-friction values of the slotted wall case are higher than the ones obtained in the solid wall case. This difference is more significant at $\alpha = 20\,°$ due to the increased blockage effect of the model. At both angles of attack, the difference in C_f decreases as x/L increases. In other words, the blockage effect in C_f values is more obvious on the upstream constant diameter part of the model as compared to the stern region. The primary and the secondary separation locations are the same in both wall configurations, thus the separation locations are less sensitive to the blockage effect.

5.1.3 Results and Discussion for the Sail-on-side Case

In figures 5.5 to 5.32, open symbols stand for the C_f vs. ϕ distributions of the sail-on-side case. It is more appropriate to evaluate the results of the sail-on-side case in two separate regions: the region with no sail (between $\phi = 0\,°$ and $180\,°$) and the region with the sail (between $\phi = 180\,°$ and $360\,°$). In the first region, the origin and the variation of the primary and the secondary separation lines as a function of x/L and α show the same characteristics as defined for the barebody case. This implies that the main flow feature on the non-sail region is the cross flow separation. Figures 5.45 and 5.46 give the primary separation locations vs. α for each x/L stations on the non-sail side. The same distribution for the secondary separation locations are presented in figures 5.47 and 5.48. Although the general trend is the same, the locations of the primary and the secondary separations are slightly different from the barebody separation locations. They are more leeward compared to the barebody locations. This difference can be observed in figures 5.49 and 5.50. Figure 5.49 shows the variation of the primary separation location with α for three different x/L stations. As can be seen from this figure, the primary separation locations of the barebody case and the non-sail region of the sail-on-side case are approximately the same within uncertainties up to $\alpha = 15.3°$. Beyond this angle, the separation locations of the sail-on-side case start to deviate from the barebody results having an offset in the leeward direction. This difference is obvious for $\alpha = 21.4\,°, 23.4\,°$ and $25.5°$. Figure 5.50 shows the variation of the secondary separation location with α for the same x/L locations. In this figure, for all angles of attack, the secondary separation locations on the non-sail region of the sail-on-side case are shifted in the leeward direction

compared to the secondary separation locations of the barebody case.

The skin-friction distribution trend of the sail region on the nose part of model is approximately the same as the one obtained for the barebody case. At stations $x/L = 0.110$, 0.131 and 0.170, the same flow separation and reattachment pattern can be seen starting from $\alpha = 15.3\,^{\circ}$. As can be seen from the figures 5.19, 5.20, and 5.21, C_f vs. ϕ distributions for all angles of attack are symmetric with respect to $\phi = 180\,^{\circ}$. The low speed separated flow region on the stern of the model can be seen again from figure 5.4 which shows the oil flow pattern of this region for the sail-on-side case at $\alpha = 10\,^{\circ}$.

Downstream of the sail, the flow structure on the sail side of the model is much different than the one observed for the non-sail side. The flow field in this region is strongly affected by the presence of the sail. Compared to the separation topology of the barebody and the non-sail region of the sail-on-side case, the separation location trend as a function of x/L and α shows significant differences. Two minima in C_f vs. ϕ distributions on the leeward side of the sail region can be observed for certain angles of attack and x/L locations.

Figures 5.51 and 5.52 show the first (measured from $\phi = 180\,^{\circ}$) of these separation locations as a function of α for different streamwise measurement stations starting from $x/L = 0.434$. At the stations upstream of $x/L = 0.434$, this separation pattern is not observed. For the other stations, first measured separation location on the leeward side does not follow a certain pattern as the angle of attack or x/L are increased. It changes between $\phi = 207\,^{\circ}$ and $\phi = 216\,^{\circ}$ in an irregular fashion. This separation pattern can be observed at different angles of attack for different sensor locations. The first angle of attack at which this separation can be detected is $\alpha = 5.1\,^{\circ}$ for all sensor locations, while the highest angle of attack changes for different x/L. Among all the sensor locations, the highest angle of attack is $17.4\,^{\circ}$ and observed at $x/L = 0.434$. Beyond this angle of attack, the minimum associated with the first separation location on the leeward side of the sail region vanishes at all x/L locations.

A second minima in C_f distribution can be located on the leeward side of the sail region. Figures 5.53 and 5.54 show these separation locations at angles of attack between $\alpha = 3.1^{\circ}$ and $\alpha = 27.6\,^{\circ}$ for the sensor stations starting from $x/L = 0.434$. For the stations $x/L = 0.434$, 0.501, 0.570, and 0.638, the separation locations move leeward as the angle of attack is increased up to $15.3\,^{\circ}$. After this particular angle of attack, the separation

location for each sensor remains approximately the same. For the stations downstream of $x/L = 0.638$, the separation locations move leeward until $\alpha = 9.3\,^\circ$ is reached. At the remaining angles of attack, the separation location remains approximately at the same ϕ location for each sensor station. The results on the sail side indicate that the flow field does differ from the crossflow separation structure observed for the barebody and non-sail region of the sail-on-side case. Therefore the categorization of the separation locations as the primary or the secondary is not clear and may not reflect the real flow structure of this region.

The flow in the vicinity of the sail-body junction is dominated by the horseshoe type separation. This can be clearly seen from figure 5.3 which shows the oil-flow pattern in the leeward side of the sail region at $\alpha = 15\,^\circ$. The separation line emanating from a three-dimensional stagnation point upstream of the sail extends from both leeward and windward side of the sail and travels downstream. The separation line on the leeward side of the sail can be seen along the converging skin friction lines in figure 5.3. Although the flow topology near the onset of the horseshoe separation is different from that of the crossflow separation as described in Yates and Chapman [1], both show similar characteristics of separated flows downstream: there is a strong convergence of the limiting streamlines on the surface and there are concentrated regions of vorticity in the flow. This may raise the ambiguity about the identification of the separation pattern downstream of the sail. However, the first and second separation locations on the leeward side of the sail region described in the previous paragraph may represent the separation lines emanating from the leeward and windward side of the sail respectively. At high angles of attack, only one separation line (described by the second minimum in the previous paragraph) can be detected. This may imply that leeward and windward separation lines emerge just at the downstream of the sail forming a single separation line.

Figures 5.55 to 5.68, show the C_f contours around the sail region at steady angles of attack. Note that the blank areas are the regions where no data were acquired. The vertical blank between $x/L \simeq 0.22$ and $x/L \simeq 0.26$ designates the ring area where the sail is mounted. These contour plots are generated by using the C_f measurements obtained from both sensor sets A and B. From figure 5.55, the symmetry in the C_f distribution with respect to the sail chord line at $\alpha = 0.9\,^\circ$ can be observed. This symmetry disappears as the angle of attack is increased. In figure 5.62, at $\alpha = 15.3\,^\circ$, a low velocity region can be noticed at around $x/L = 0.27$ and $\phi = 245\,^\circ$ which also

matches with the oil flow visualization results at that location given by figure 5.3. C_f on the hull takes relatively large values at regions closer to the sail. At higher angles of attack starting from $\alpha = 21.4\,^\circ$, the increase in the C_f magnitude on the leeward side of the sail leading edge where the flow is most accelerated can also be seen.

5.2 Steady Pressure Measurements

5.2.1 Data Reduction

Pressure data reduction was straight forward, however some corrections to the data had to be made. As described in chapter 2, the pressure taps were on the sensor plugs located just behind each hot-film sensor. Although the sensor plugs were levelled with the surface of the model as much as possible, there were slight surface irregularities in the vicinity of the pressure holes which effected the pressure distribution. These irregularities were minimized before the final measurements. However, there were still some oscillations in the data. In order to get rid of these oscillations, the following approach has been developed: the local irregularities on the pressure ports effect the shape of the local streamlines (make more convex or concave) changing the local static pressure measured. By using the normal-to-wall momentum equation, this change in the pressure coefficient ΔC_p can be approximated as:

$$\frac{dC_p}{dr} \sim \frac{U^2}{r} \tag{5.5}$$

where U is the velocity in the local streamwise direction and r is the normal-to-wall coordinate. Assuming that the local streamline curvature due to the surface irregularity will be approximately the same at all angles of attack and roll position of the model;

$$\Delta C_p = A\left(\frac{U^2}{U_\infty^2}\right) \tag{5.6}$$

Here A is the unknown coefficient which is different for each port position. With a simple approach, C_p can be written as:

$$C_p = 1 - \frac{U^2}{U_\infty^2} \tag{5.7}$$

By using the above result in equation 5.6;

$$\Delta C_p = A(1 - C_p) \tag{5.8}$$

If we define ΔC_p as the correction to be made to each port location, then we can write

$$C_{pc} = C_{pm} + \Delta C_p \tag{5.9}$$

where C_{pm} is the measured C_p value and C_{pc} is the corrected C_p value. By using the expression for ΔC_p given by equation 5.8, we can obtain the final form of the correction equation as:

$$C_{pc} = A + (1 - A)C_{pm} \tag{5.10}$$

In order to find the A value for each port position, the C_p results of the barebody at $0\,^\circ$ angle of attack obtained from a RANS code were used (figure 5.69). These CFD results were supplied by Dr. D. L. Whitfield, Mississippi State University. At each port position, the C_{pc} was taken as the C_p value of the CFD and the C_p values of the barebody pressure measurements at $0\,^\circ$ angle of attack with slotted walls were taken as the C_{pm}. The A values obtained as the result of this procedure were used for the correction of the rest of the data that were taken at $10\,^\circ$ and $20\,^\circ$ angles of attack.

5.2.2 Results and Discussion

Figures 5.70 and 5.71 show barebody pressure coefficient C_p vs. circumferential location ϕ distributions for different x/L locations at $\alpha = 10\,^\circ$. Each figure has 10 x/L locations which gives a total number of 20 streamwise measurement stations at a specific angle of attack. The first station is located at $x/L = 0.112$ and the last one at $x/L = 0.845$. Note that the pressure measurement stations are slightly downstream of the corresponding skin-friction measurement locations. However, the difference is approximately 0.2% of the overall model length and can be considered as negligible. All measurement stations given in C_p figures lie on the long sensor row of the model. Figures 5.72 and 5.73 show the same kind of distribution for $\alpha = 20\,^\circ$.

In figures 5.70 to 5.73, C_p values are presented for two wind tunnel wall configurations. Solid symbols represent the solid wall results and the open symbols stand for the slotted wall case. As can be seen from these figures, C_p values of the solid wall case are more negative compared to the ones obtained in the slotted wall case through all ϕ locations. This is an expected result, since in the solid wall case the fluid over the measurement stations is accelerated more compared to the real flow conditions due to the blockage effect of the model at angle of attack. This extra pressure gradient term makes the

C_p values more negative. On the other hand, in the slotted wall configuration with an open-air ratio of 38%, the blockage effect can be reduced significantly and more reliable pressure and skin-friction values can be obtained. The difference between the slotted and solid wall results is more significant for $\alpha = 20\,^\circ$.

At both angles of attack, a favorable pressure gradient can be observed on the windward side of the model for each sensor. The leeward side of model can be thought as a pressure recovery region. However due to the crossflow separation on the leeward side of the model, the general C_p trend does not follow a monotonic increase. Especially at $\alpha = 20\,^\circ$, a local minimum in C_p distribution can be detected on the leeward side of the model at each station between $x/L = 0.288$ and $x/L = 0.777$. As also observed by Wetzel [2] in the prolate spheroid case, these minima are the result of the flow separation and may coincide beneath the coherent vortices that form in such an open separation. These vortices with relatively high circulation induce again higher local velocities which in turn lead to a local pressure decrease immediately beneath the vortical core. The C_p distributions of the last two stations $x/L = 0.821$ and $x/L = 0.865$ follow a different trend on the leeward side of the model at both angles of attack compared to the other stations. As in the skin-friction case, a relatively flat C_p profile can be observed on the circumferential locations corresponding to the low speed separated flow region of the stern.

Figures 5.74 and 5.75 show C_p vs. ϕ distributions for different x/L locations at $\alpha = 10\,^\circ$ for the sail-on-side case. The data are compared with the barebody case on the non-sail region of the model. Solid symbols represent the C_p values of the sail-on-side case while the open symbols are used for the barebody case. Both sail-on-side and barebody results are obtained with the slotted wall configuration. Figures 5.76 and 5.77 show the same kind of distribution for $\alpha = 20\,^\circ$. Note that the scales of the C_p axes are different for $\alpha = 10\,^\circ$ and $\alpha = 20\,^\circ$ cases. On the non-sail region of the model (between $\phi = 0\,^\circ$ and $\phi = 180\,^\circ$), the C_p distributions follow the same trend as the one obtained for the barebody case at both angles of attack and the values are approximately the same within the uncertainties. On the sail side, the mean pressure distributions are affected by the presence of the sail except the first four stations on the nose part of the model. These four stations show a symmetric pressure distribution with respect to $\phi = 180\,^\circ$. For the other stations, this symmetry can not be observed. The effect of the sail is significant at the stations located between $x/L = 0.210$ and $x/L = 0.308$. The station at $x/L = 0.210$ is just upstream of the sail and the pressure increase due the stagnation process can be

clearly seen between $\phi = 260\,^\circ$ and $\phi = 280\,^\circ$. The C_p value takes its maximum value approximately at $\phi = 280\,^\circ$ for both angles of attack. The pressure distributions in the vicinity of the leading edge of the sail are of particular interest, since they are responsible for the formation of the horseshoe vortices in this region as described by Simpson [31]. During the measurements two stations were under the sail: station $x/L = 0.268$ between $\phi = 262\,^\circ$ and $\phi = 270\,^\circ$, and station $x/L = 0.288$ between $\phi = 267\,^\circ$ and $\phi = 269\,^\circ$. For these two stations, the C_p values at the ϕ locations under the sail are left blank in the figures.

Figures 5.78 through 5.81 show the C_p vs. x/L distributions obtained with slotted walls for different ϕ locations at $10\,^\circ$ and $20\,^\circ$ angles of attack . Figures 5.78 and 5.79 give the results for the barebody case. For $\alpha = 10\,^\circ$, a smooth change of C_p with x/L at different ϕ values can be observed. At $\alpha = 20\,^\circ$, C_p values are more scattered and the magnitude difference between each ϕ position is bigger. Sail-on-side results are given in figures 5.80 and 5.81. At both angles of attack, the effect of the sail on the pressure distribution can be seen on the leeward side of the model, especially at $\phi = 210\,^\circ$ and $\phi = 270\,^\circ$.

In order to determine the circumferential behavior of the mean pressure in the separated flow regions, C_p distributions are compared with the C_f variations at the same x/L locations. C_f distributions of $x/L = 0.501$ and $x/L = 0.774$ at $\alpha = 11.3\,^\circ$ and $\alpha = 21.4\,^\circ$ are compared with the C_p variations of $x/L = 0.503$ and $x/L = 0.777$ at $\alpha = 10\,^\circ$ and $\alpha = 20\,^\circ$. Figures 5.82 to 5.85 show the comparison of the barebody case at the conditions given above, while the figures 5.86 to 5.89 show the comparison of the sail-on-side case. A common characteristic of the pressure distributions in the vicinity of the separation locations can be observed from the barebody figures: the mean pressure values are approximately constant over the separated fluid regions. This zero pressure gradient region is obvious at $x/L = 0.777$ for $\alpha = 20\,^\circ$ given by the figure 5.85. The flat pressure profile on the leeward side of the model covers the region between $\phi = 111\,^\circ$ and $\phi = 153\,^\circ$ and includes both the primary and the secondary separation locations. The same C_p trend can be observed on the leeward side of the non-sail region in the sail-on-side case. As discussed before, at relatively low angles of attack, two separation locations can be observed on the sail region of model. In figure 5.86, these two separation locations can be seen on the leeward side of the sail region at $x/L = 0.501$ for $\alpha = 11.3\,^\circ$. Over the first separation location ($\phi = 216\,^\circ$), the pressure gradient is not zero whereas for the second separation location ($\phi = 260\,^\circ$) a constant pressure region exists. At higher

angles of attack, only the second separation location remains and the first one vanishes. In figure 5.89, at $x/L = 0.777$ for $\alpha = 20°$, again a flat pressure profile over the separation location on the leeward side of the sail region can be detected. As discussed in Wetzel et al. [32], although the pressure data are used often to indicate the existence of massive separation, it is not a good indicator of the separation location. This is due to the fact that the crossflow separation is the result of a local flow phenomena, but pressure at a given point in space is strongly influenced by the entire flow field. The results of this study also support the aforementioned principle. One can think of using the flat pressure profile in regions of separation to locate the separation locations, however it is difficult to determine the exact point where this flat pressure distribution begins.

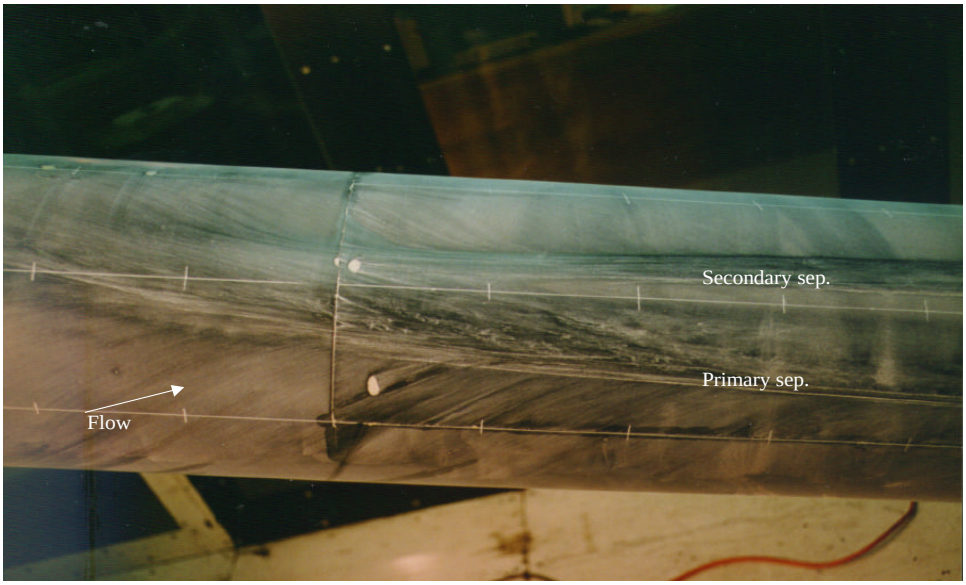

Figure 5.1: Oil flow visualization showing the cross flow separation topology on the constant diameter region of the model for the barebody case at $\alpha = 20\,^{\circ}$, $Re = 4.5 \times 10^6$. Flow is from left to right.

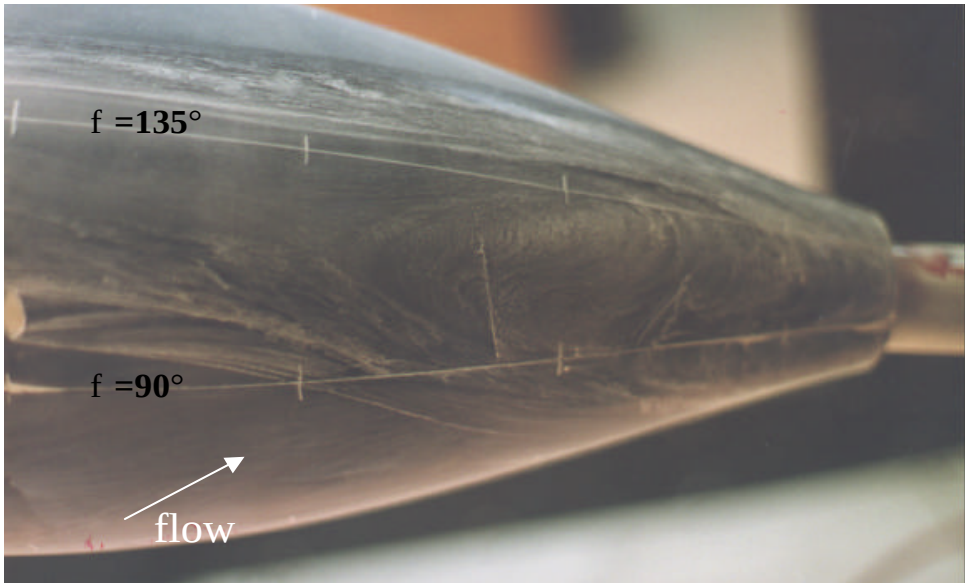

Figure 5.2: Oil flow visualization showing the low speed fluid region on the stern of the model for the barebody case at $\alpha = 15\,^{\circ}$, $Re = 4.5 \times 10^6$. Flow is from left to right.

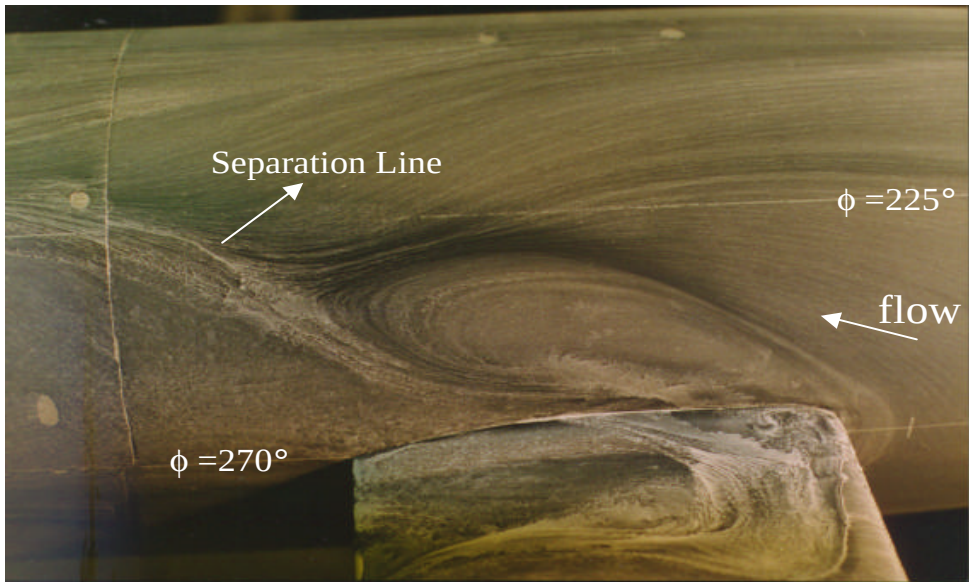

Figure 5.3: Oil flow pattern showing the separation in the vicinity of the sail at $\alpha = 15\,^{\circ}$, $Re = 4.5 \times 10^6$. Flow is from right to left.

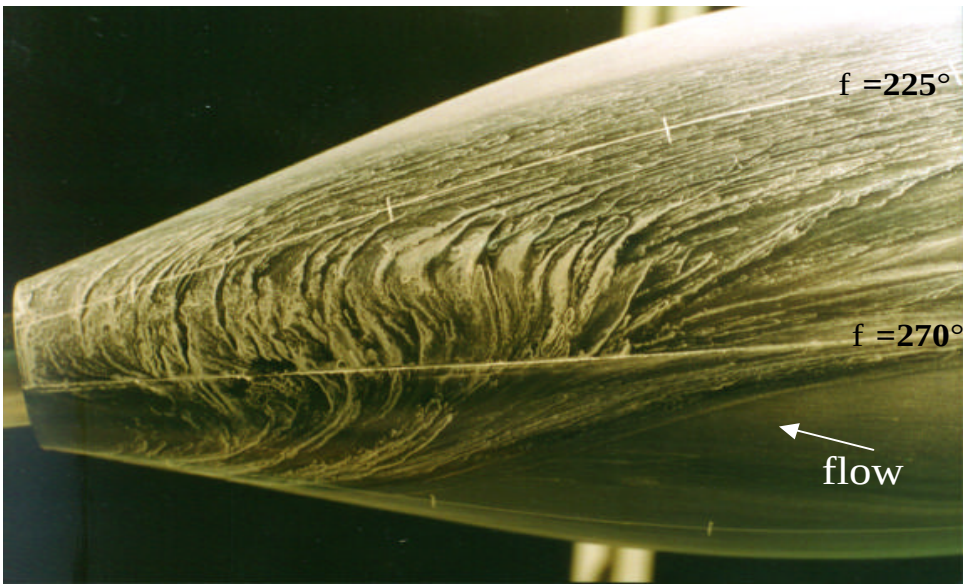

Figure 5.4: Oil flow visualization of the sail side showing the low speed fluid region on the stern of the model for the sail-on-side case at $\alpha = 10\,^{\circ}$, $Re = 4.5 \times 10^6$. Flow is from right to left.

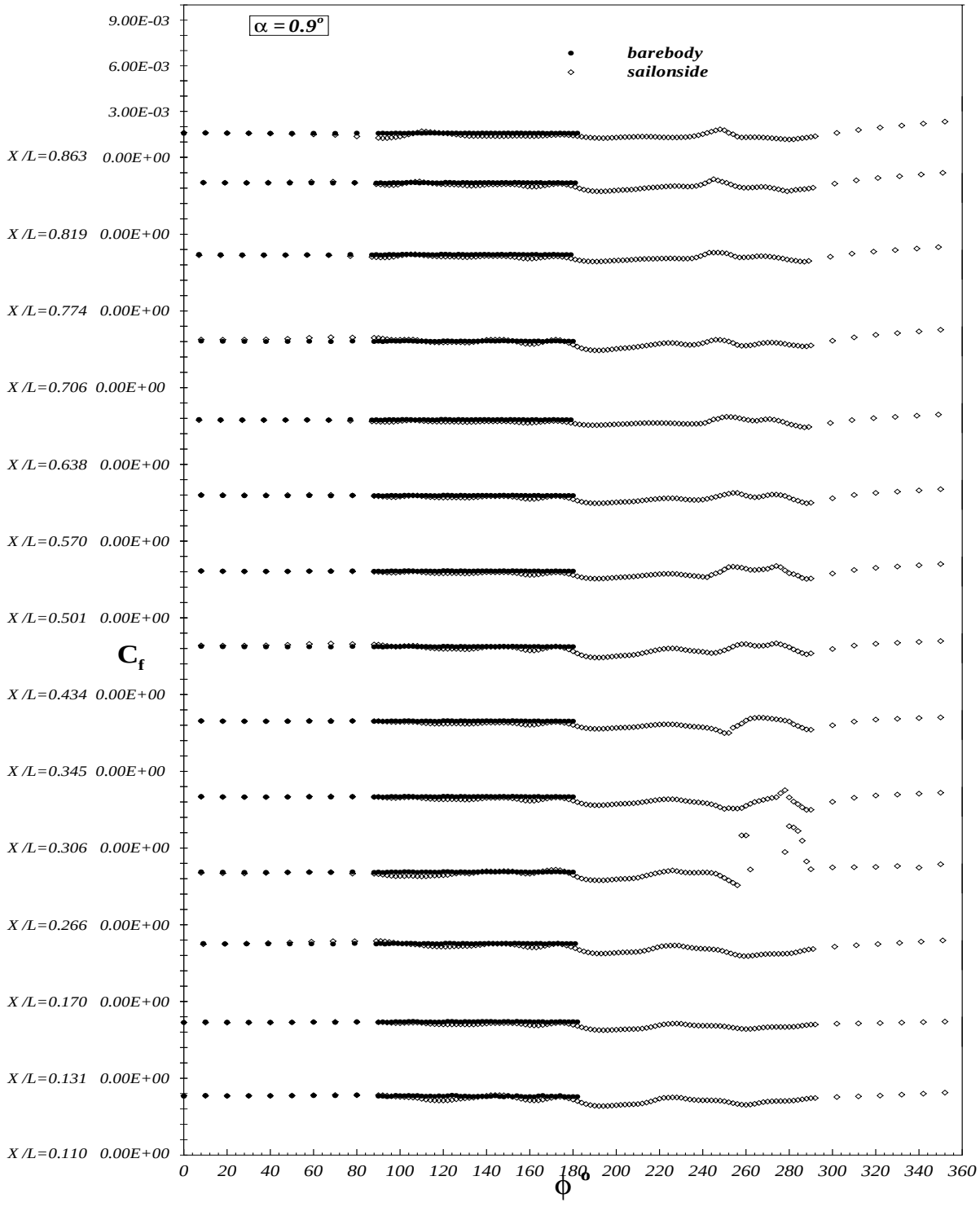

Figure 5.5: C_f vs. ϕ for all x/L locations at $\alpha = 0.9\,^\circ$ for steady barebody and sail-on-side cases. Sail side on the right of the figure starting from $\phi = 180\,^\circ$.

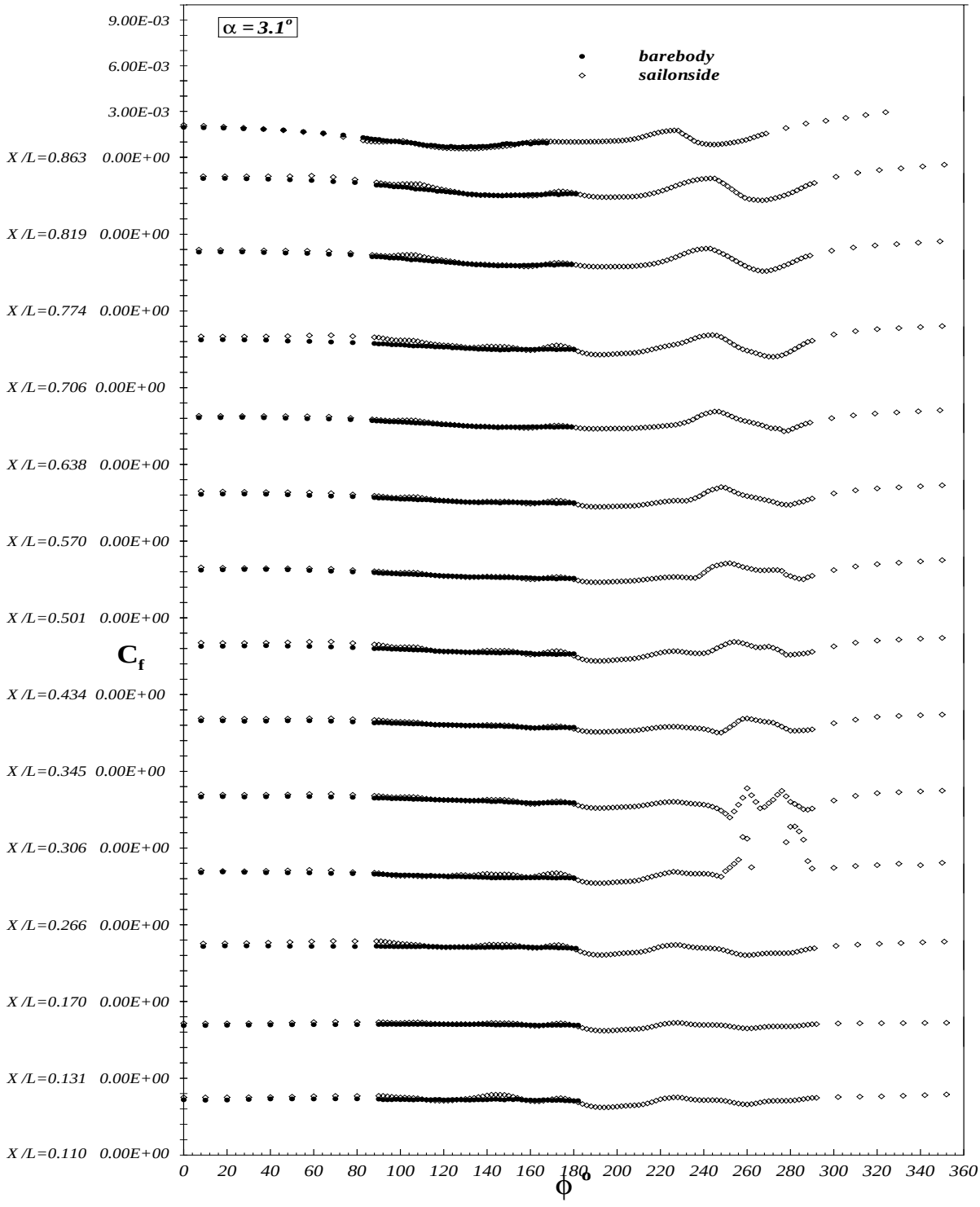

Figure 5.6: C_f vs. ϕ for all x/L locations at $\alpha = 3.1\,^\circ$ for steady barebody and sail-on-side cases. Sail side on the right of the figure starting from $\phi = 180\,^\circ$.

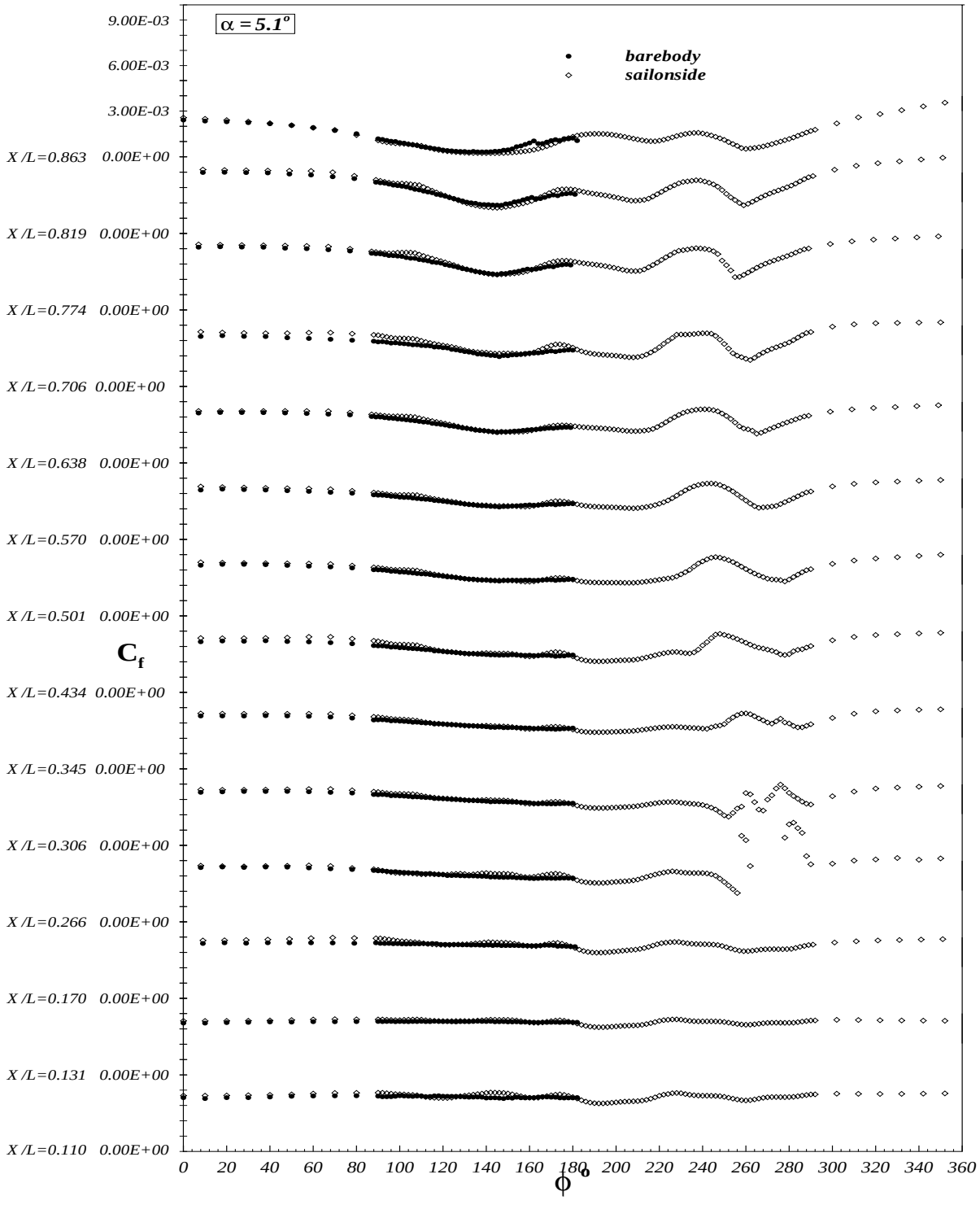

Figure 5.7: C_f vs. ϕ for all x/L locations at $\alpha = 5.1\,^\circ$ for steady barebody and sail-on-side cases. Sail side on the right of the figure starting from $\phi = 180\,^\circ$.

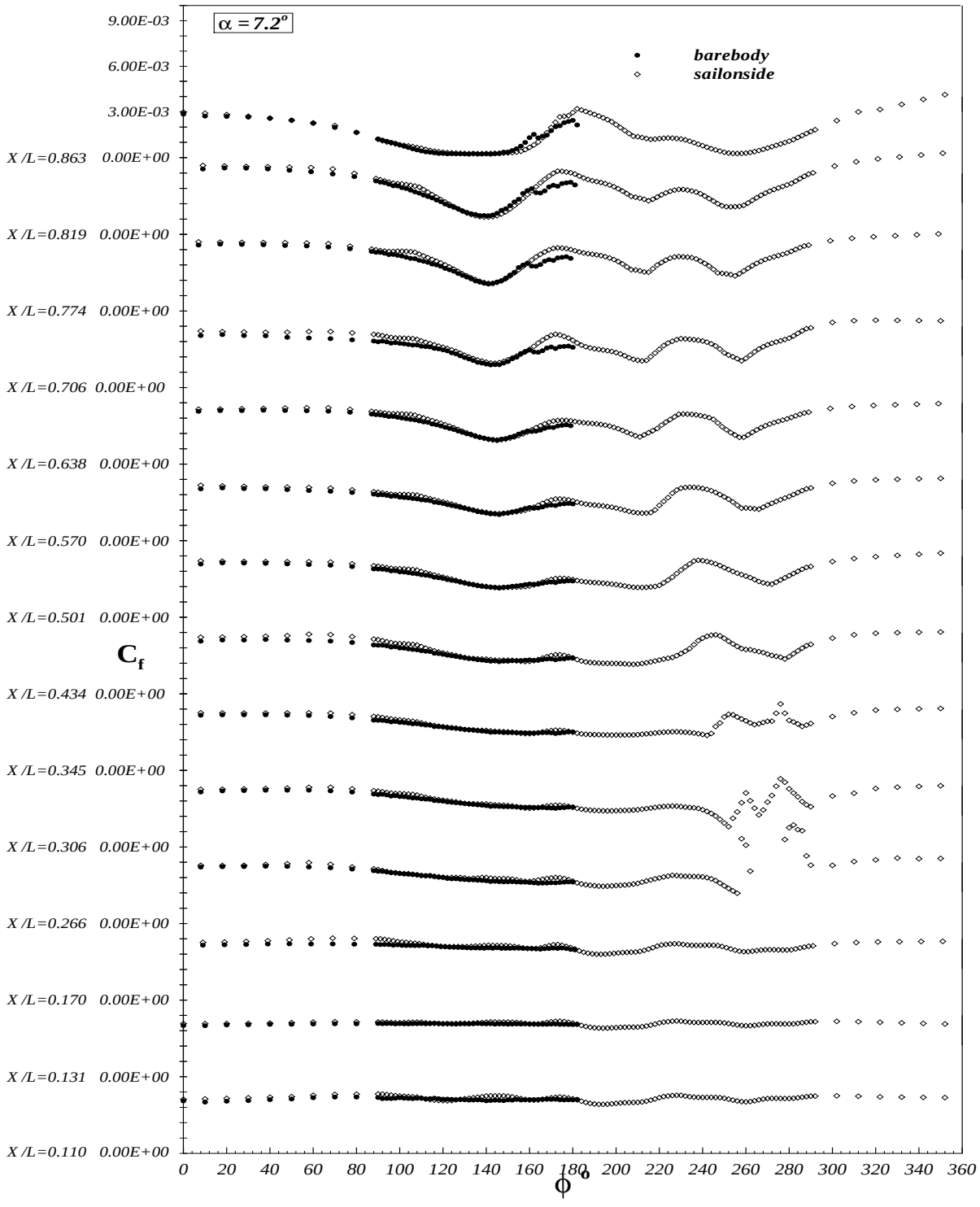

Figure 5.8: C_f vs. ϕ for all x/L locations at $\alpha = 7.2\,^\circ$ for steady barebody and sail-on-side cases. Sail side on the right of the figure starting from $\phi = 180\,^\circ$.

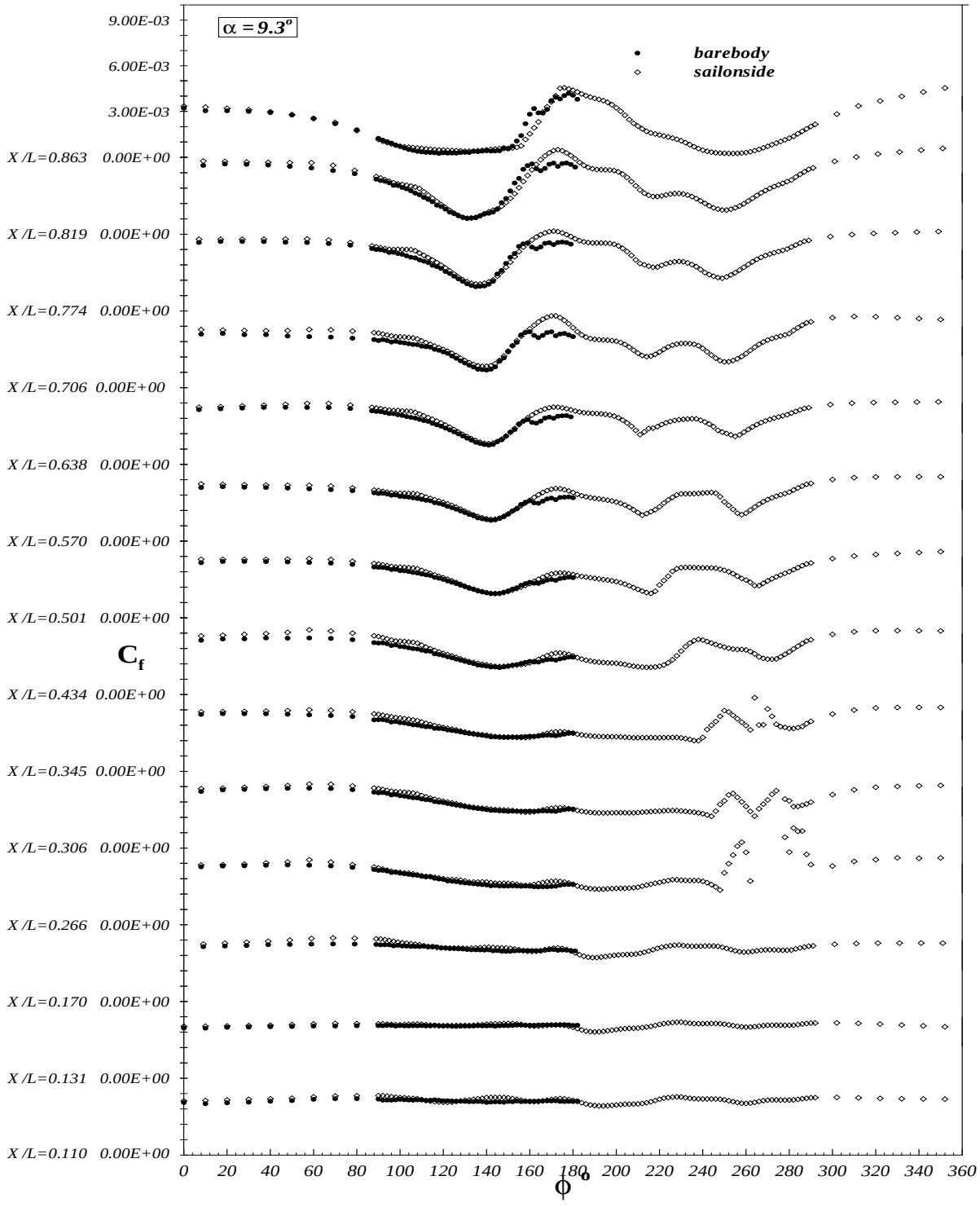

Figure 5.9: C_f vs. ϕ for all x/L locations at $\alpha = 9.3\,^\circ$ for steady barebody and sail-on-side cases. Sail side on the right of the figure starting from $\phi = 180\,^\circ$.

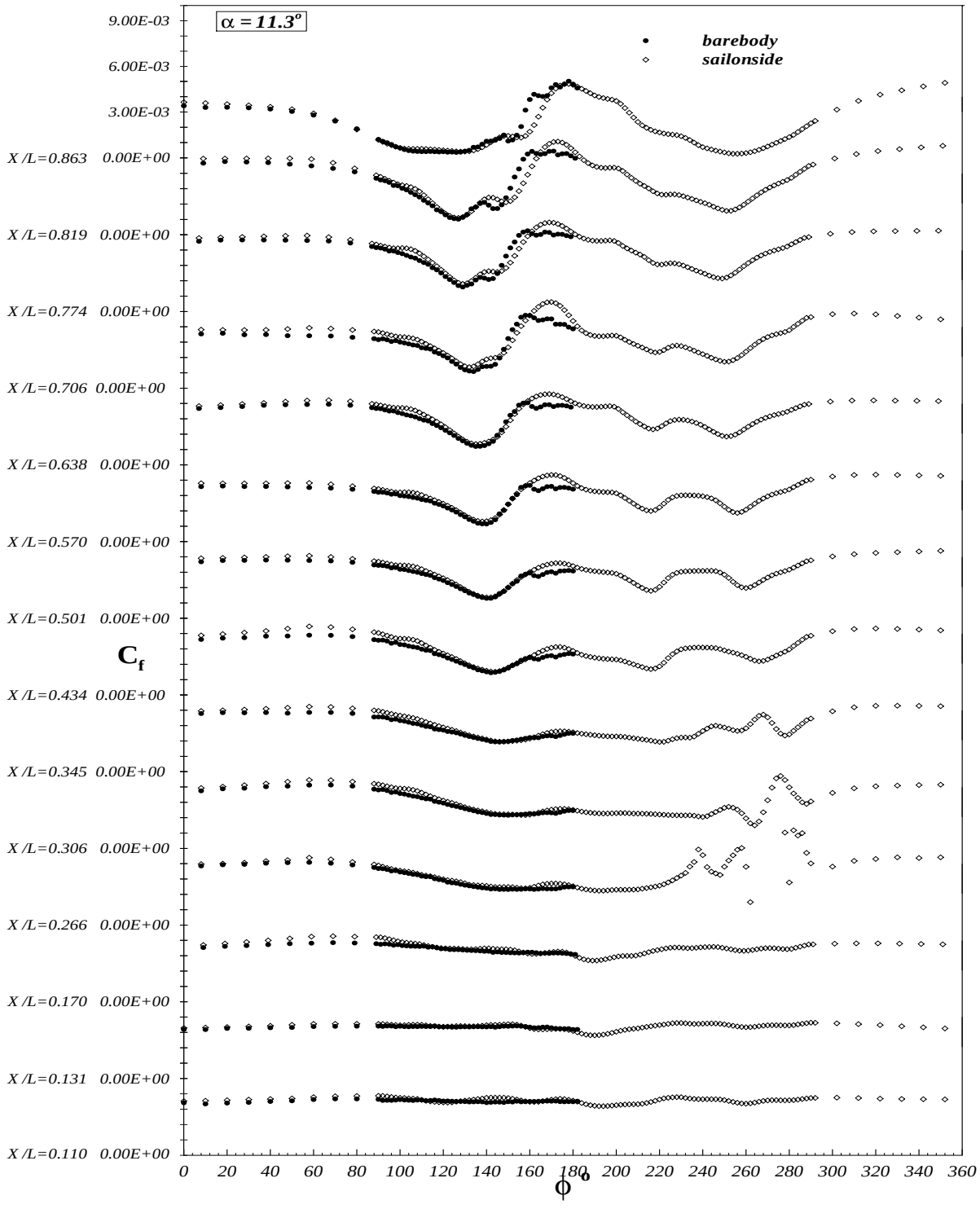

Figure 5.10: C_f vs. ϕ for all x/L locations at $\alpha = 11.3^\circ$ for steady barebody and sail-on-side cases. Sail side on the right of the figure starting from $\phi = 180^\circ$.

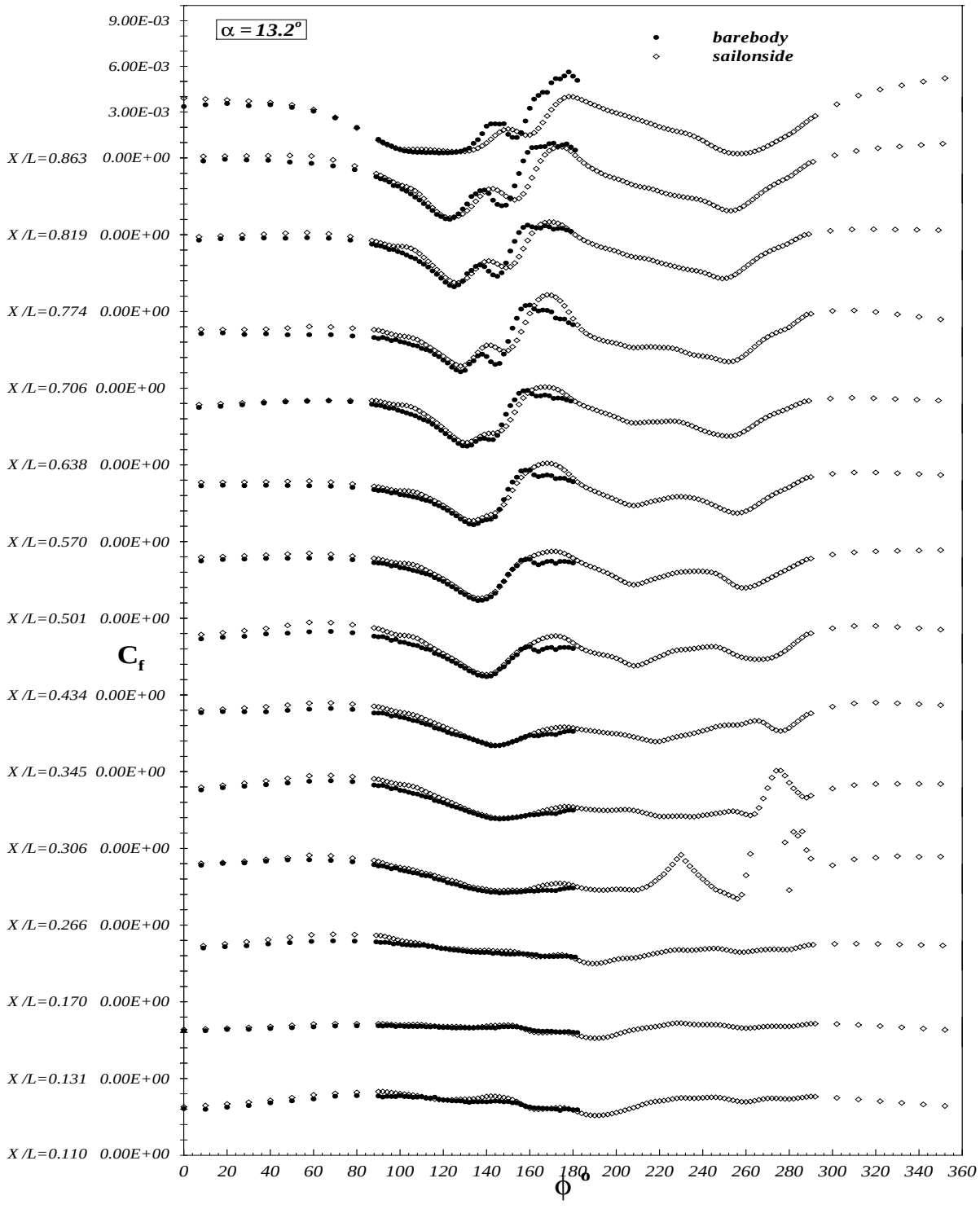

Figure 5.11: C_f vs. ϕ for all x/L locations at $\alpha = 13.2\,^\circ$ for steady barebody and sail-on-side cases. Sail side on the right of the figure starting from $\phi = 180\,^\circ$.

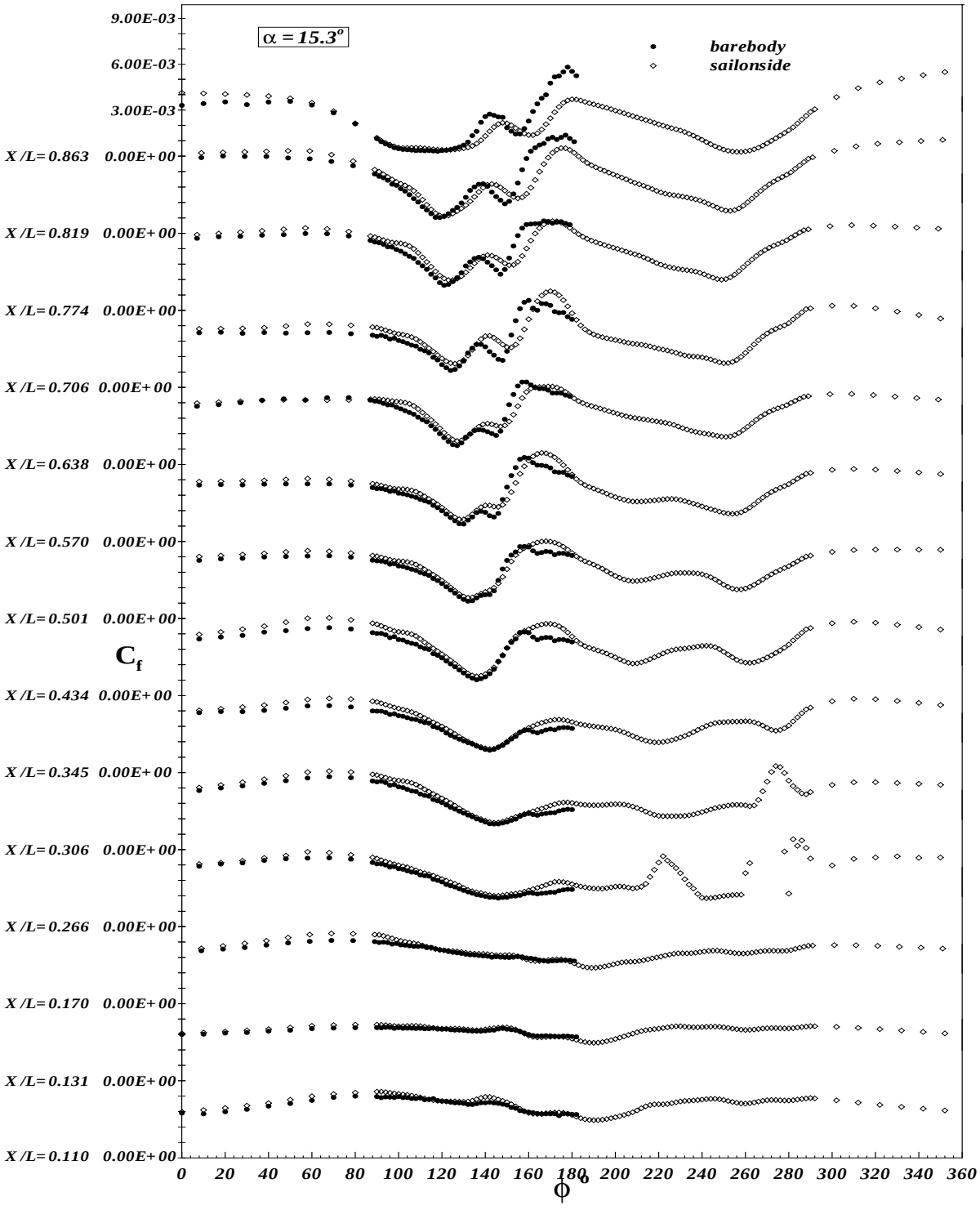

Figure 5.12: C_f vs. ϕ for all x/L locations at $\alpha = 15.3\,^\circ$ for steady barebody and sail-on-side cases. Sail side on the right of the figure starting from $\phi = 180\,^\circ$.

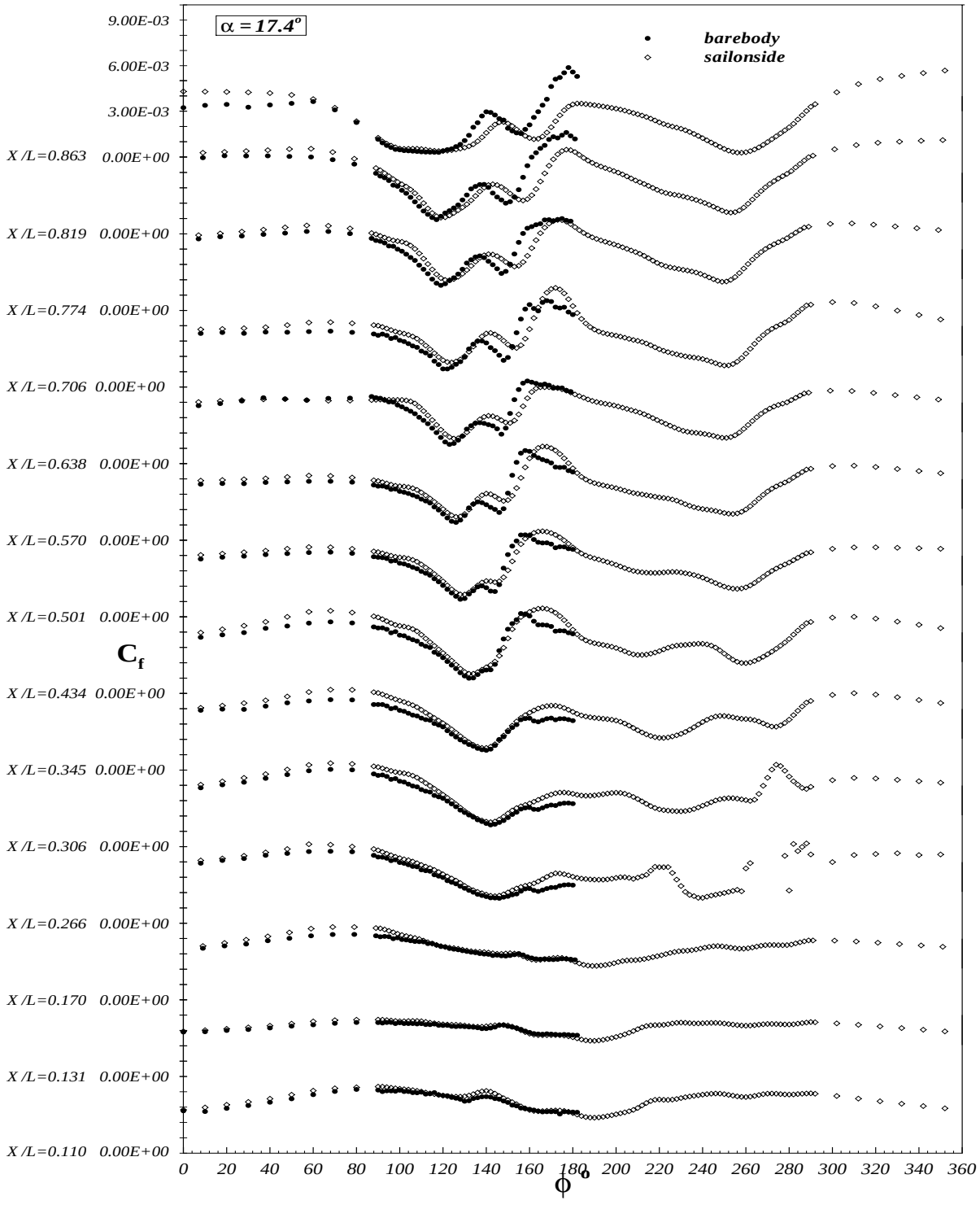

Figure 5.13: C_f vs. ϕ for all x/L locations at $\alpha = 17.4^\circ$ for steady barebody and sail-on-side cases. Sail side on the right of the figure starting from $\phi = 180^\circ$.

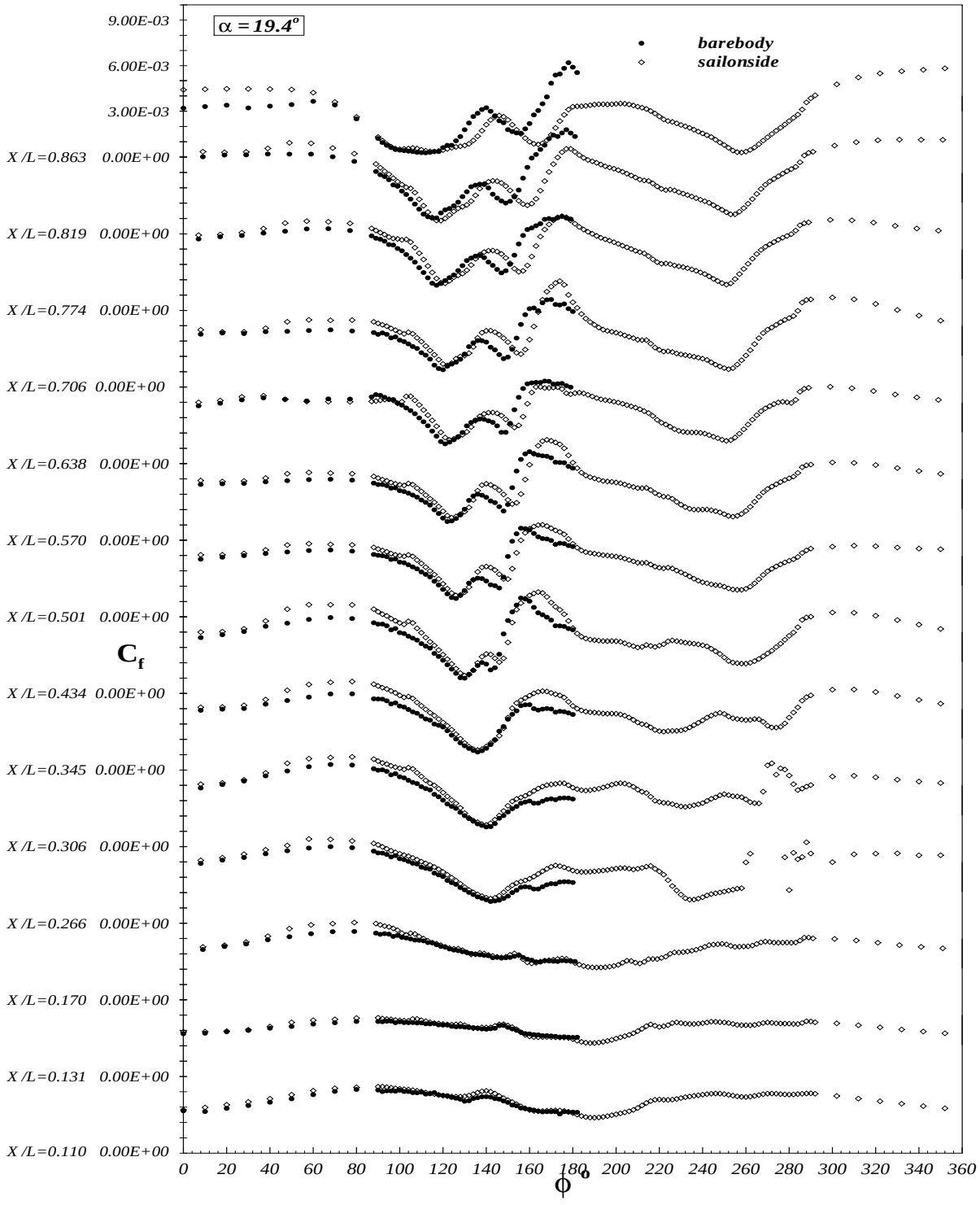

Figure 5.14: C_f vs. ϕ for all x/L locations at $\alpha = 19.4^\circ$ for steady barebody and sail-on-side cases. Sail side on the right of the figure starting from $\phi = 180^\circ$.

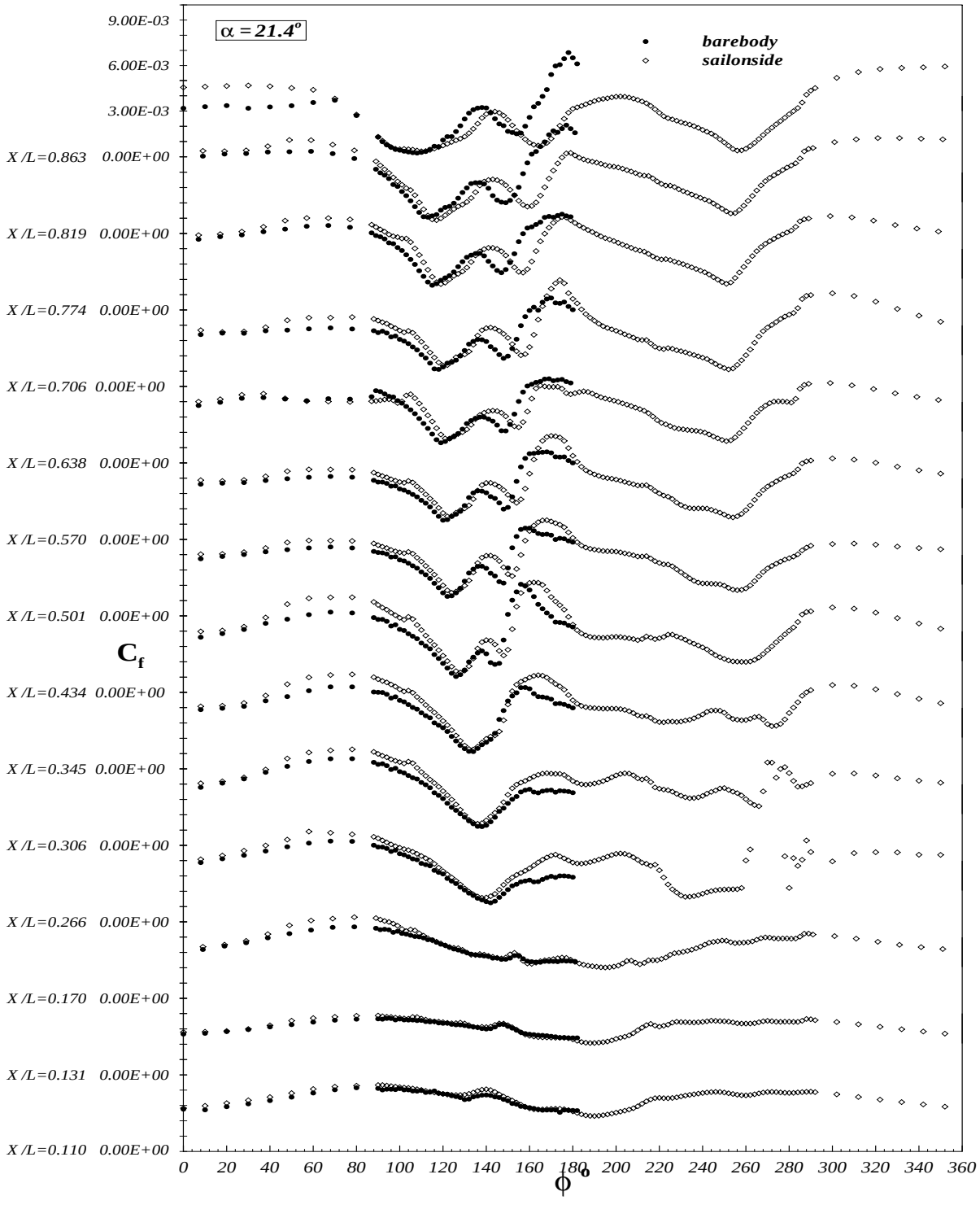

Figure 5.15: C_f vs. ϕ for all x/L locations at $\alpha = 21.4^\circ$ for steady barebody and sail-on-side cases. Sail side on the right of the figure starting from $\phi = 180^\circ$.

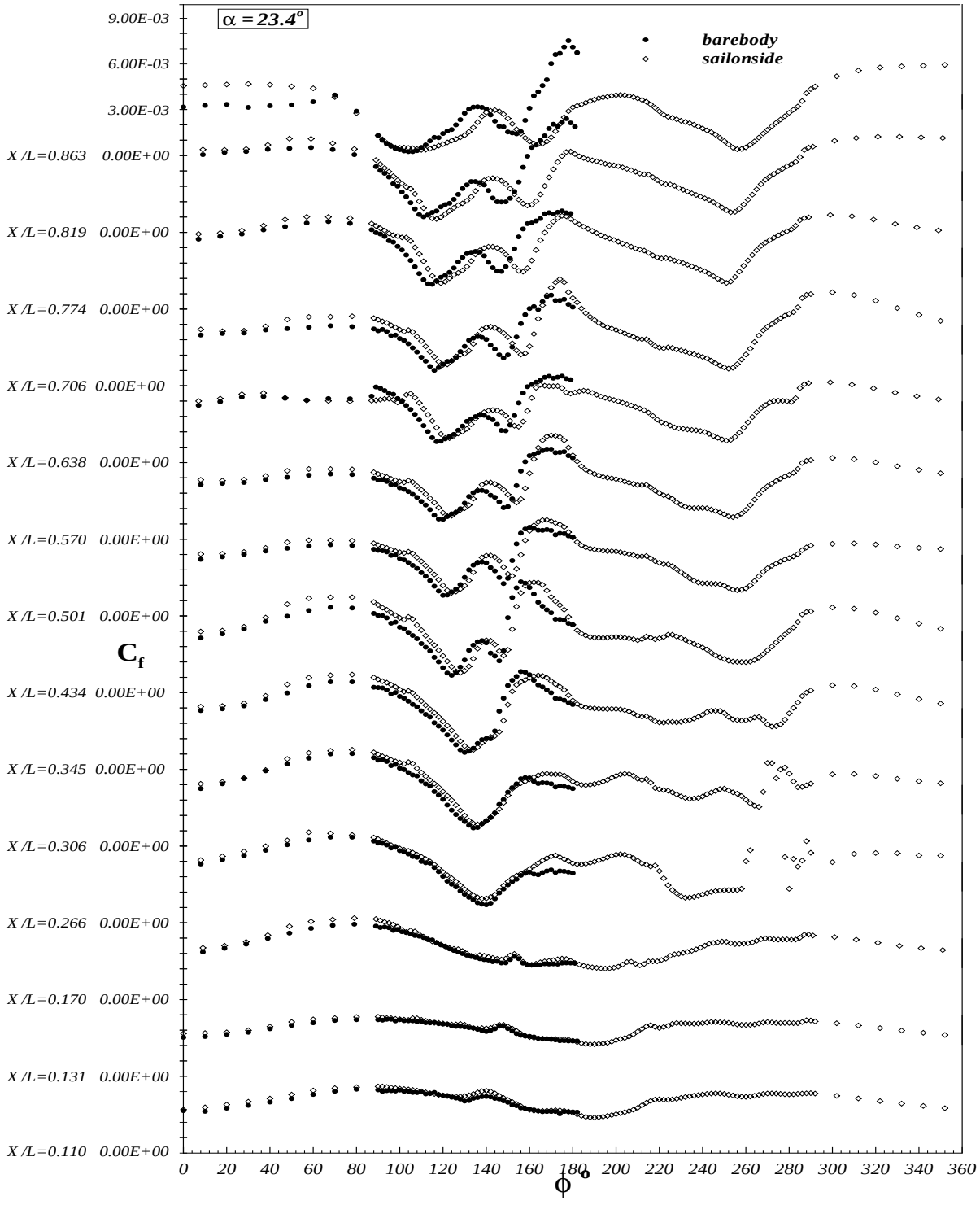

Figure 5.16: C_f vs. ϕ for all x/L locations at $\alpha = 23.4^\circ$ for steady barebody and sail-on-side cases. Sail side on the right of the figure starting from $\phi = 180^\circ$.

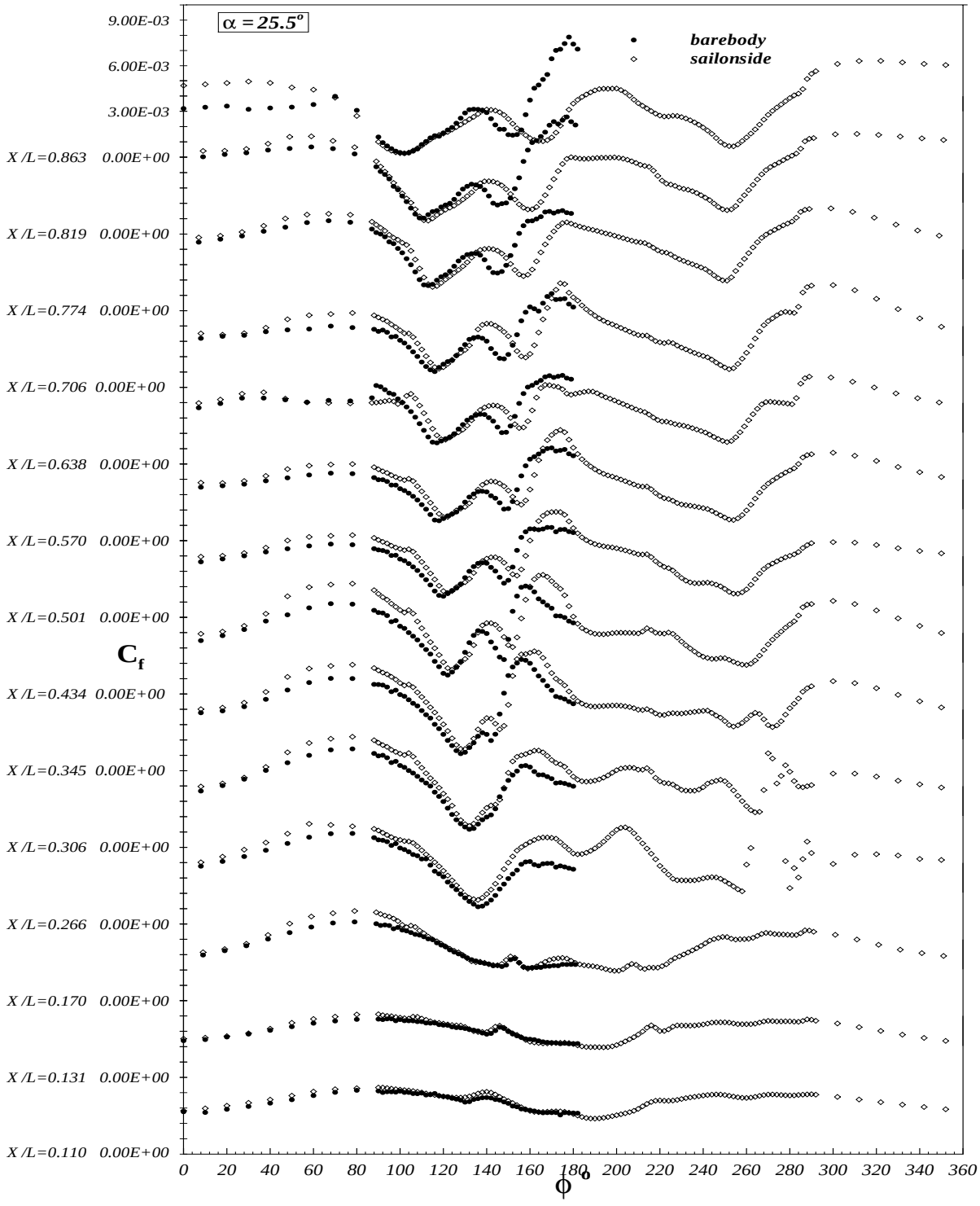

Figure 5.17: C_f vs. ϕ for all x/L locations at $\alpha = 25.5\,^\circ$ for steady barebody and sail-on-side cases. Sail side on the right of the figure starting from $\phi = 180\,^\circ$.

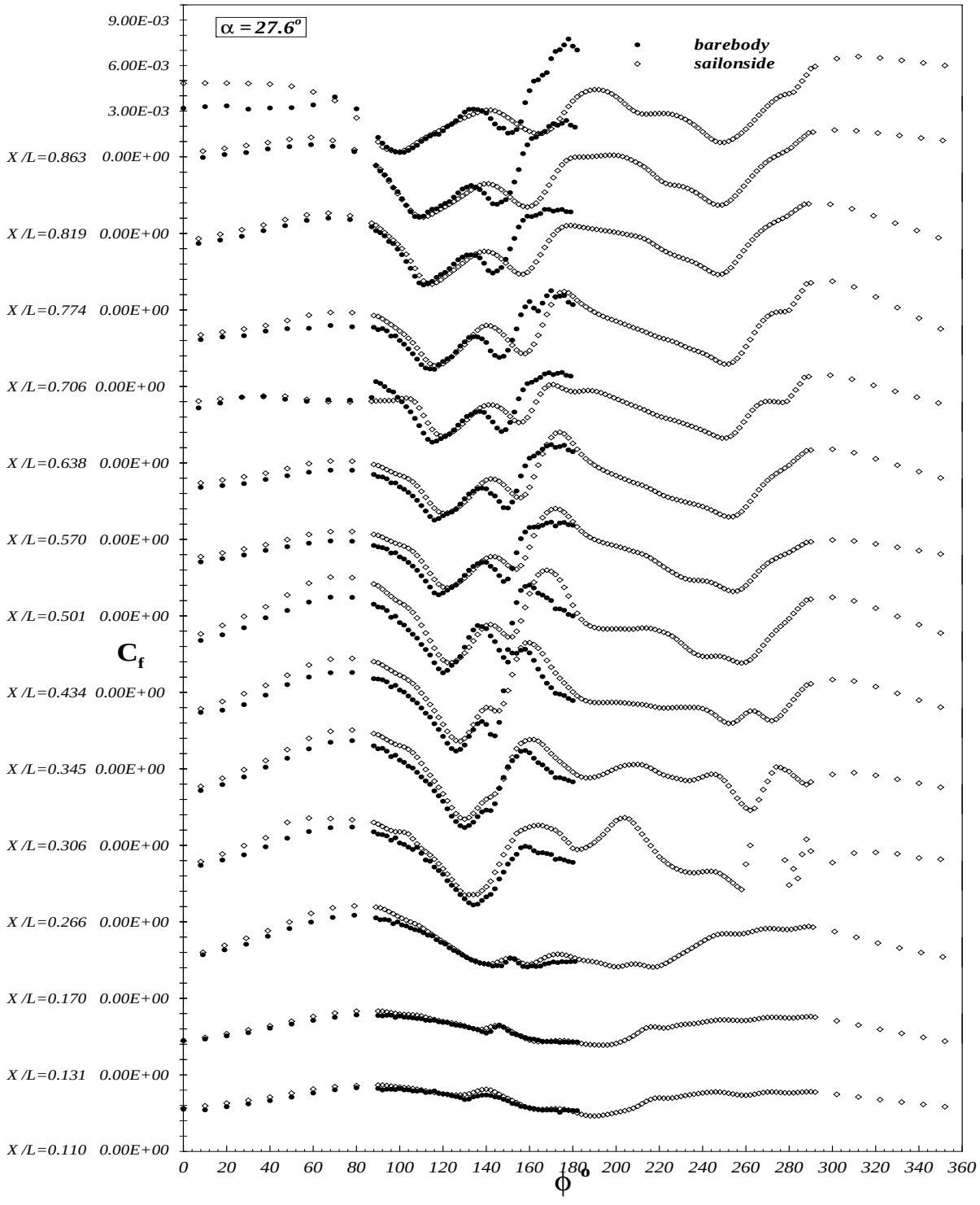

Figure 5.18: C_f vs. ϕ for all x/L locations at $\alpha = 27.6\,^\circ$ for steady barebody and sail-on-side cases. Sail side on the right of the figure starting from $\phi = 180\,^\circ$.

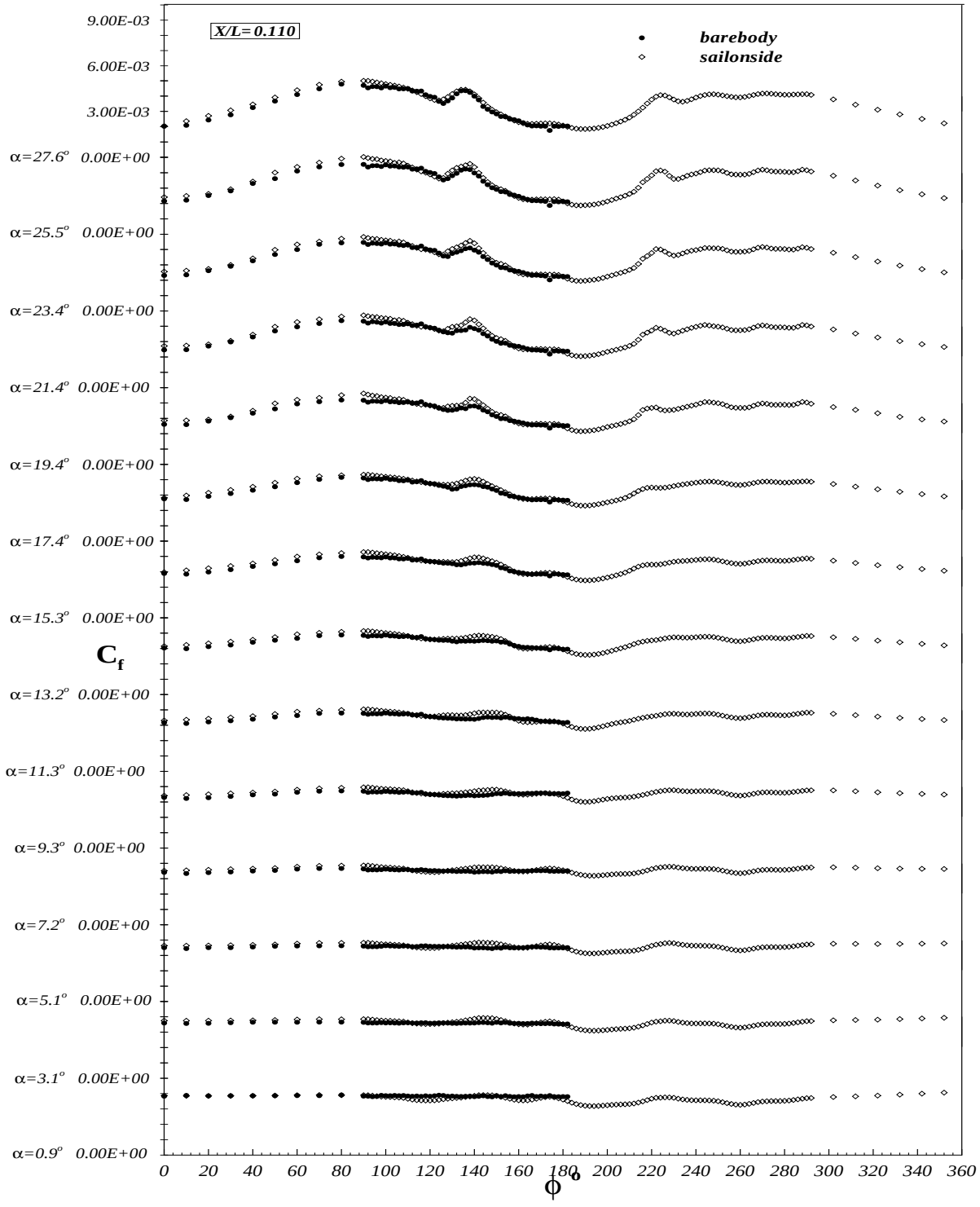

Figure 5.19: C_f vs. ϕ for all α at $x/L = 0.110$ for steady barebody and sail-on-side cases. Sail side on the right of the figure starting from $\phi = 180\,^{\circ}$.

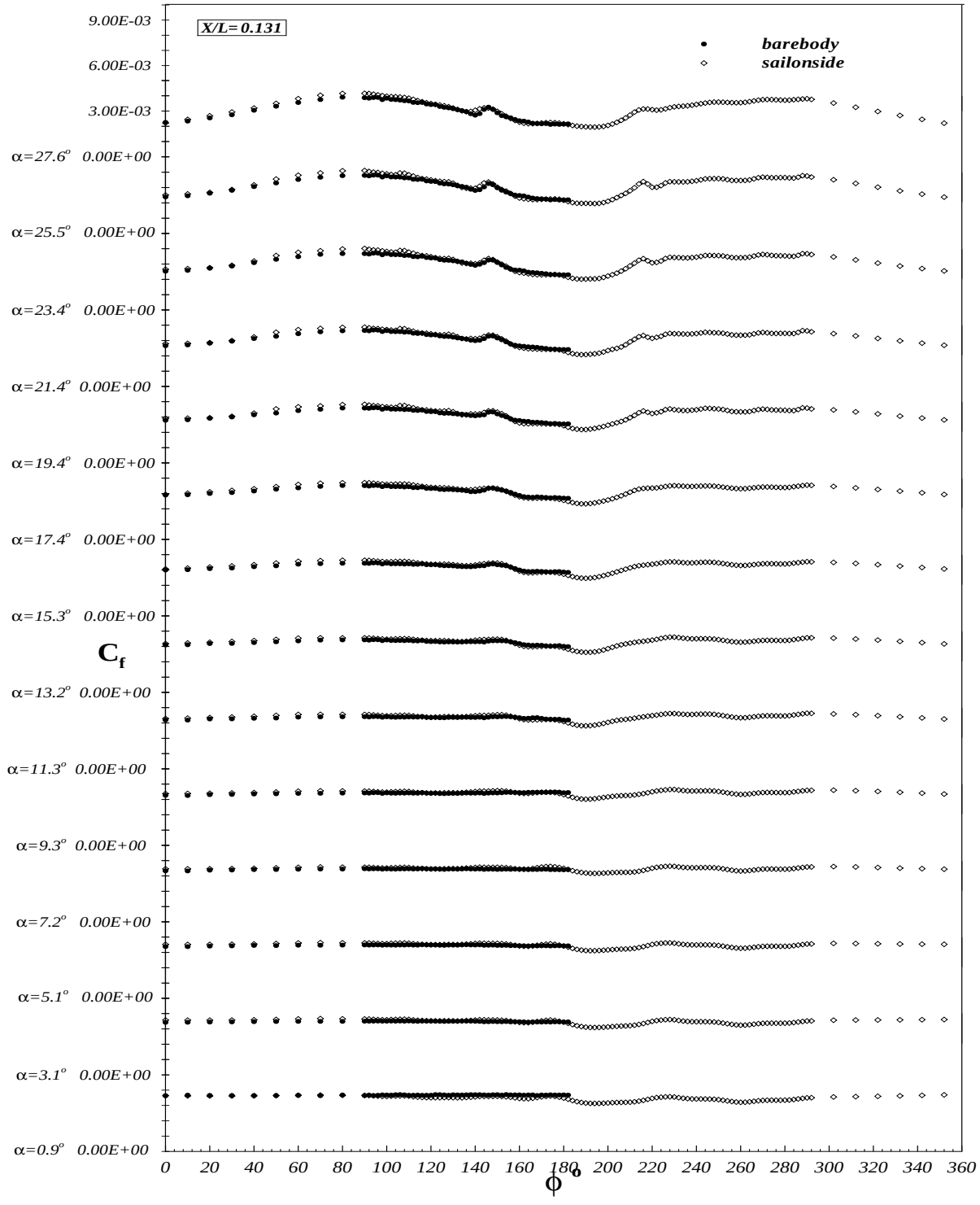

Figure 5.20: C_f vs. ϕ for all α at $x/L = 0.131$ for steady barebody and sail-on-side cases. Sail side on the right of the figure starting from $\phi = 180\,^{\circ}$.

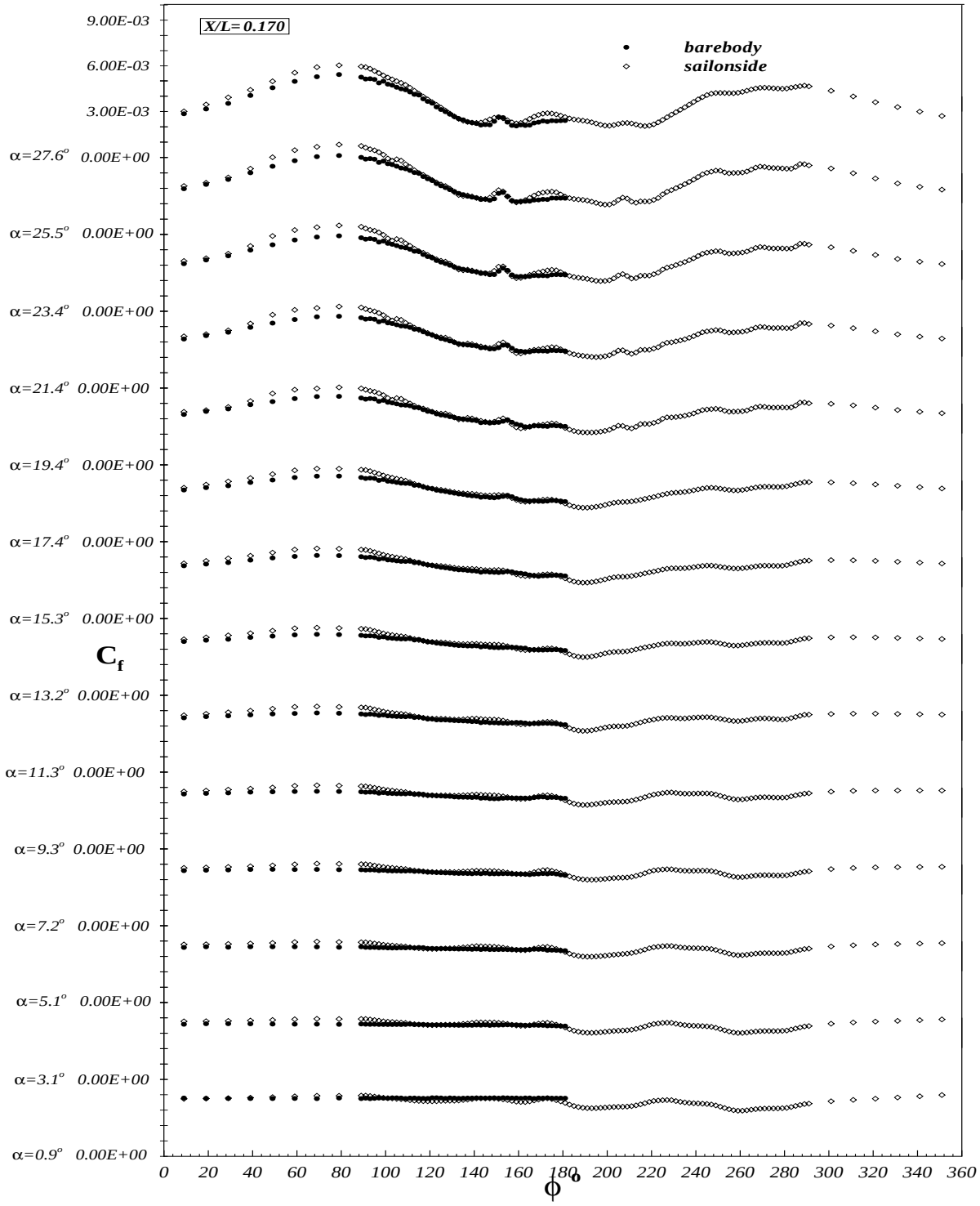

Figure 5.21: C_f vs. ϕ for all α at $x/L = 0.170$ for steady barebody and sail-on-side cases. Sail side on the right of the figure starting from $\phi = 180\,^\circ$.

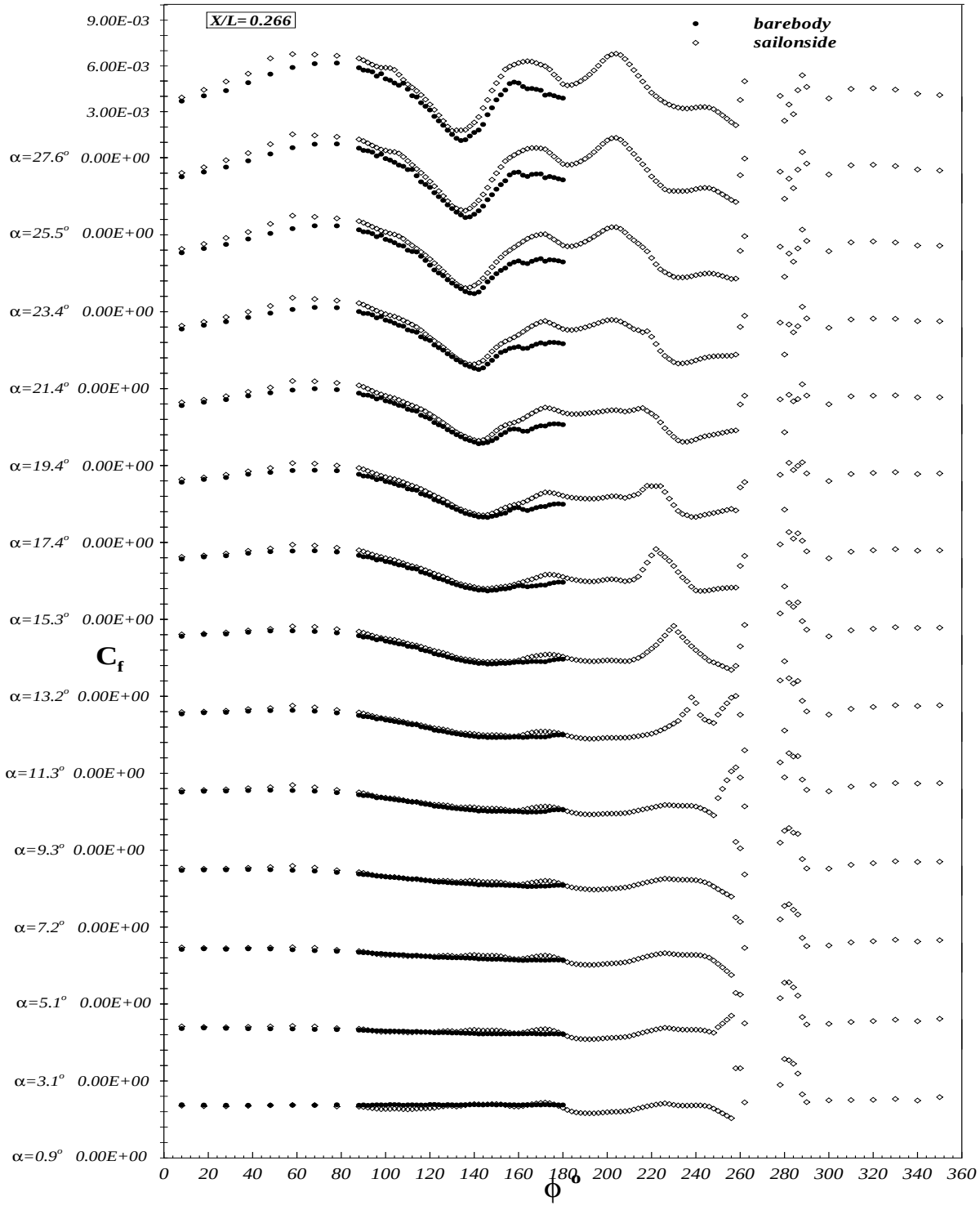

Figure 5.22: C_f vs. ϕ for all α at $x/L = 0.266$ for steady barebody and sail-on-side cases. Sail side on the right of the figure starting from $\phi = 180\,^{\circ}$.

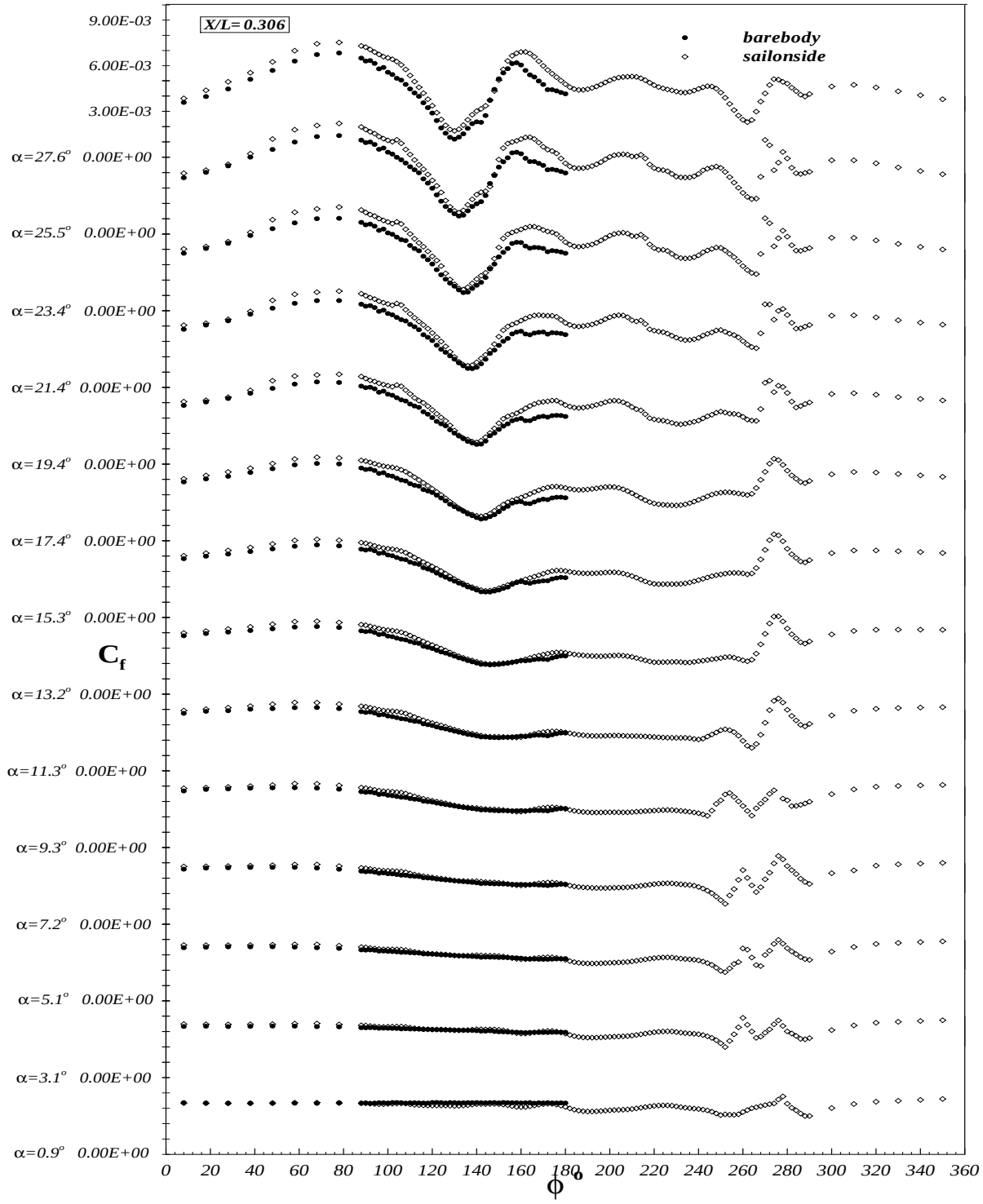

Figure 5.23: C_f vs. ϕ for all α at $x/L = 0.306$ for steady barebody and sail-on-side cases. Sail side on the right of the figure starting from $\phi = 180\,^\circ$.

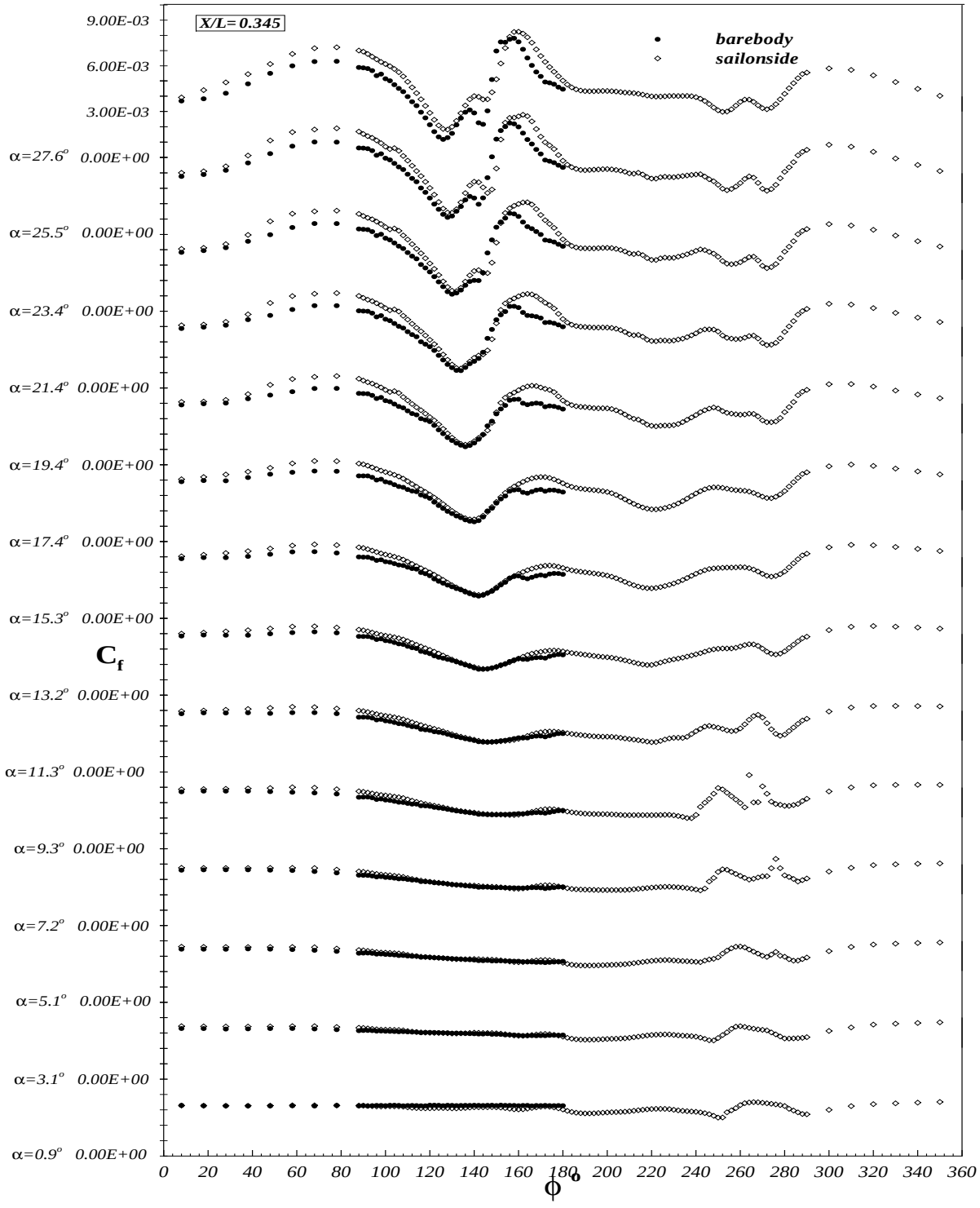

Figure 5.24: C_f vs. ϕ for all α at $x/L = 0.345$ for steady barebody and sail-on-side cases. Sail side on the right of the figure starting from $\phi = 180\,^\circ$.

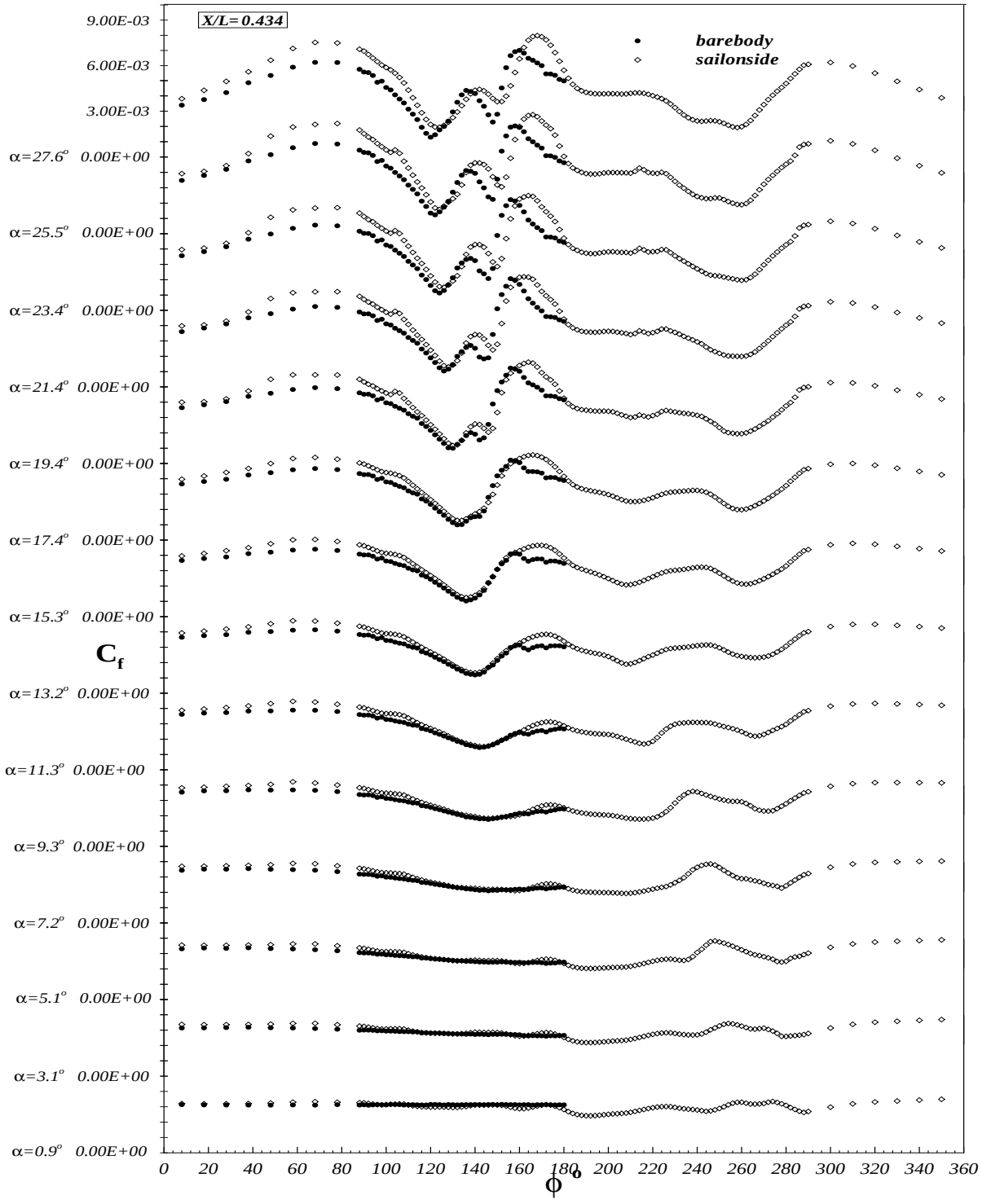

Figure 5.25: C_f vs. ϕ for all α at $x/L = 0.434$ for steady barebody and sail-on-side cases. Sail side on the right of the figure starting from $\phi = 180\,^\circ$.

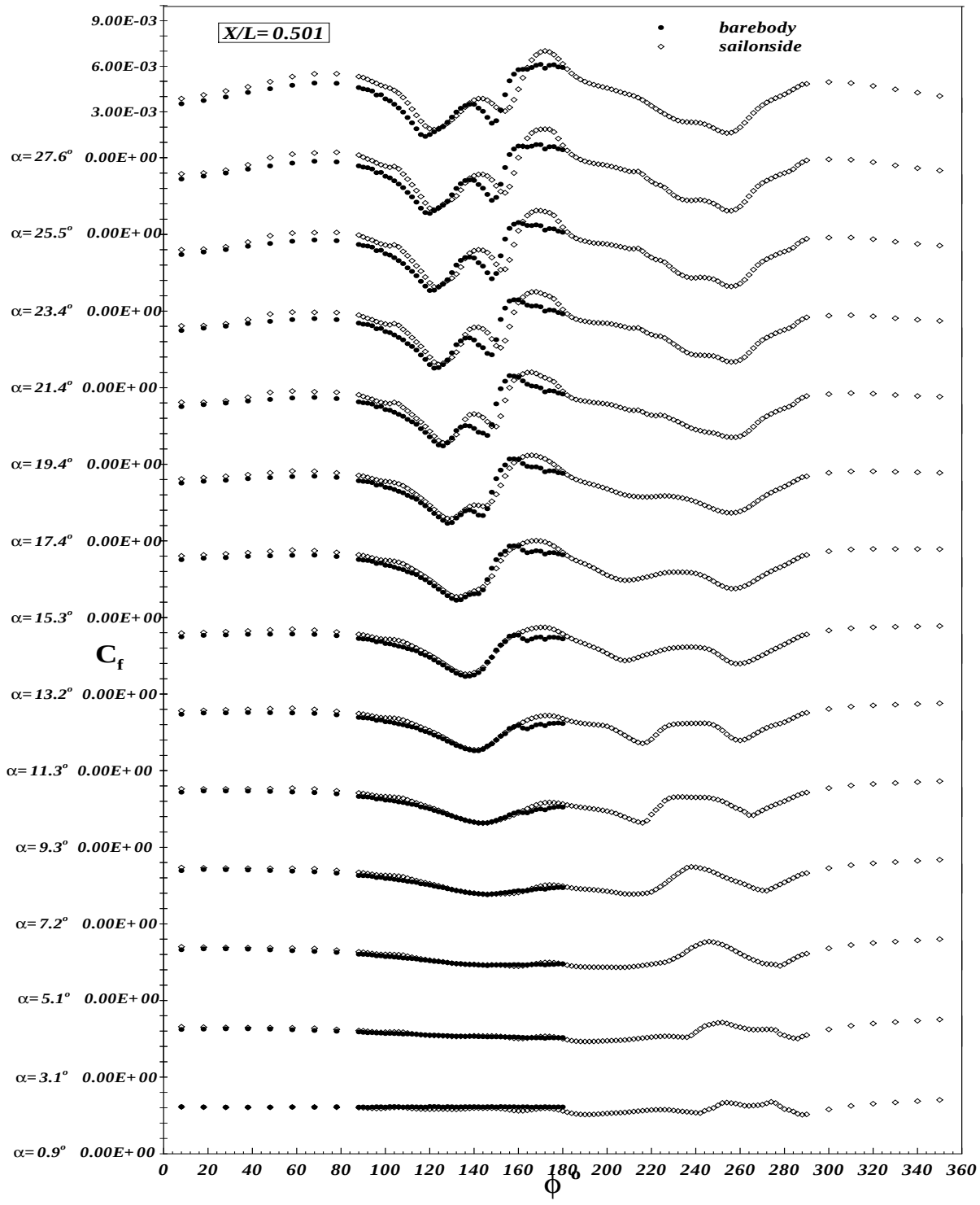

Figure 5.26: C_f vs. ϕ for all α at $x/L = 0.501$ for steady barebody and sail-on-side cases. Sail side on the right of the figure starting from $\phi = 180\,^\circ$.

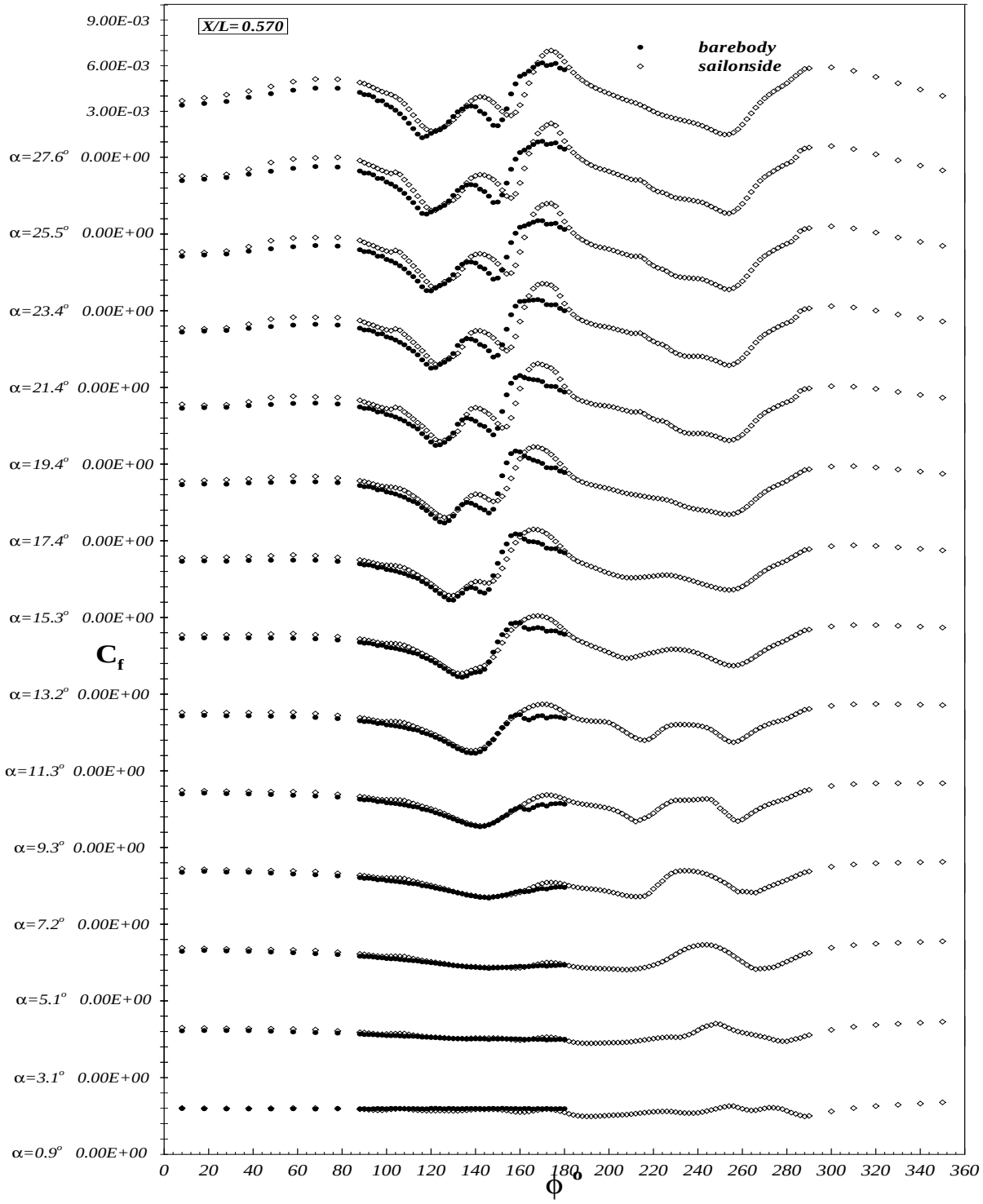

Figure 5.27: C_f vs. ϕ for all α at $x/L = 0.570$ for steady barebody and sail-on-side cases. Sail side on the right of the figure starting from $\phi = 180\,^\circ$.

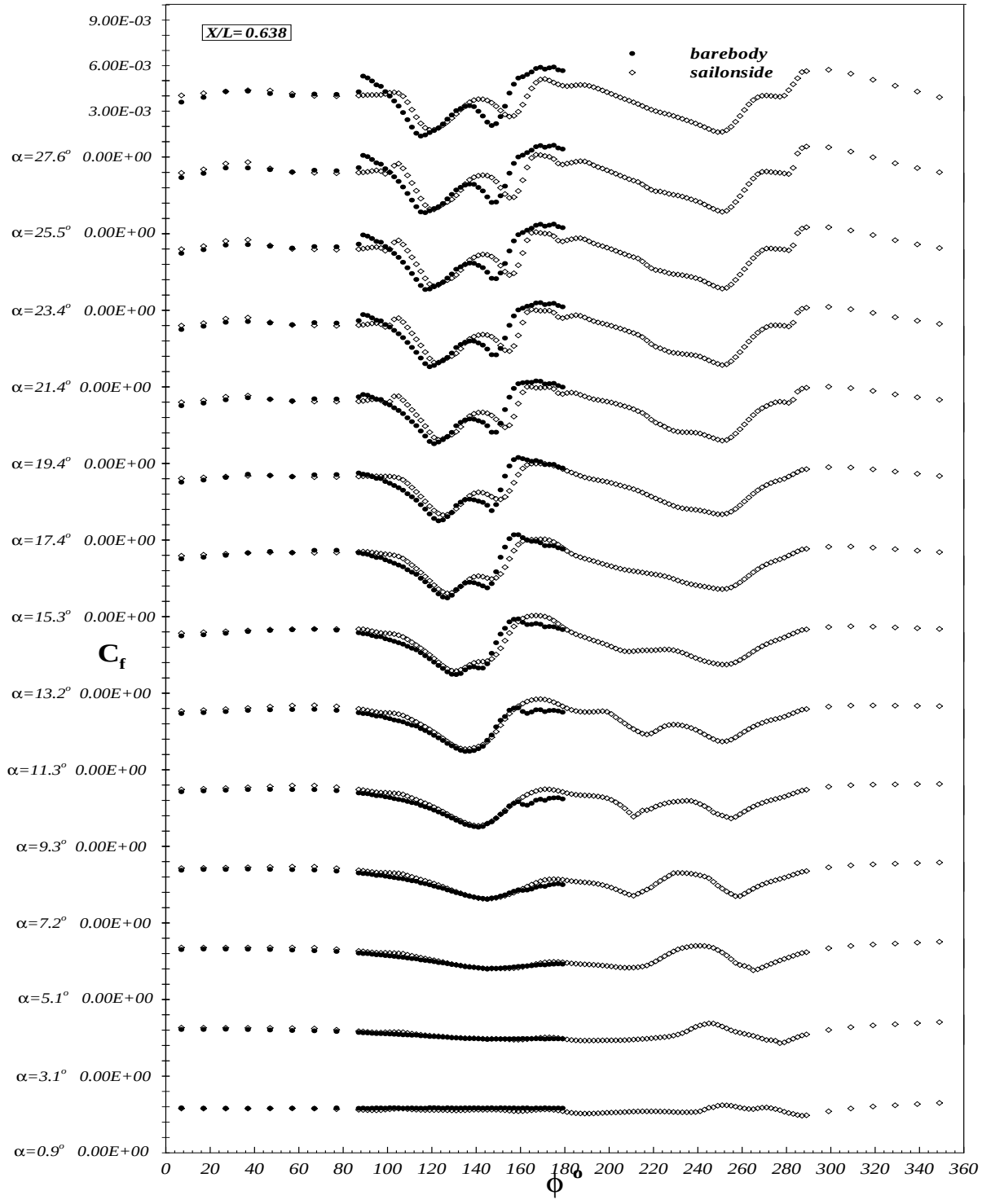

Figure 5.28: C_f vs. ϕ for all α at $x/L = 0.638$ for steady barebody and sail-on-side cases. Sail side on the right of the figure starting from $\phi = 180\,^{\circ}$.

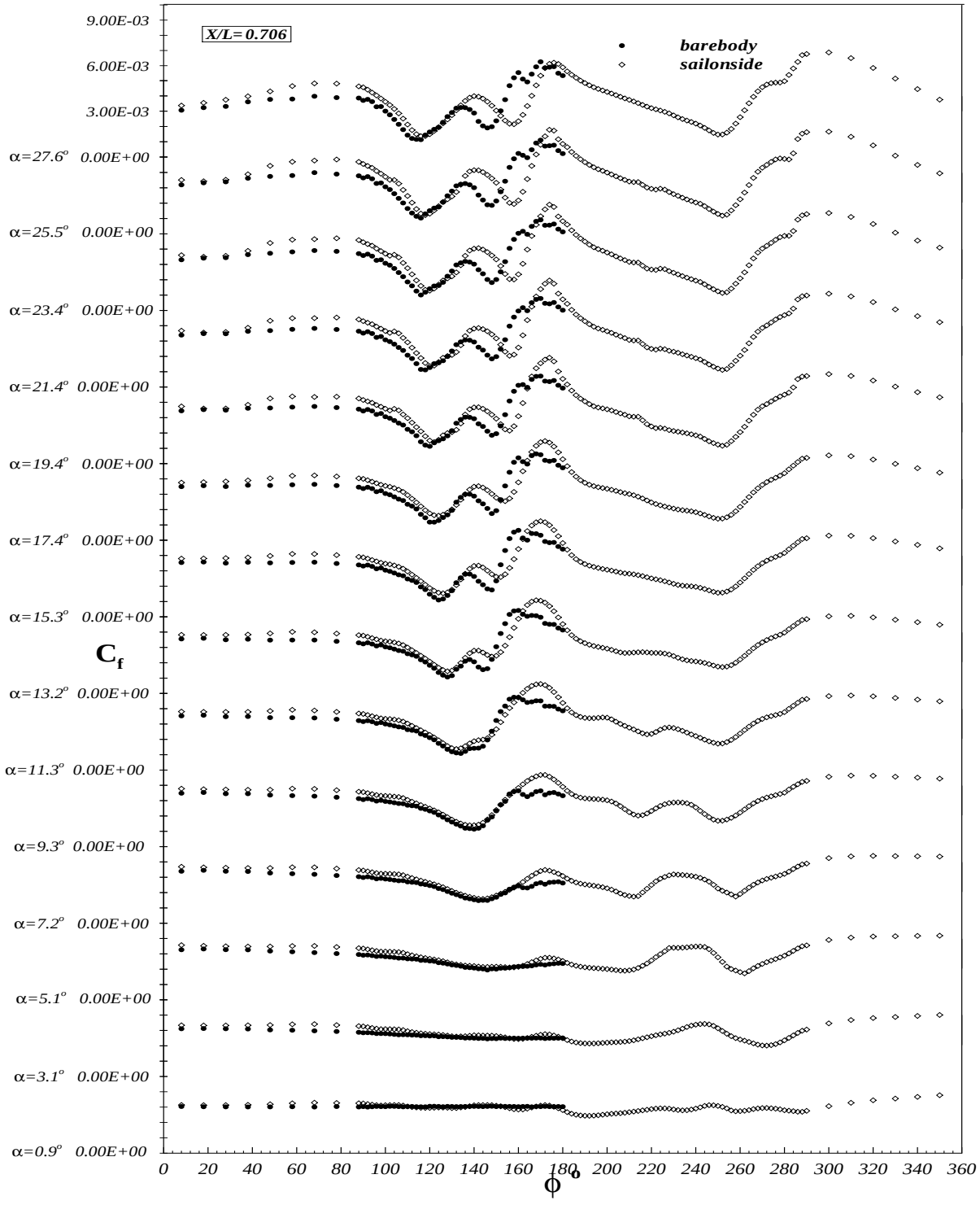

Figure 5.29: C_f vs. ϕ for all α at $x/L = 0.706$ for steady barebody and sail-on-side cases. Sail side on the right of the figure starting from $\phi = 180\,^{\circ}$.

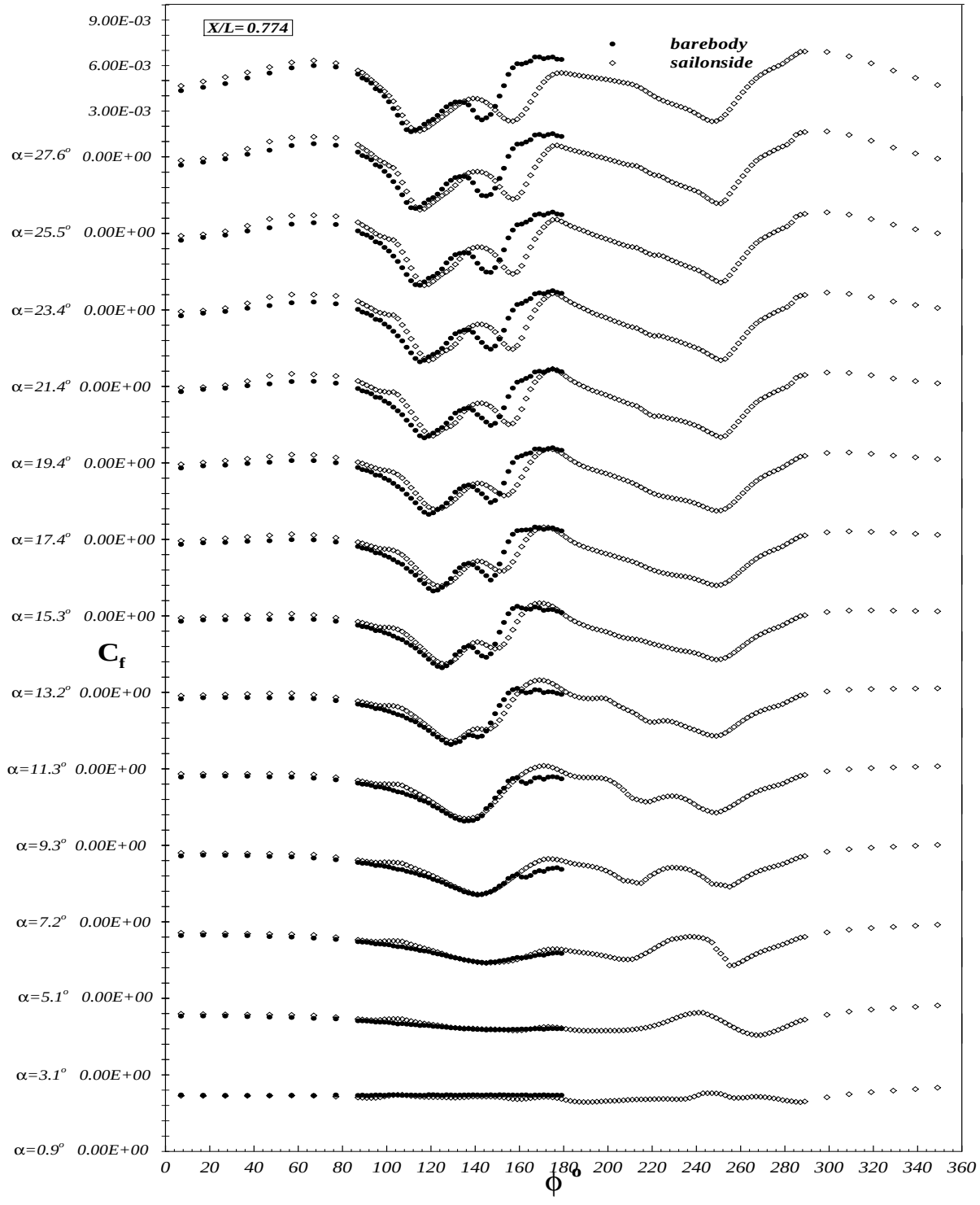

Figure 5.30: C_f vs. ϕ for all α at $x/L = 0.774$ for steady barebody and sail-on-side cases. Sail side on the right of the figure starting from $\phi = 180\,^{\circ}$.

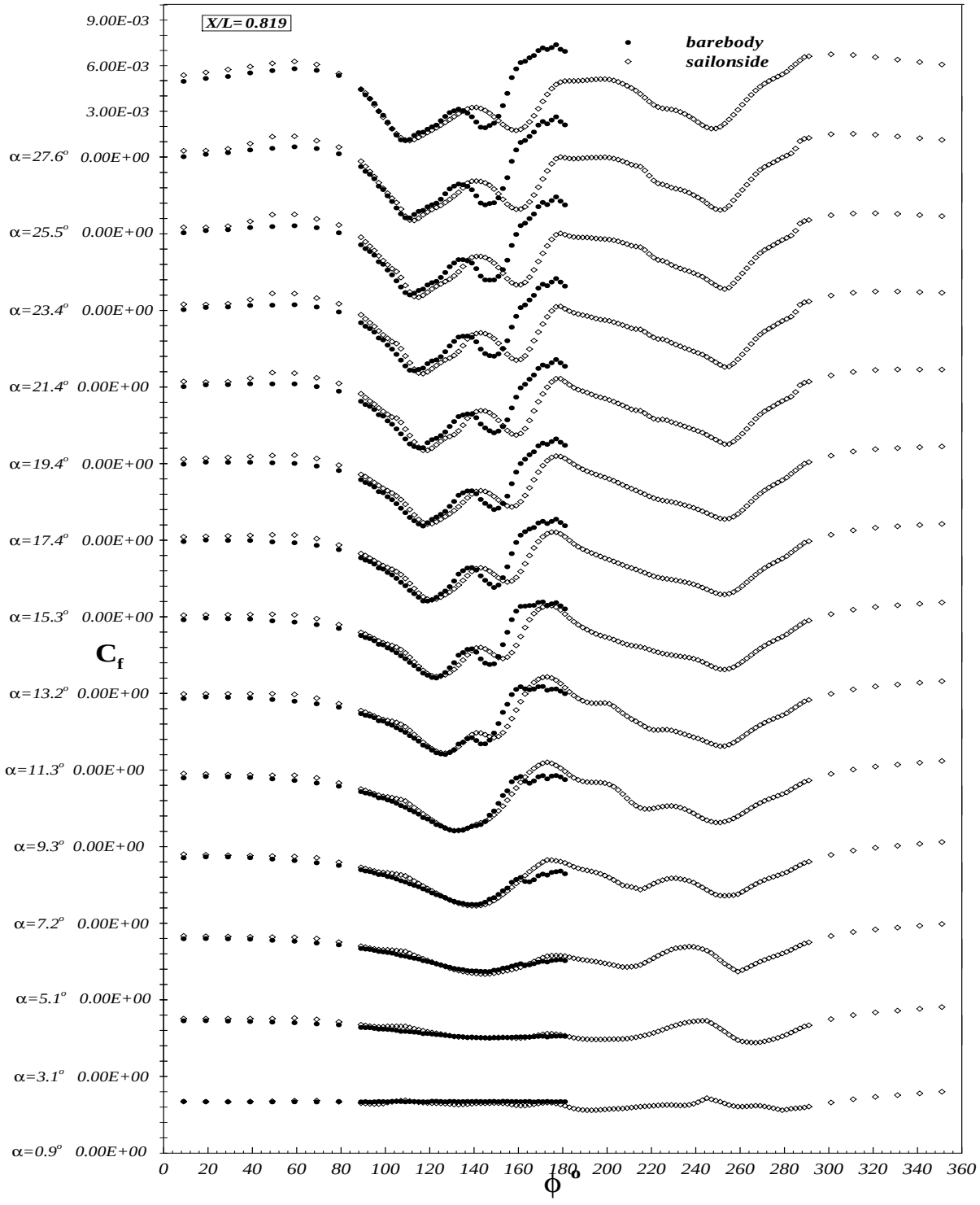

Figure 5.31: C_f vs. ϕ for all α at $x/L = 0.819$ for steady barebody and sail-on-side cases. Sail side on the right of the figure starting from $\phi = 180\,^\circ$.

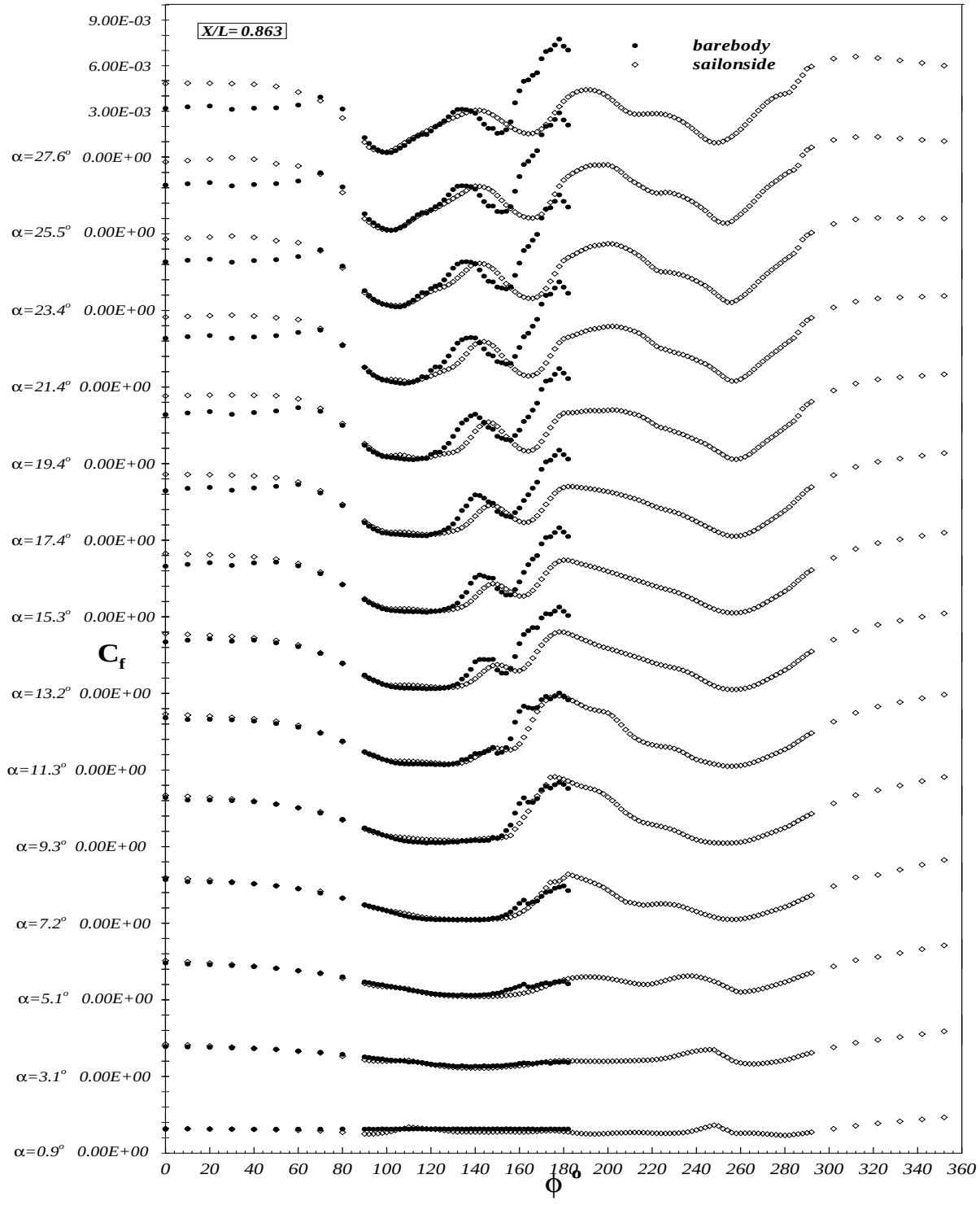

Figure 5.32: C_f vs. ϕ for all α at $x/L = 0.863$ for steady barebody and sail-on-side cases. Sail side on the right of the figure starting from $\phi = 180\,^{\circ}$.

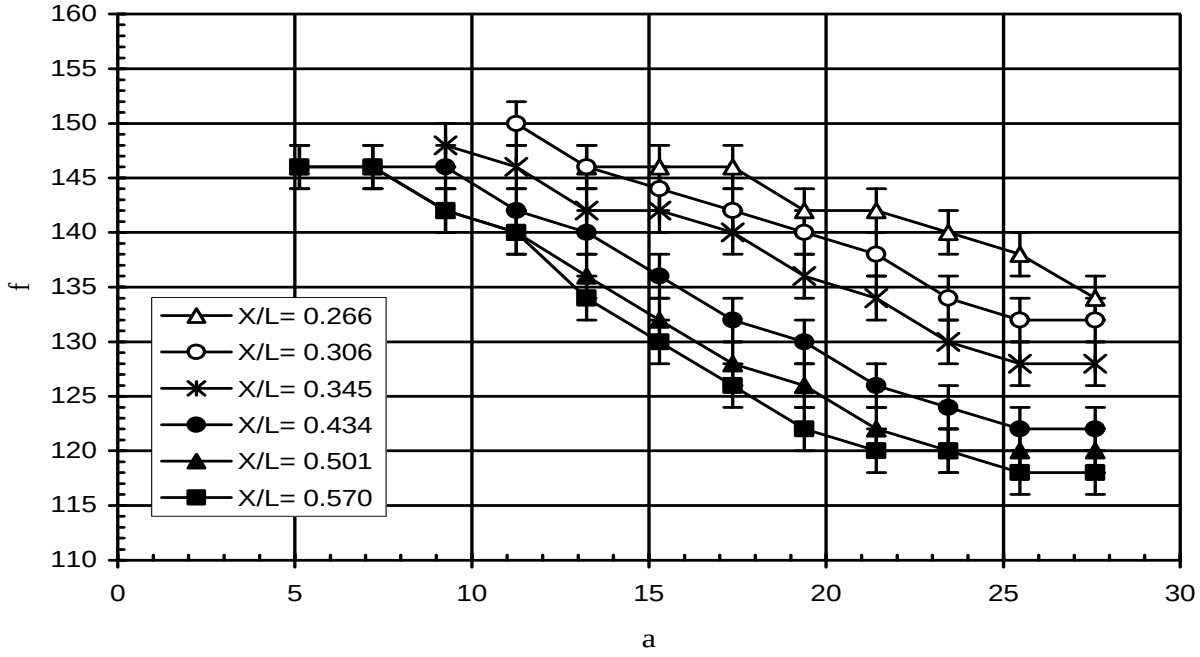

Figure 5.33: Steady primary separation locations vs. α for the barebody case.

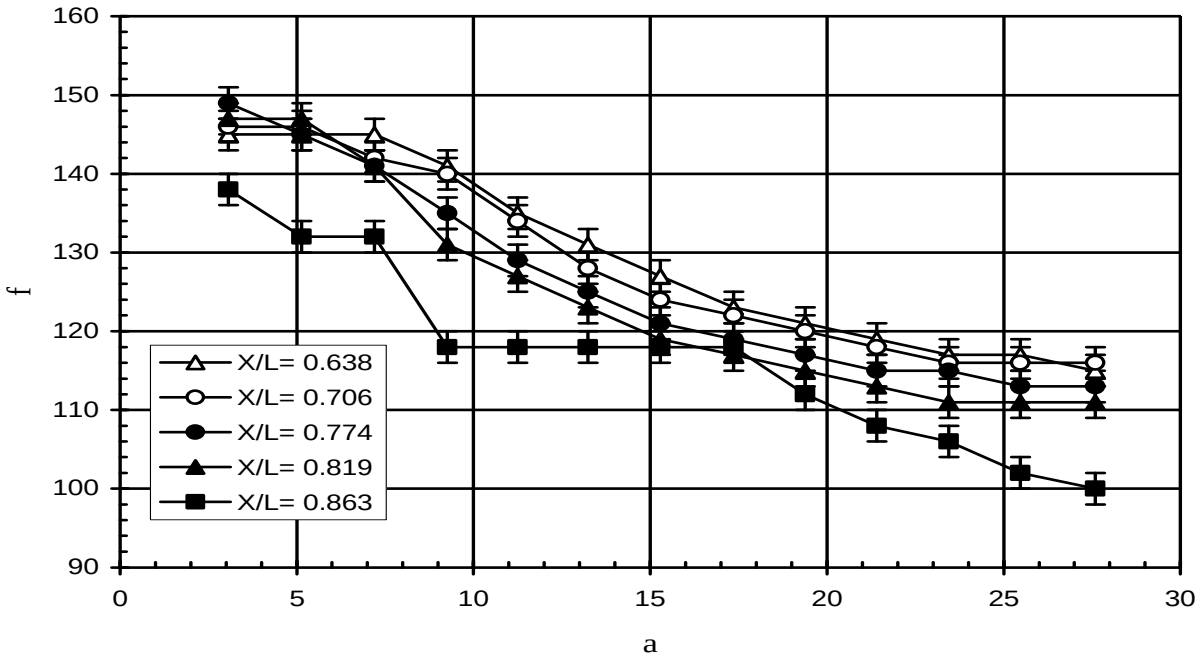

Figure 5.34: Steady primary separation locations vs. α for the barebody case (continued).

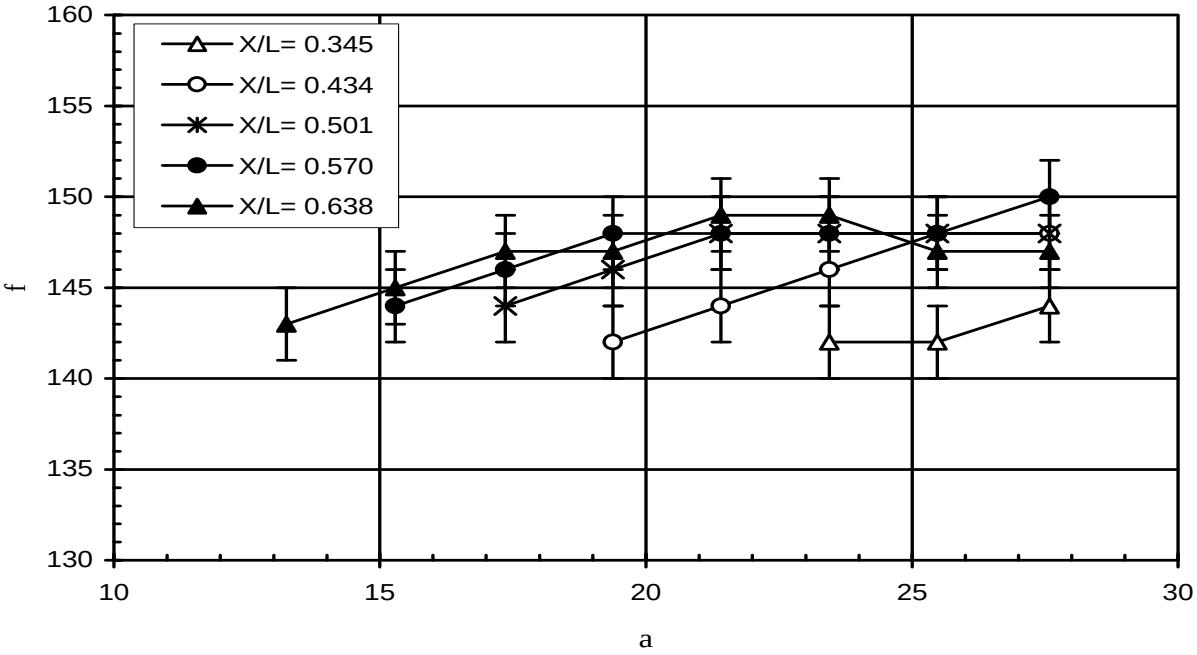

Figure 5.35: Steady secondary separation locations vs. α for the barebody case.

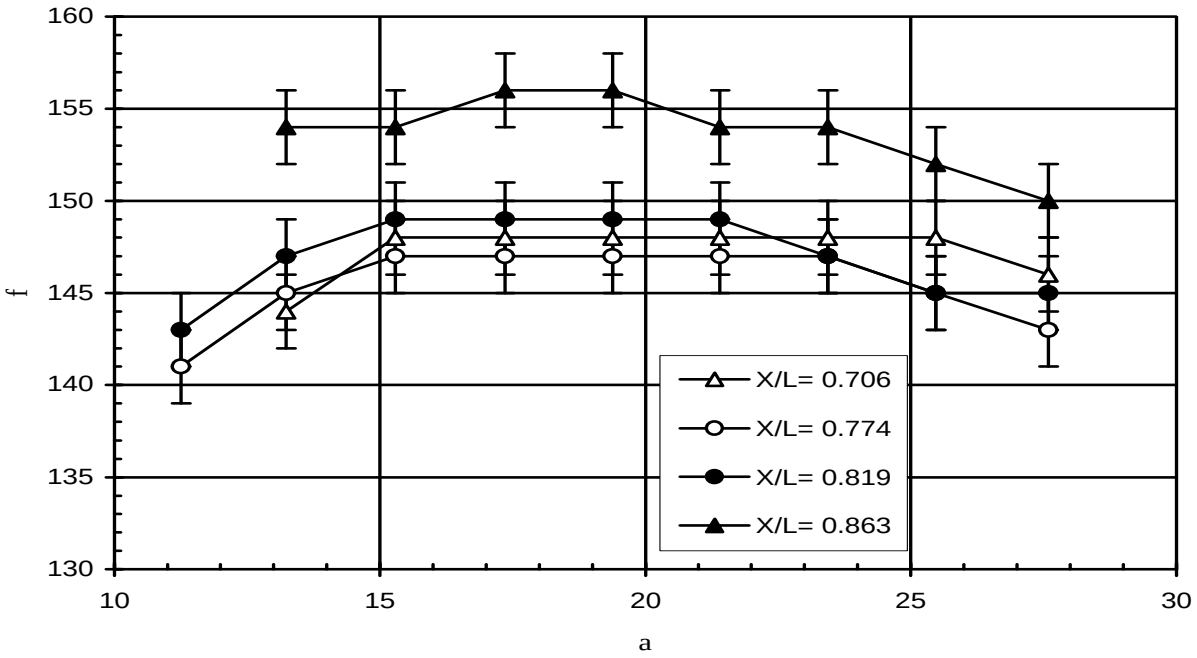

Figure 5.36: Steady secondary separation locations vs. α for the barebody case (continued).

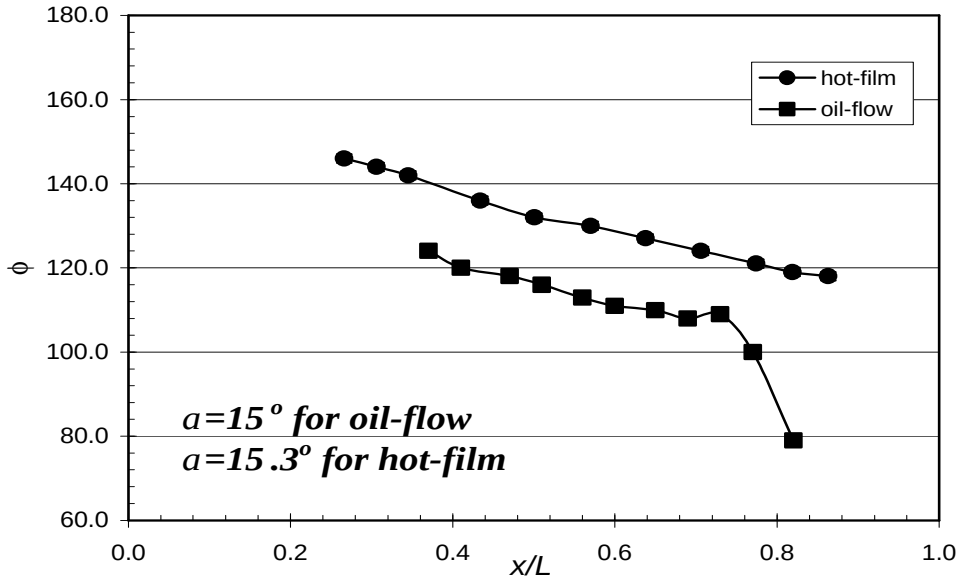

Figure 5.37: Comparison of the oil-flow primary separation locations with the hot-film primary separation locations for the barebody case. For the hot-film measurements $\alpha = 15.3\,^\circ$ and for the oil-flow results $\alpha = 15\,^\circ$.

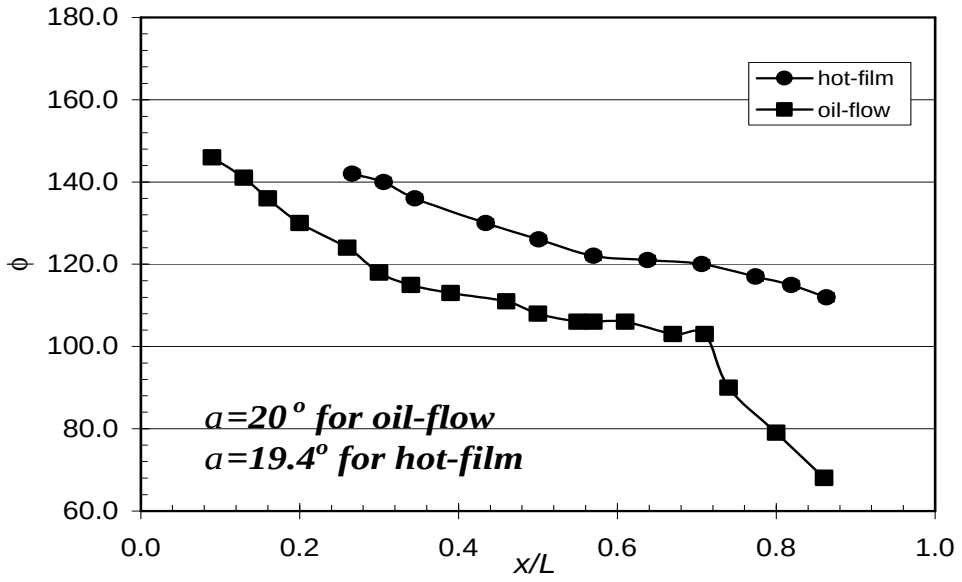

Figure 5.38: Comparison of the oil-flow primary separation locations with the hot-film primary separation locations for the barebody case. For the hot-film measurements $\alpha = 19.4\,^\circ$ and for the oil-flow results $\alpha = 20\,^\circ$.

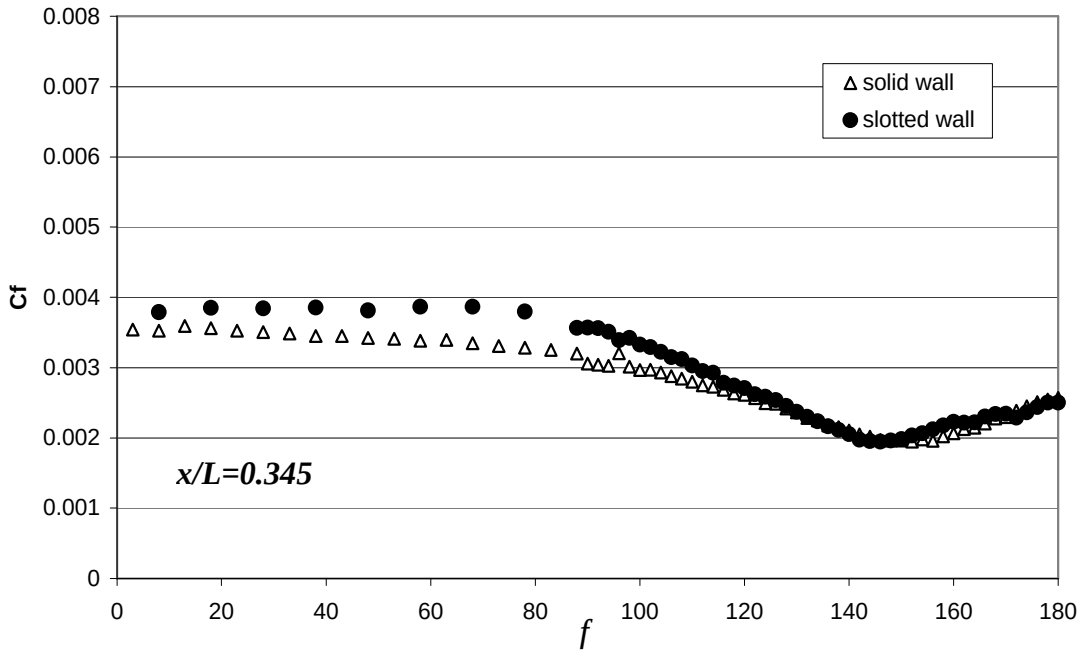

Figure 5.39: Solid vs. slotted wall comparison for the barebody C_f vs ϕ distribution at $x/L = 0.345$. $\alpha = 10\,^\circ$ for the solid wall case, and $\alpha = 9.3\,^\circ$ for the slotted wall case.

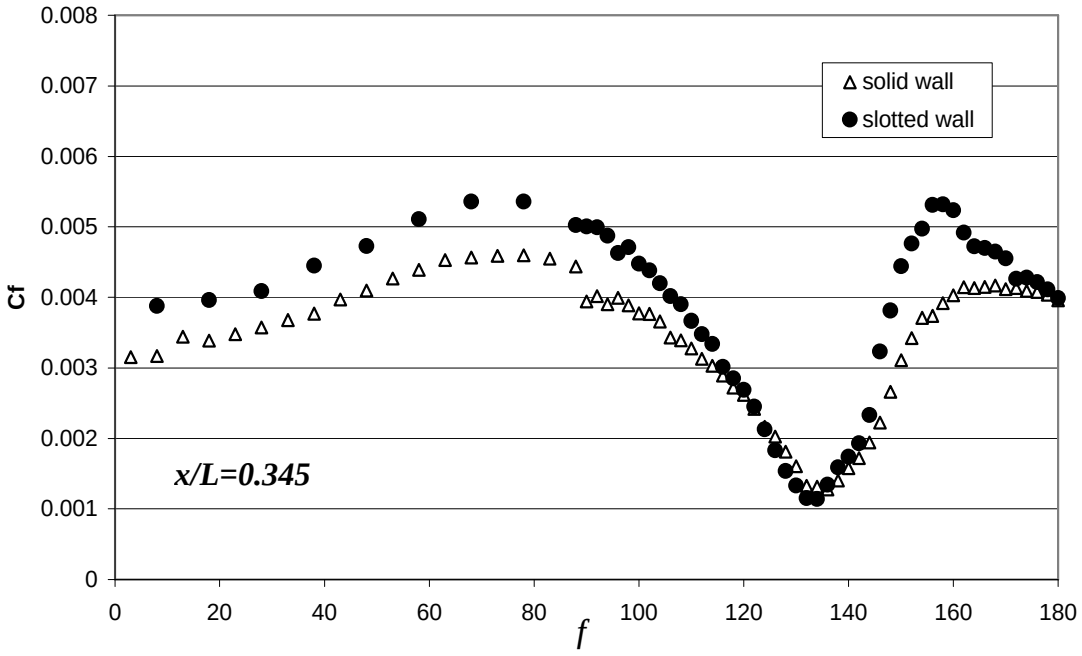

Figure 5.40: Solid vs. slotted wall comparison for the barebody C_f vs ϕ distribution at $x/L = 0.345$. $\alpha = 20\,^\circ$ for the solid wall case, and $\alpha = 19.4\,^\circ$ for the slotted wall case.

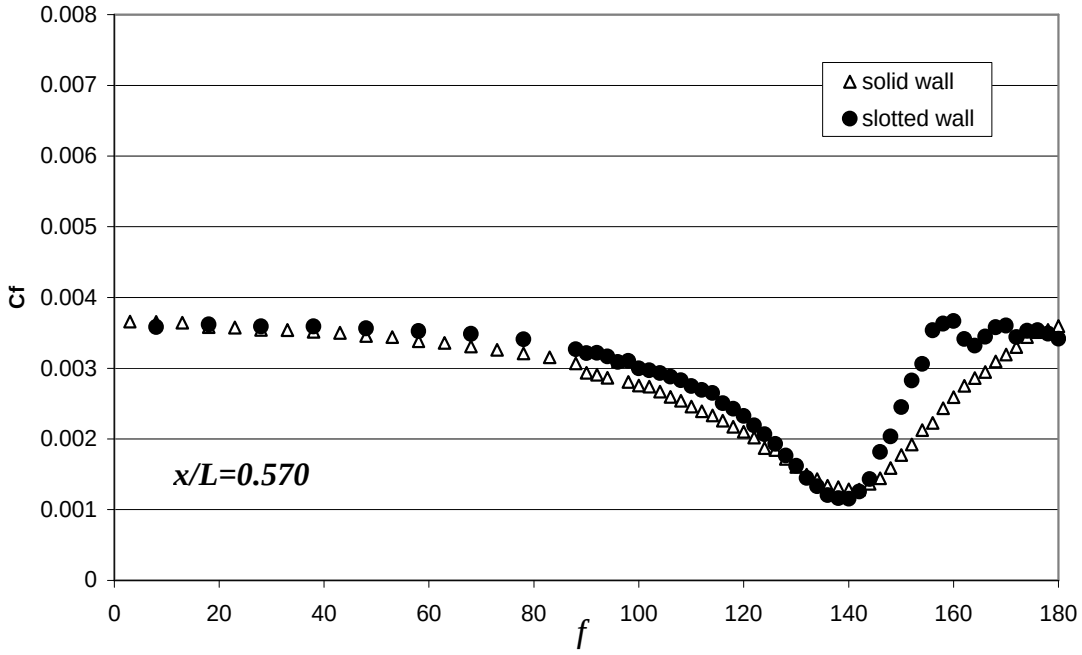

Figure 5.41: Solid vs. slotted wall comparison for the barebody C_f vs ϕ distribution at $x/L = 0.570$. $\alpha = 10\,^\circ$ for the solid wall case, and $\alpha = 9.3\,^\circ$ for the slotted wall case.

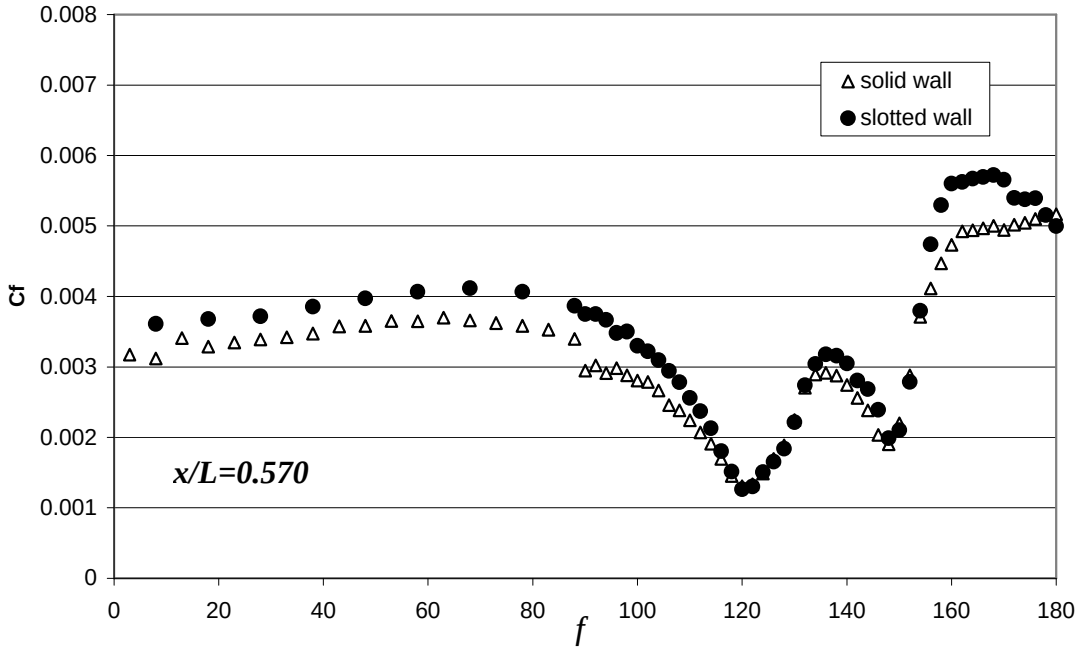

Figure 5.42: Solid vs. slotted wall comparison for the barebody C_f vs ϕ distribution at $x/L = 0.570$. $\alpha = 20\,^\circ$ for the solid wall case, and $\alpha = 19.4\,^\circ$ for the slotted wall case.

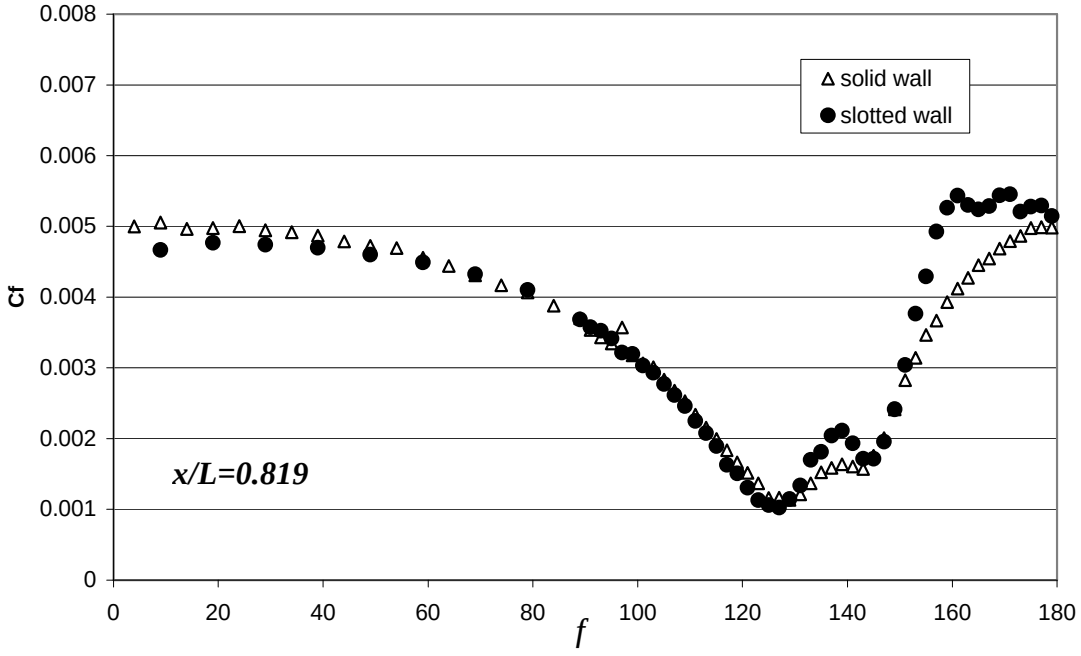

Figure 5.43: Solid vs. slotted wall comparison for the barebody C_f vs ϕ distribution at $x/L = 0.819$. $\alpha = 10\,^\circ$ for the solid wall case, and $\alpha = 9.3\,^\circ$ for the slotted wall case.

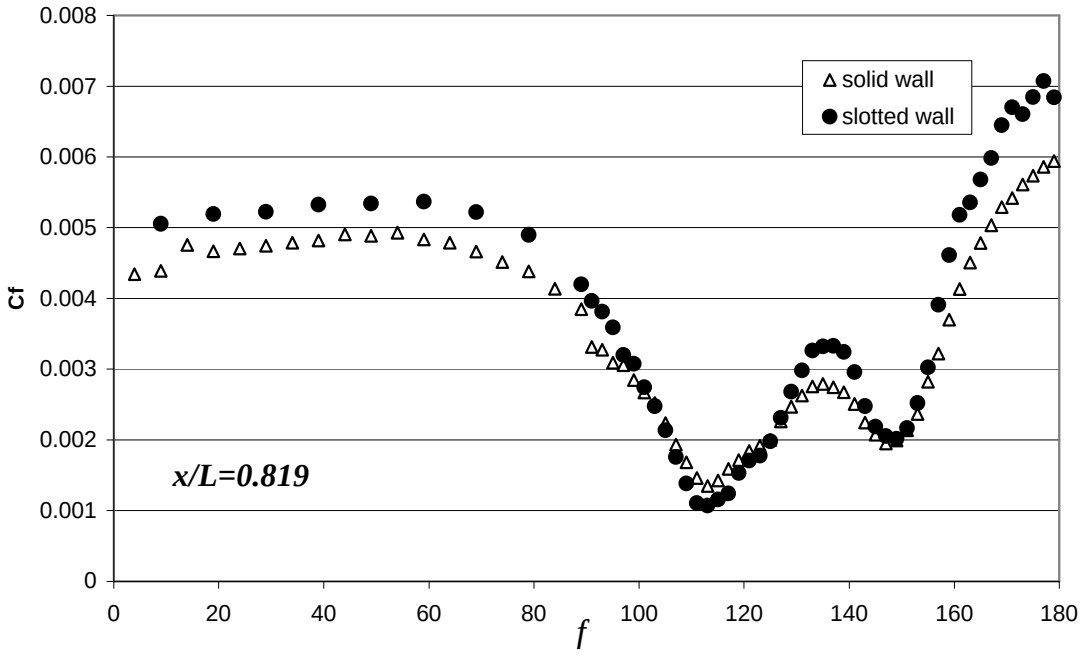

Figure 5.44: Solid vs. slotted wall comparison for the barebody C_f vs ϕ distribution at $x/L = 0.819$. $\alpha = 20\,^\circ$ for the solid wall case, and $\alpha = 19.4\,^\circ$ for the slotted wall case.

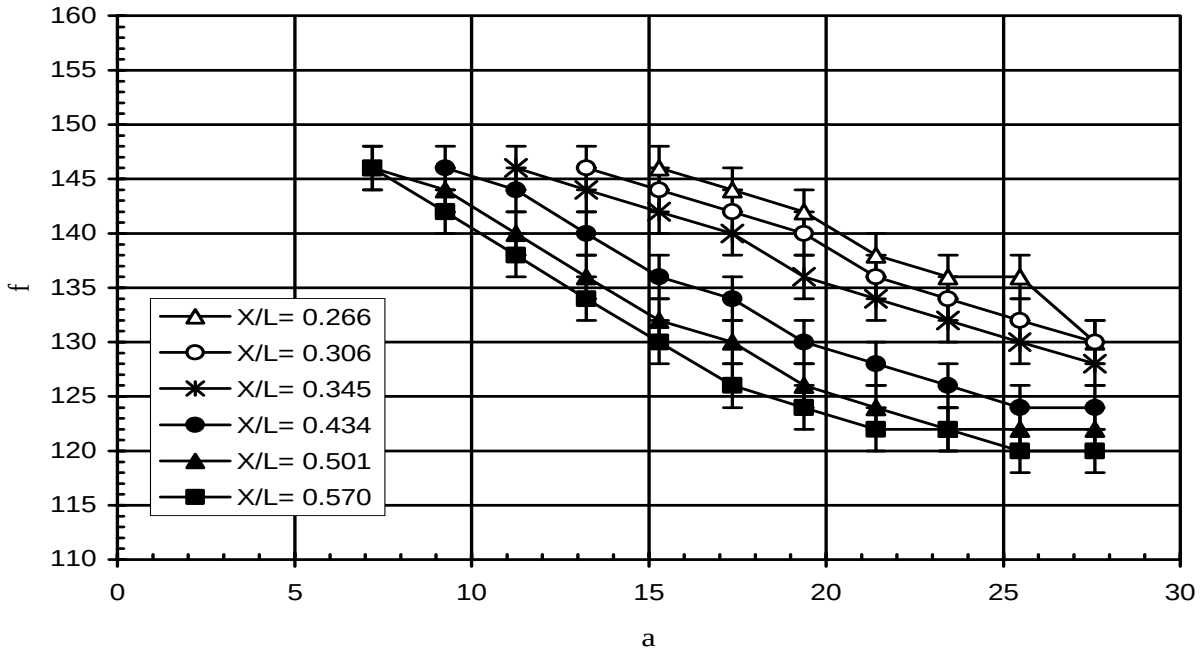

Figure 5.45: Steady primary separation locations vs. α for the sail-on-side (region without sail) case.

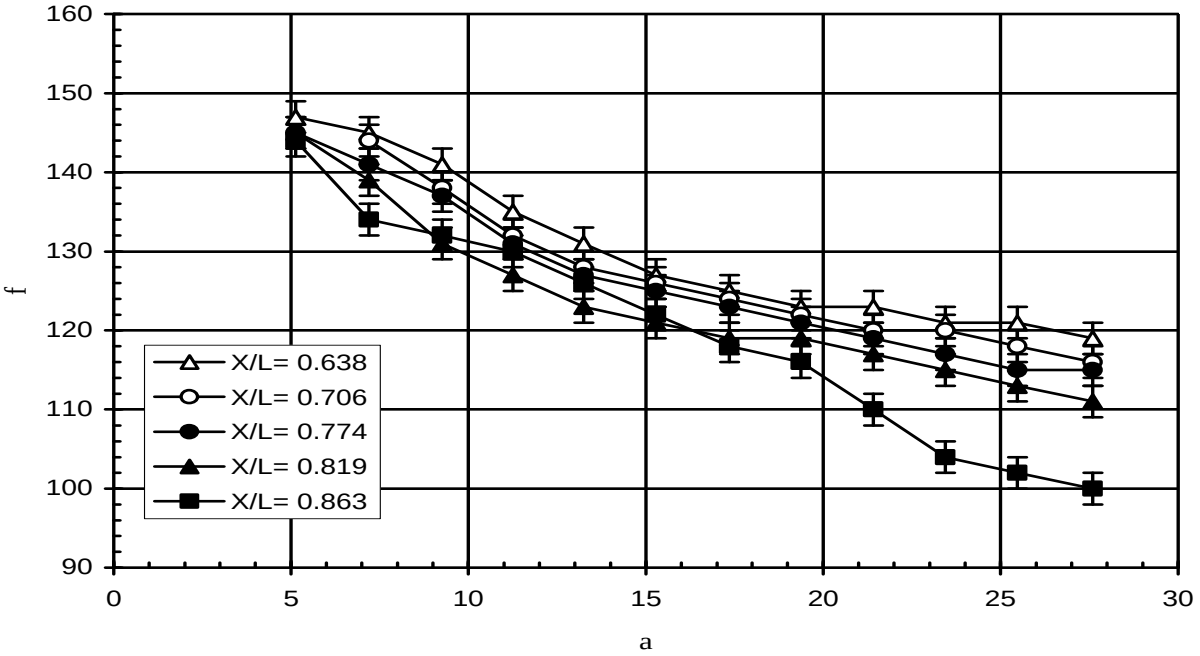

Figure 5.46: Steady primary separation locations vs. α for the sail-on-side (region without sail) case (continued).

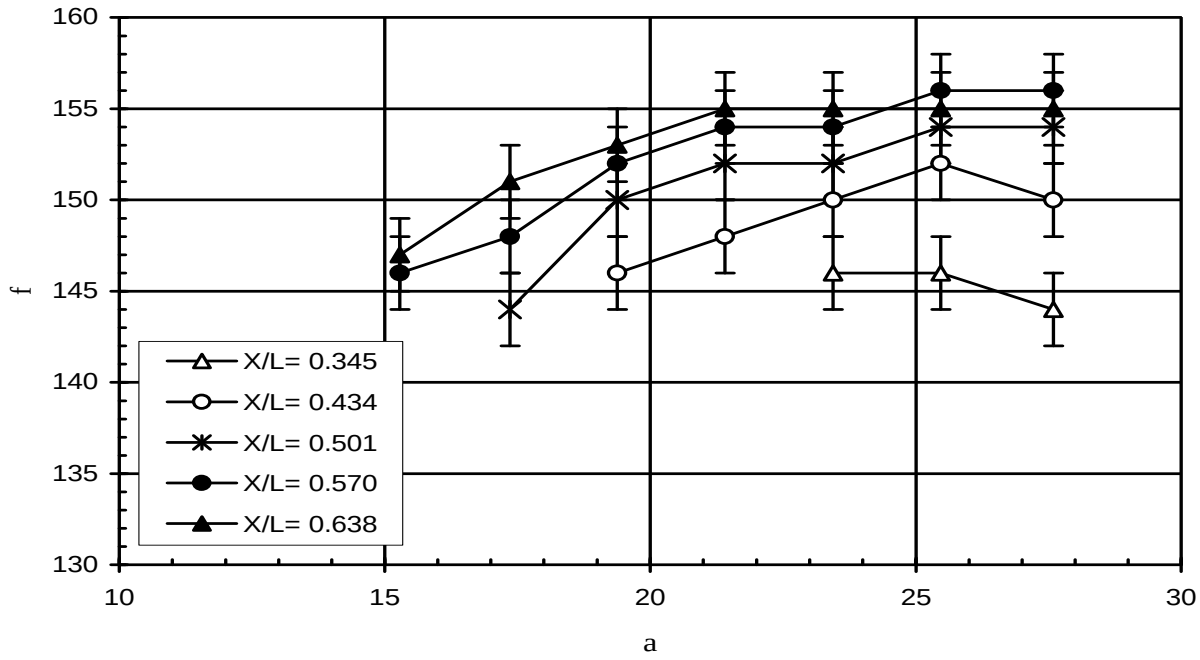

Figure 5.47: Steady secondary separation locations vs. α for the sail-on-side (region without sail) case.

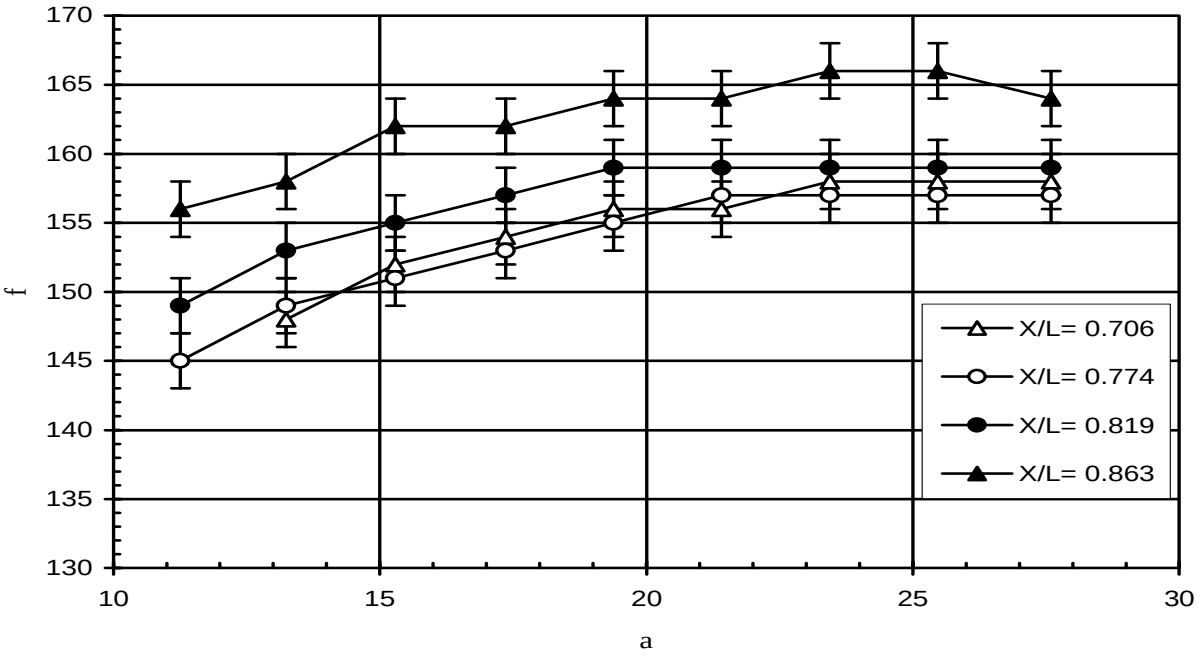

Figure 5.48: Steady secondary separation locations vs. α for the sail-on-side (region without sail) case (continued).

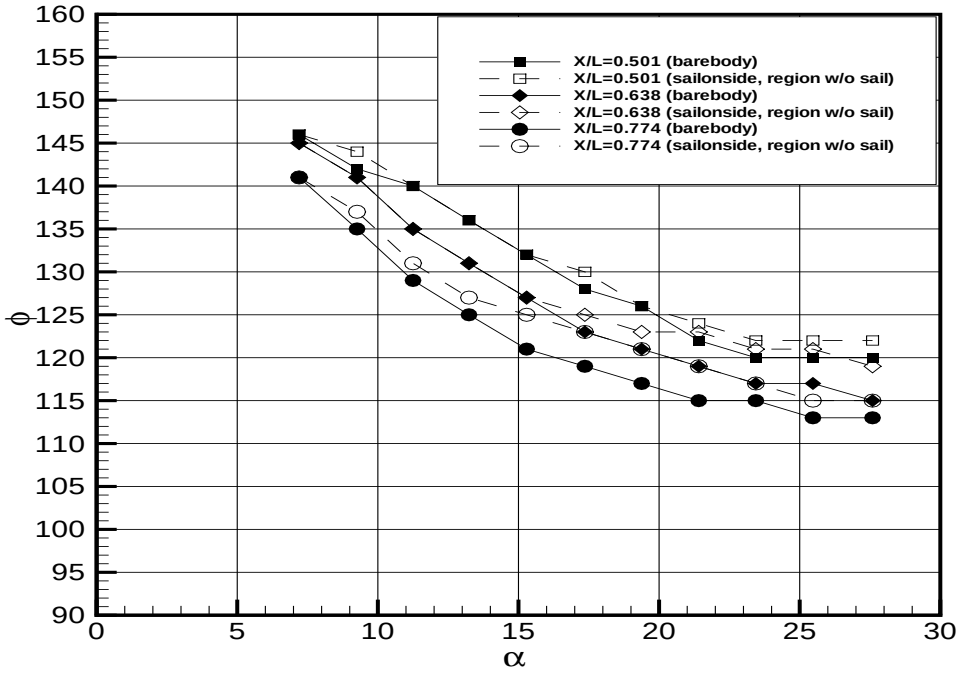

Figure 5.49: Comparison for steady primary separation locations vs. α for barebody and the sail-on-side (region without sail) case at $x/L = 0.501$, 0.638 and 0.774.

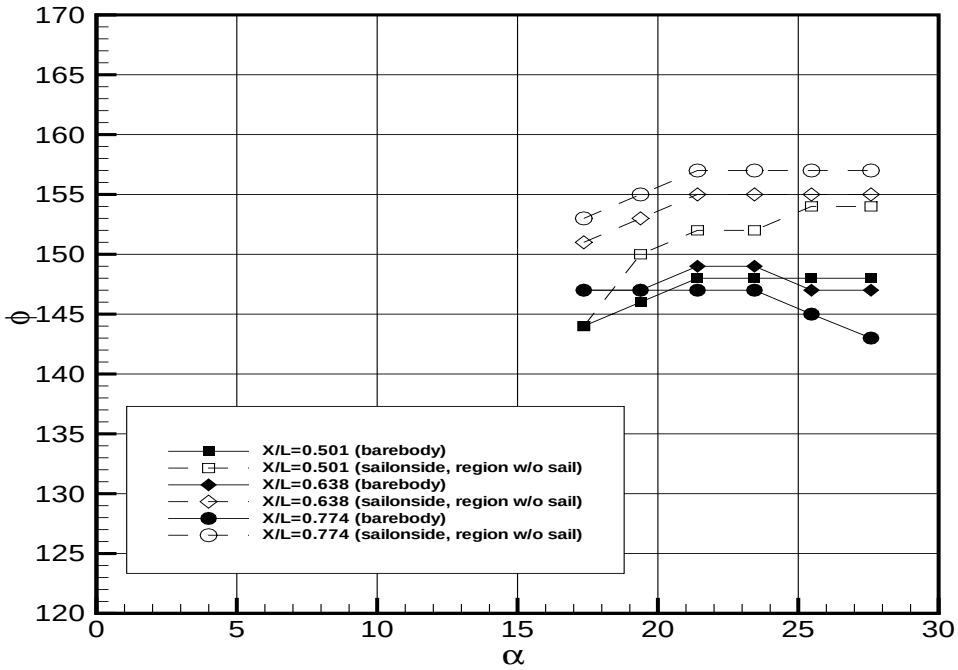

Figure 5.50: Comparison for steady secondary separation locations vs. α for barebody and the sail-on-side (region without sail) case at $x/L = 0.501$, 0.638 and 0.774.

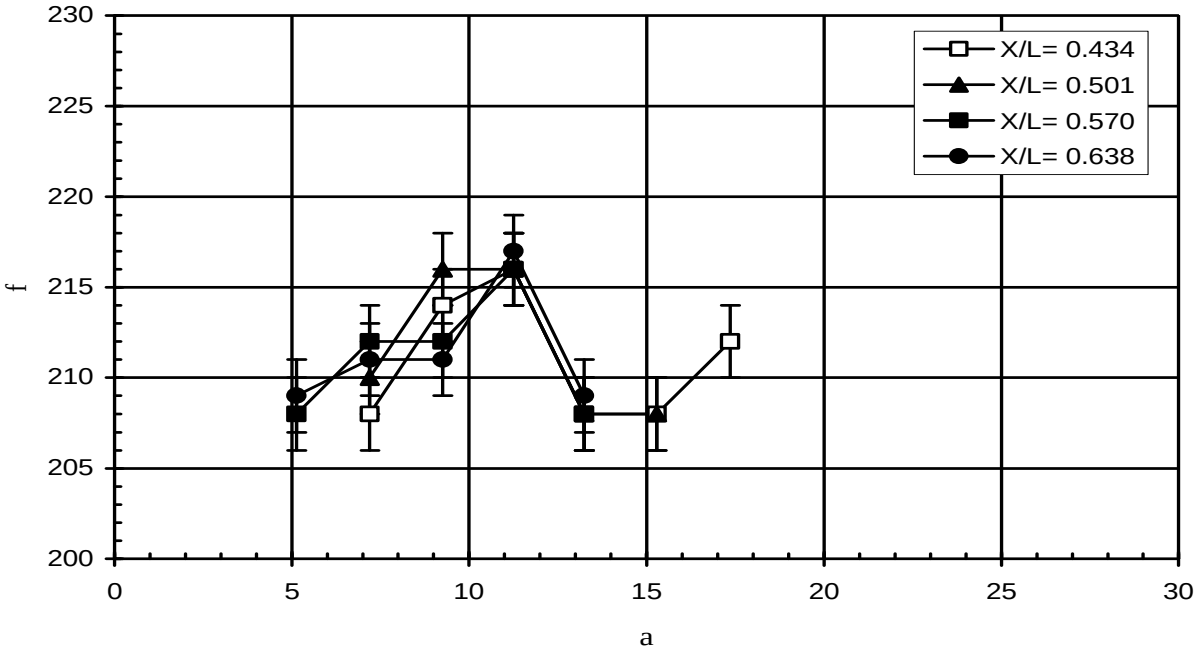

Figure 5.51: Steady 1^{st} separation locations vs. α for the sail-on-side (region with sail) case.

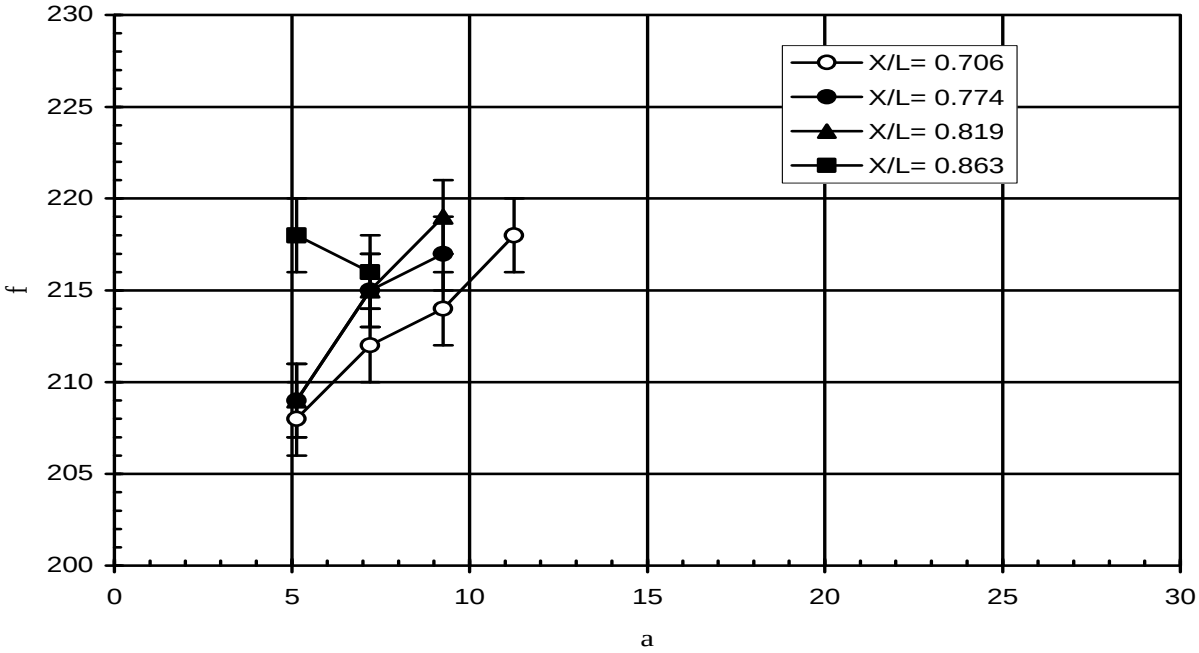

Figure 5.52: Steady 1^{st} separation locations vs. α for the sail-on-side (region with sail) case (continued).

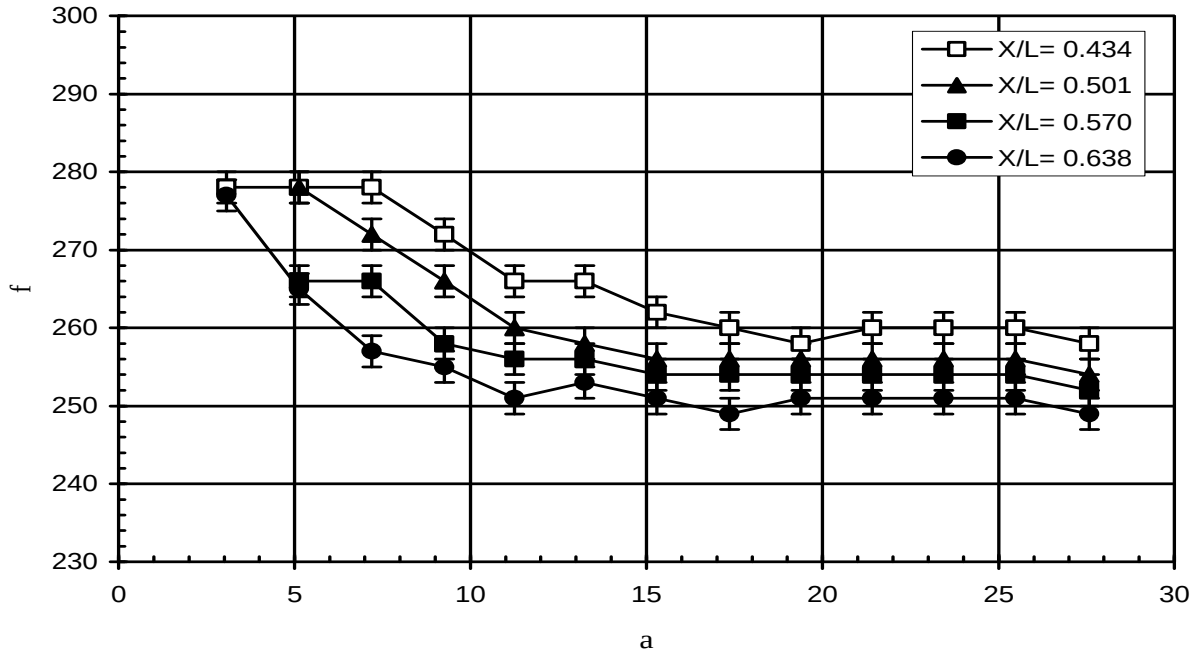

Figure 5.53: Steady 2^{nd} separation locations vs. α for the sail-on-side (region with sail) case.

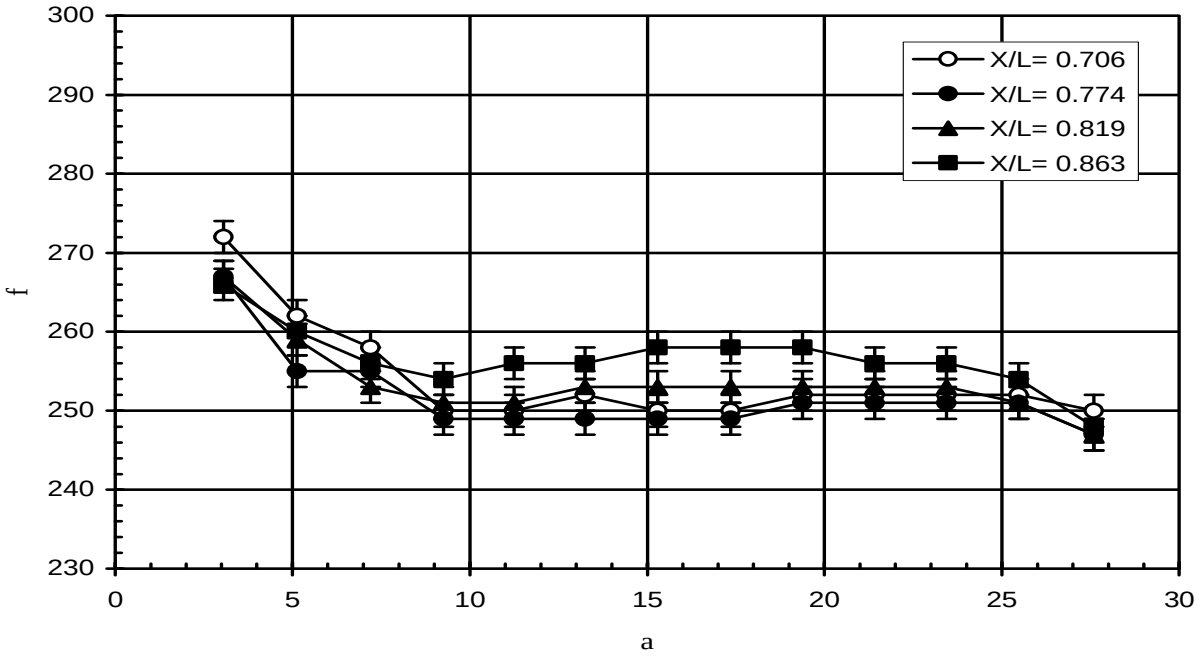

Figure 5.54: Steady 2^{nd} separation locations vs. α for the sail-on-side (region with sail) case (continued)

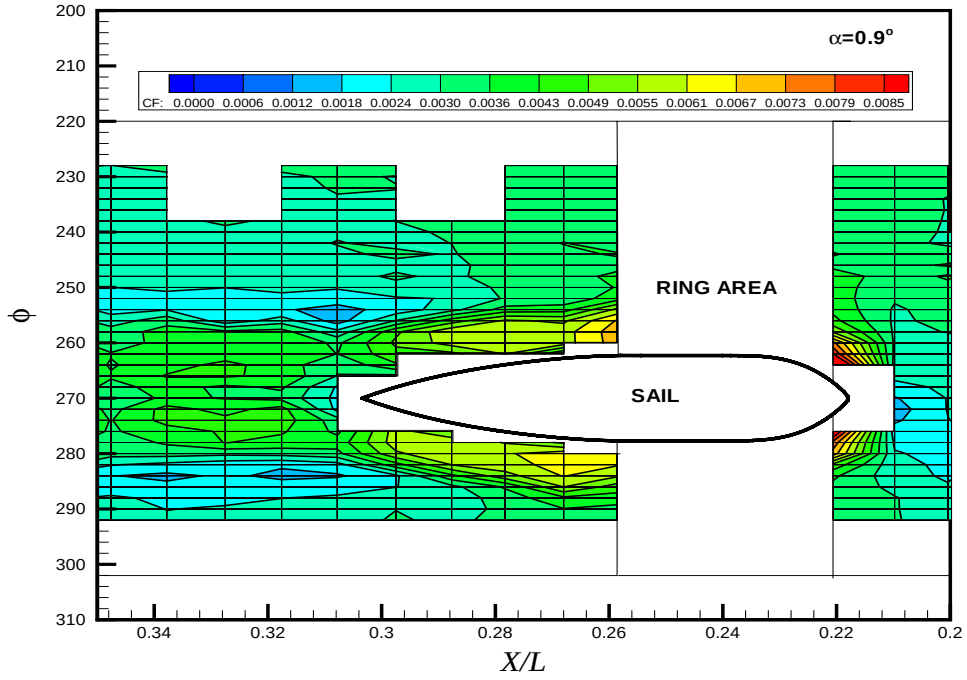

Figure 5.55: Steady C_f contours in the vicinity of sail at $\alpha = 0.9\,^\circ$.

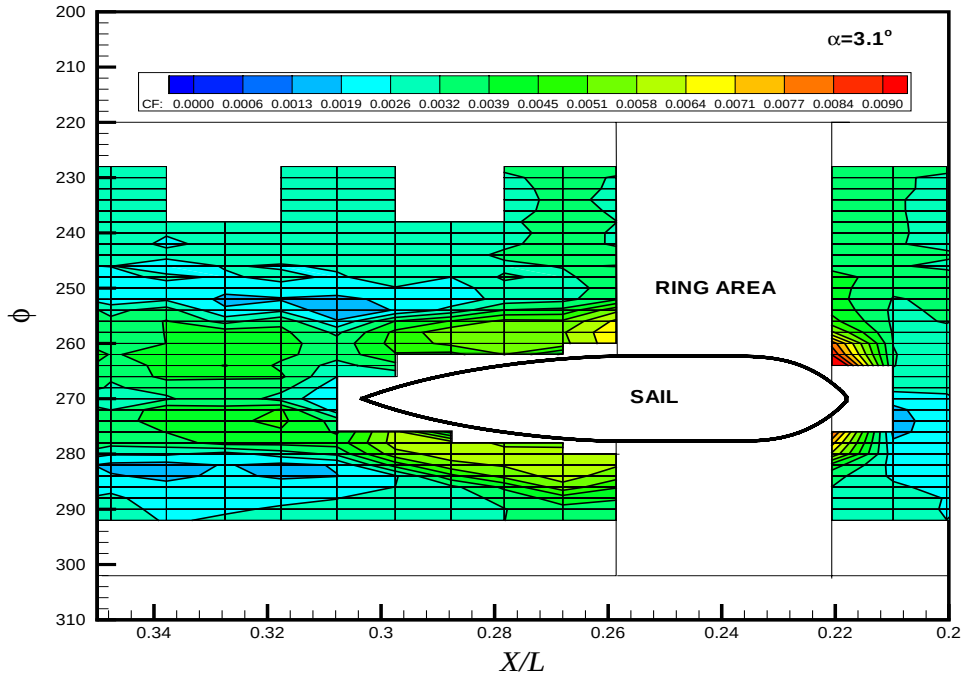

Figure 5.56: Steady C_f contours in the vicinity of sail at $\alpha = 3.1\,^\circ$.

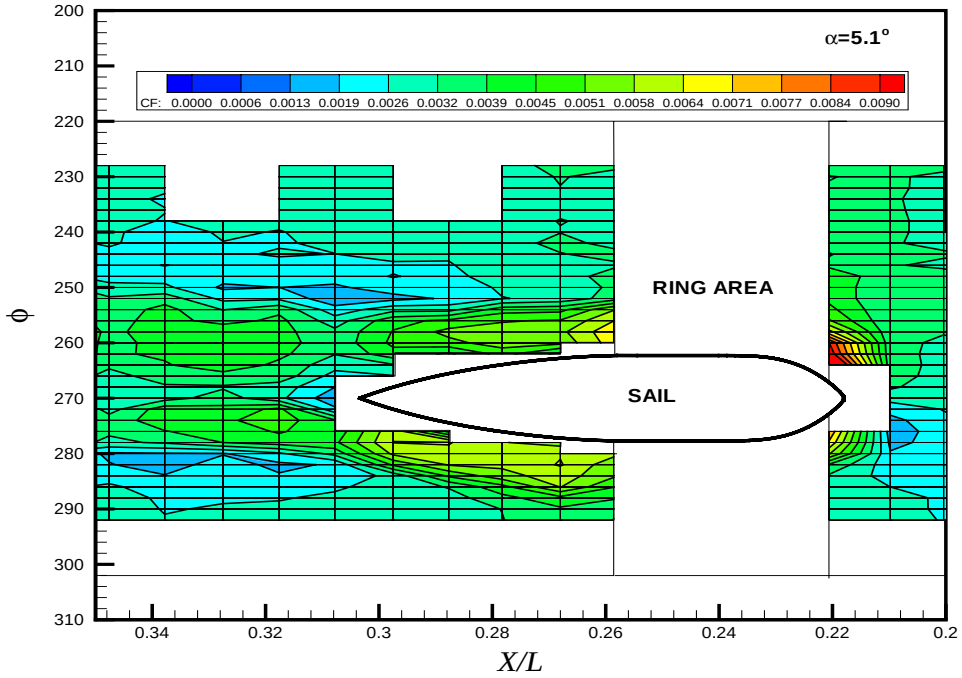

Figure 5.57: Steady C_f contours in the vicinity of sail at $\alpha = 5.1\,^{\circ}$.

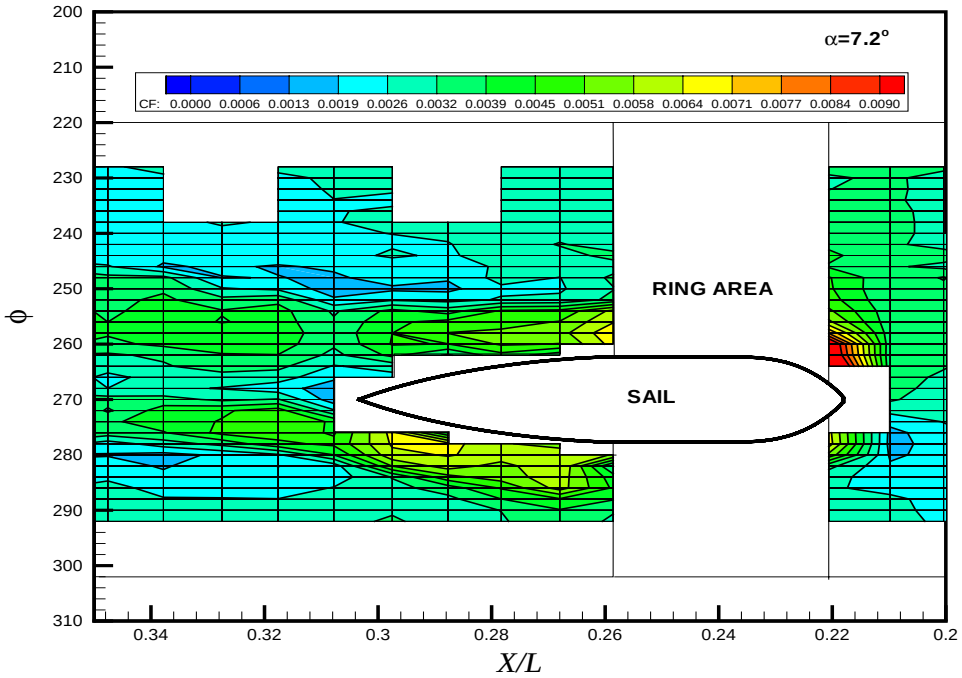

Figure 5.58: Steady C_f contours in the vicinity of sail at $\alpha = 7.2\,^{\circ}$.

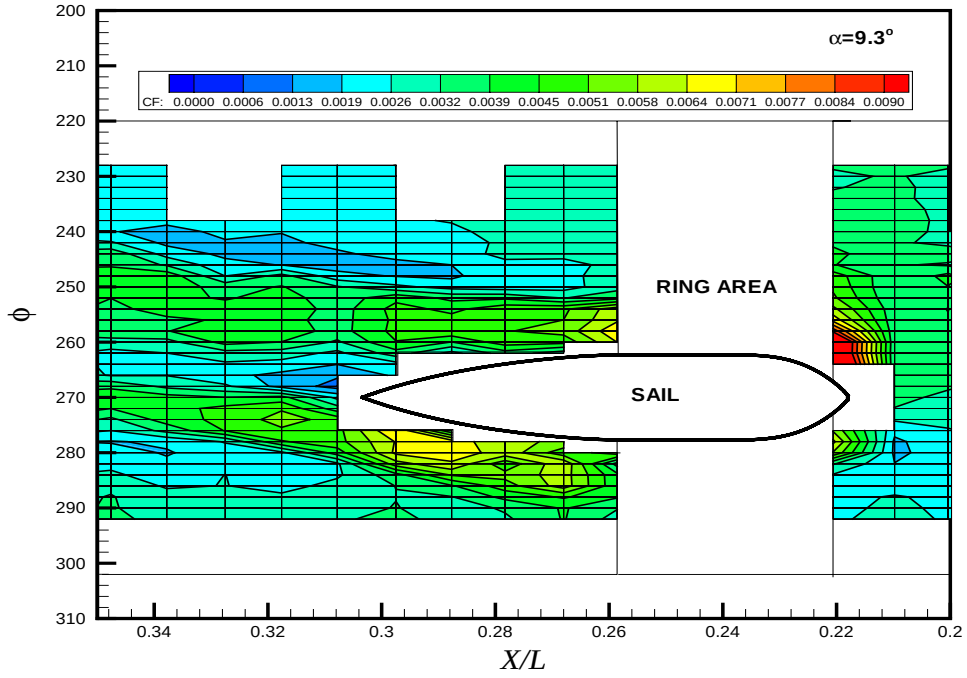

Figure 5.59: Steady C_f contours in the vicinity of sail at $\alpha = 9.3\,^\circ$.

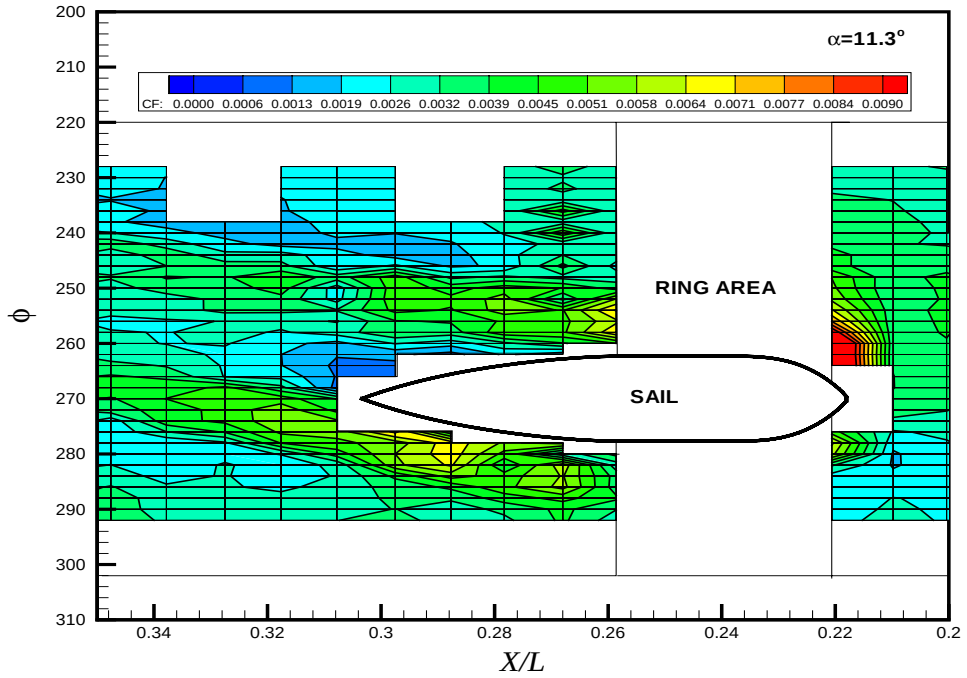

Figure 5.60: Steady C_f contours in the vicinity of sail at $\alpha = 11.3\,^\circ$.

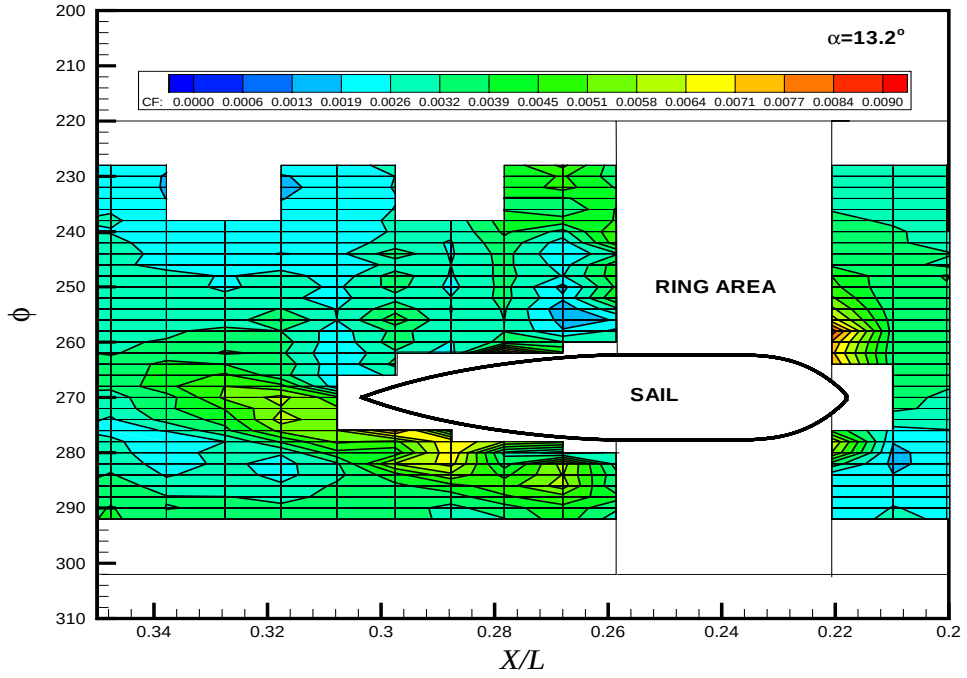

Figure 5.61: Steady C_f contours in the vicinity of sail at $\alpha = 13.2\,^\circ$.

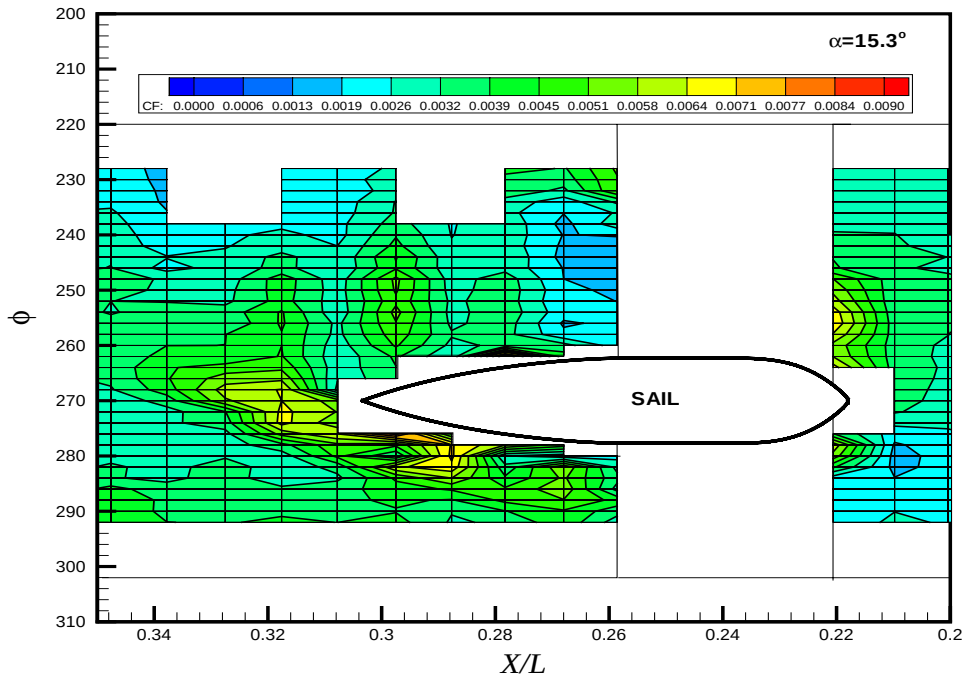

Figure 5.62: Steady C_f contours in the vicinity of sail at $\alpha = 15.3\,^\circ$.

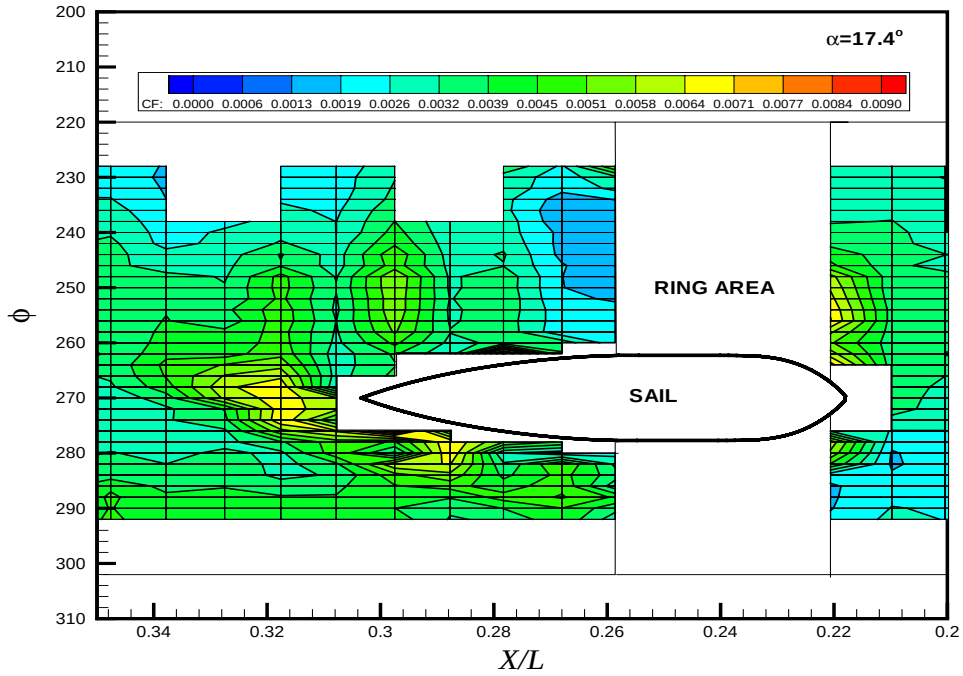

Figure 5.63: Steady C_f contours in the vicinity of sail at $\alpha = 17.4\,^\circ$.

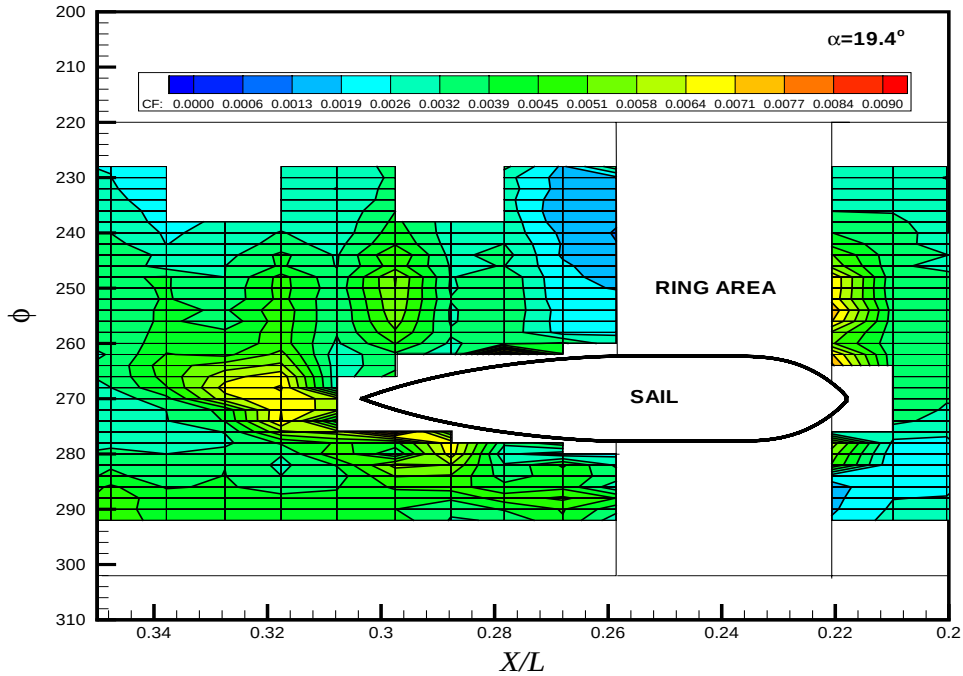

Figure 5.64: Steady C_f contours in the vicinity of sail at $\alpha = 19.4\,^\circ$.

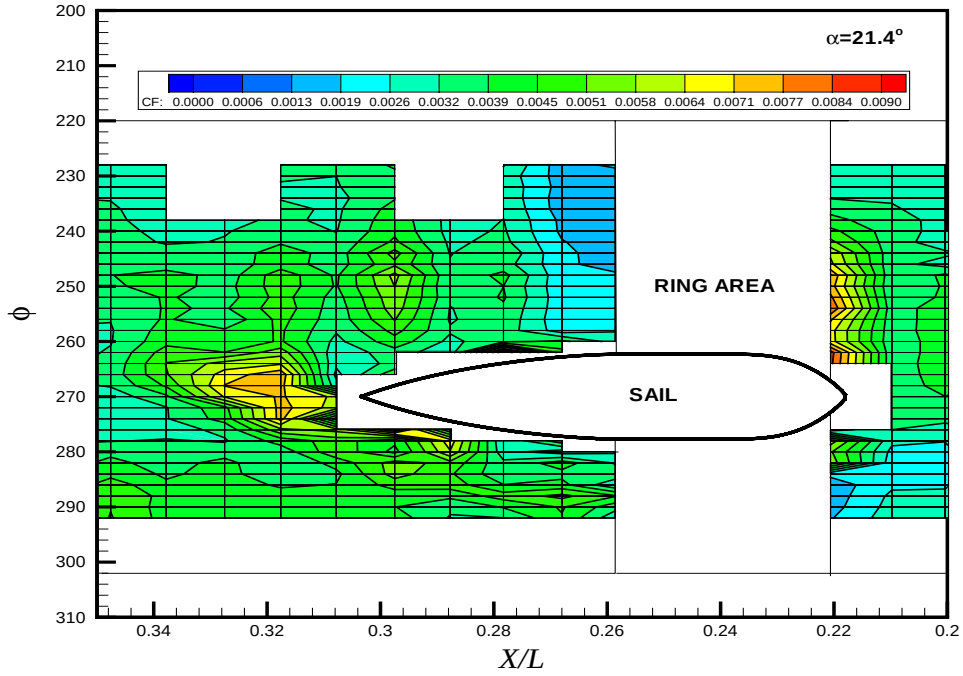

Figure 5.65: Steady C_f contours in the vicinity of sail at $\alpha = 21.4\,^\circ$.

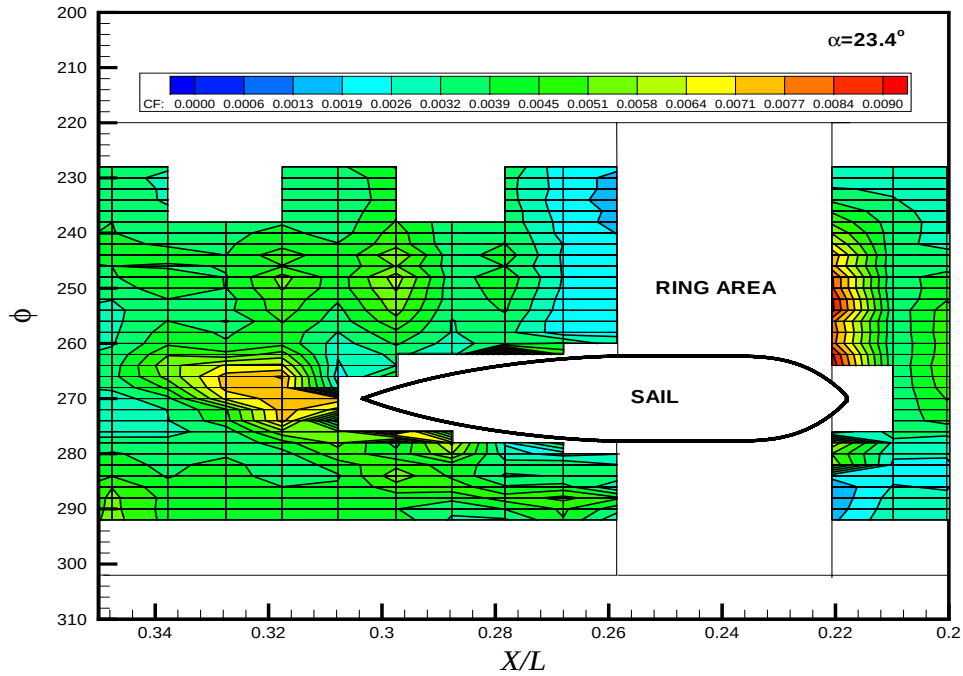

Figure 5.66: Steady C_f contours in the vicinity of sail at $\alpha = 23.4\,^\circ$.

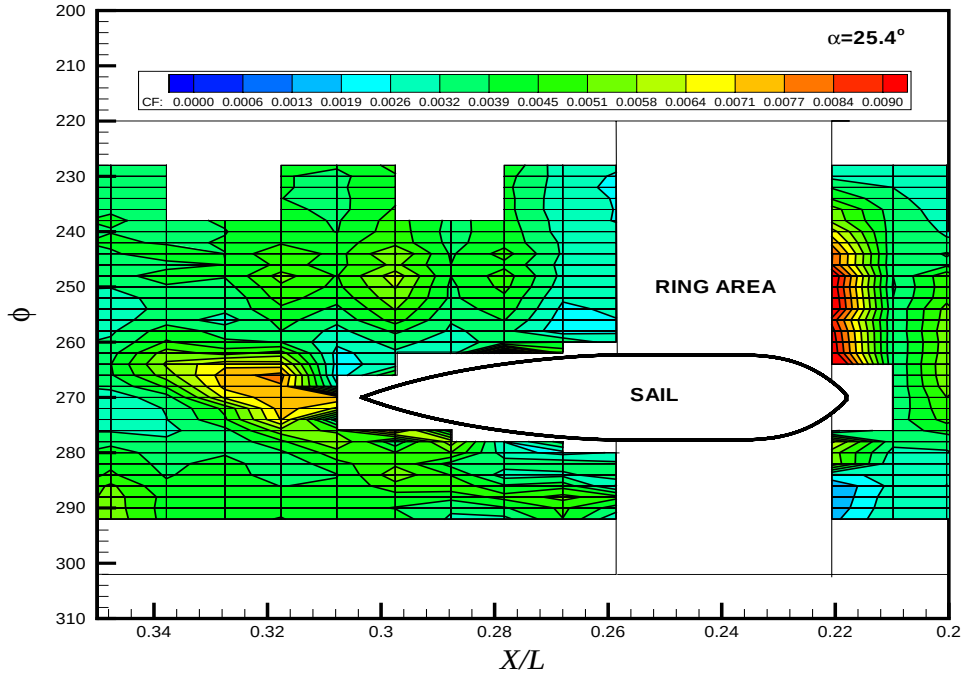

Figure 5.67: Steady C_f contours in the vicinity of sail at $\alpha = 25.5\,^\circ$.

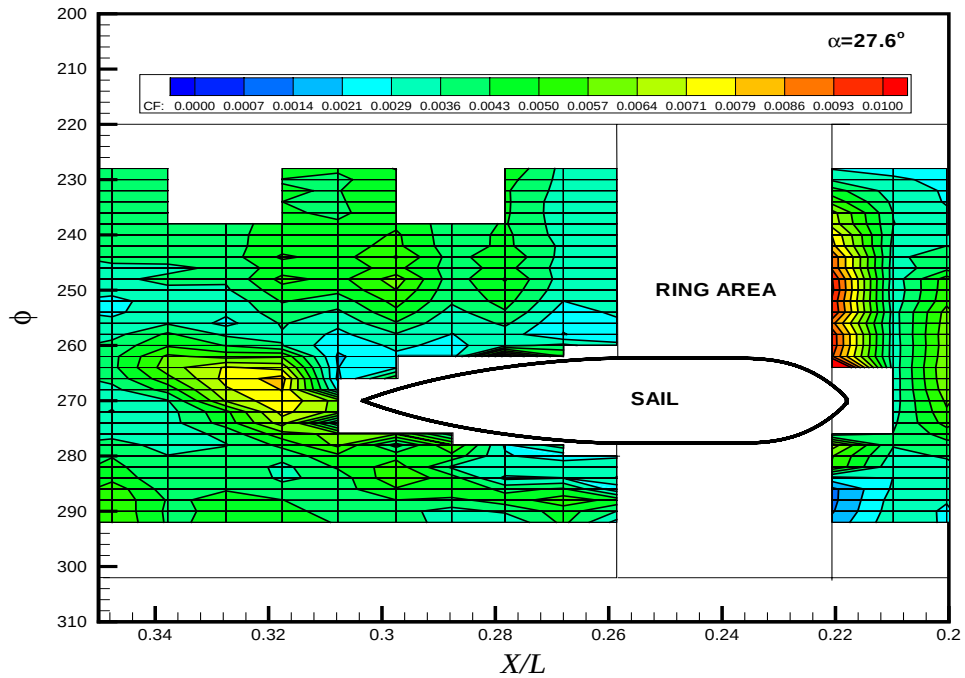

Figure 5.68: Steady C_f contours in the vicinity of sail at $\alpha = 27.6\,^\circ$.

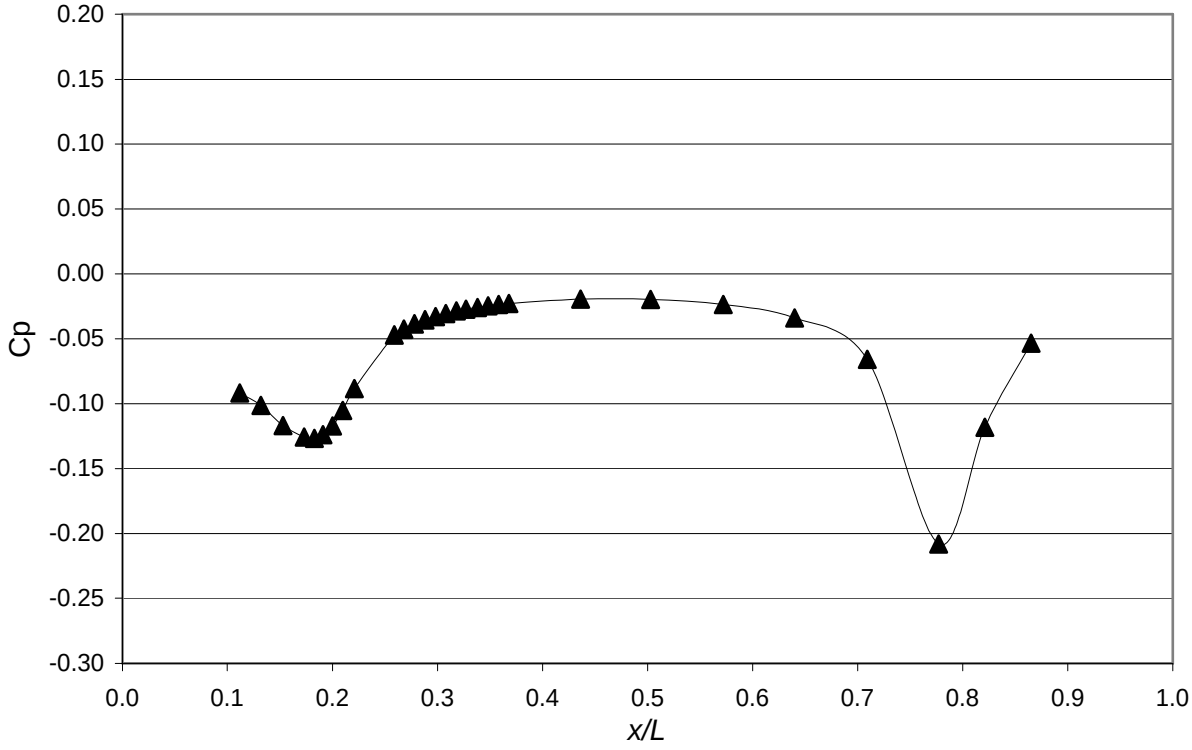

Figure 5.69: C_p vs. x/L distribution obtained from RANS code at $0\,^\circ$ angle of attack.

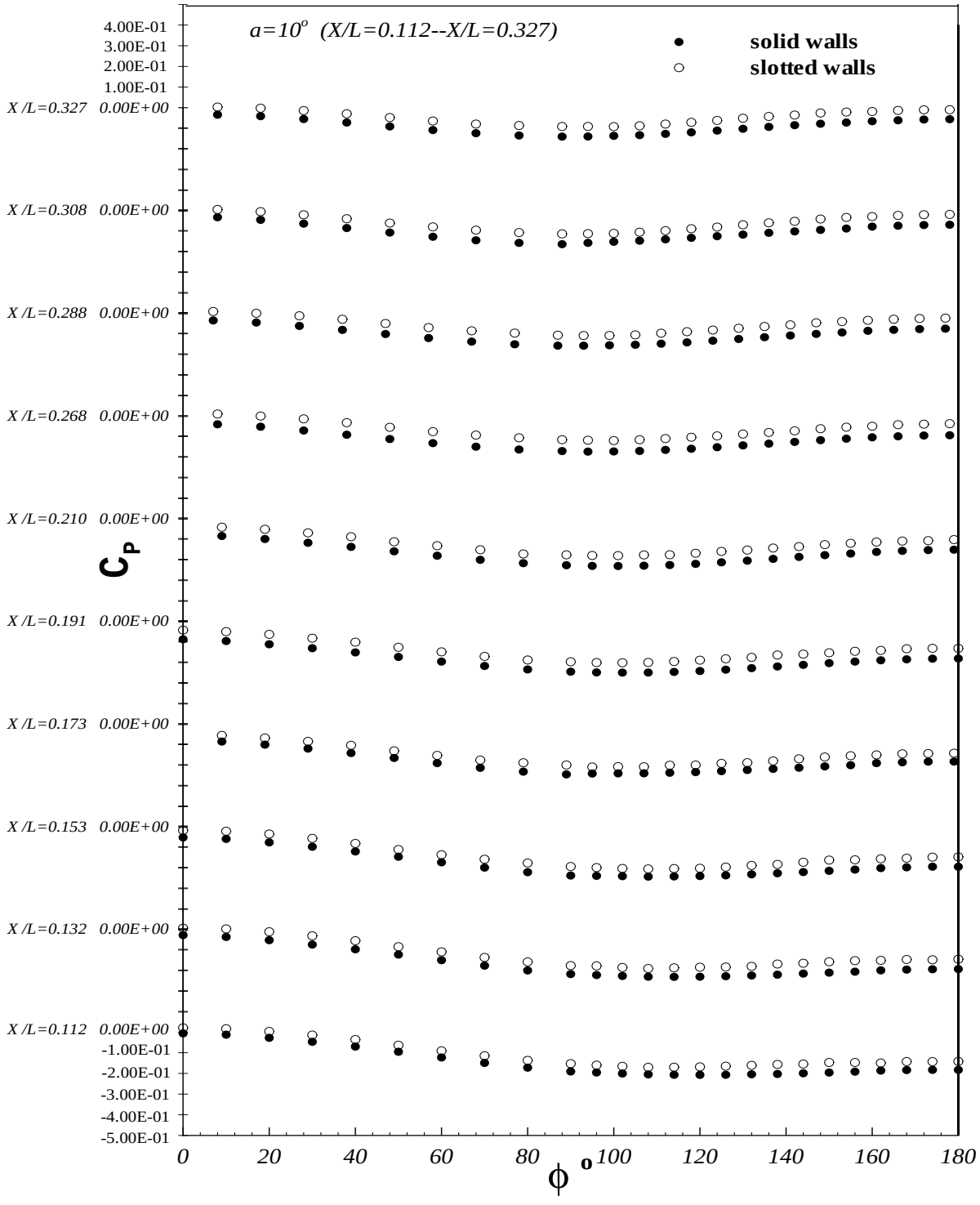

Figure 5.70: C_p vs. ϕ for the stations between $x/L = 0.112$ and $x/L = 0.327$ at $\alpha = 10.0\,^\circ$ for the barebody case. Solid and slotted wind tunnel wall configurations.

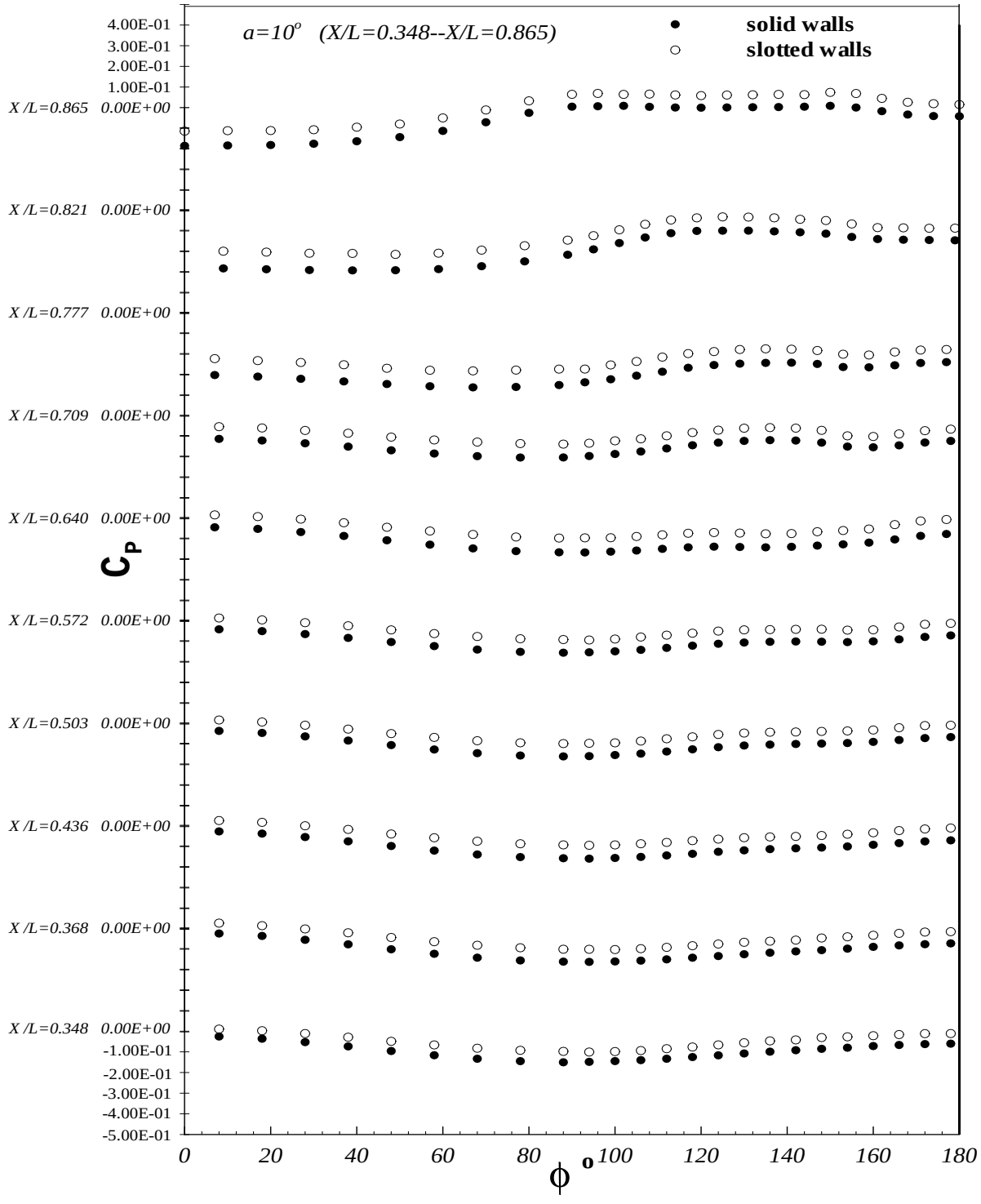

Figure 5.71: C_p vs. ϕ for the stations between $x/L = 0.348$ and $x/L = 0.865$ at $\alpha = 10.0\,^\circ$ for the barebody case. Solid and slotted wind tunnel wall configurations.

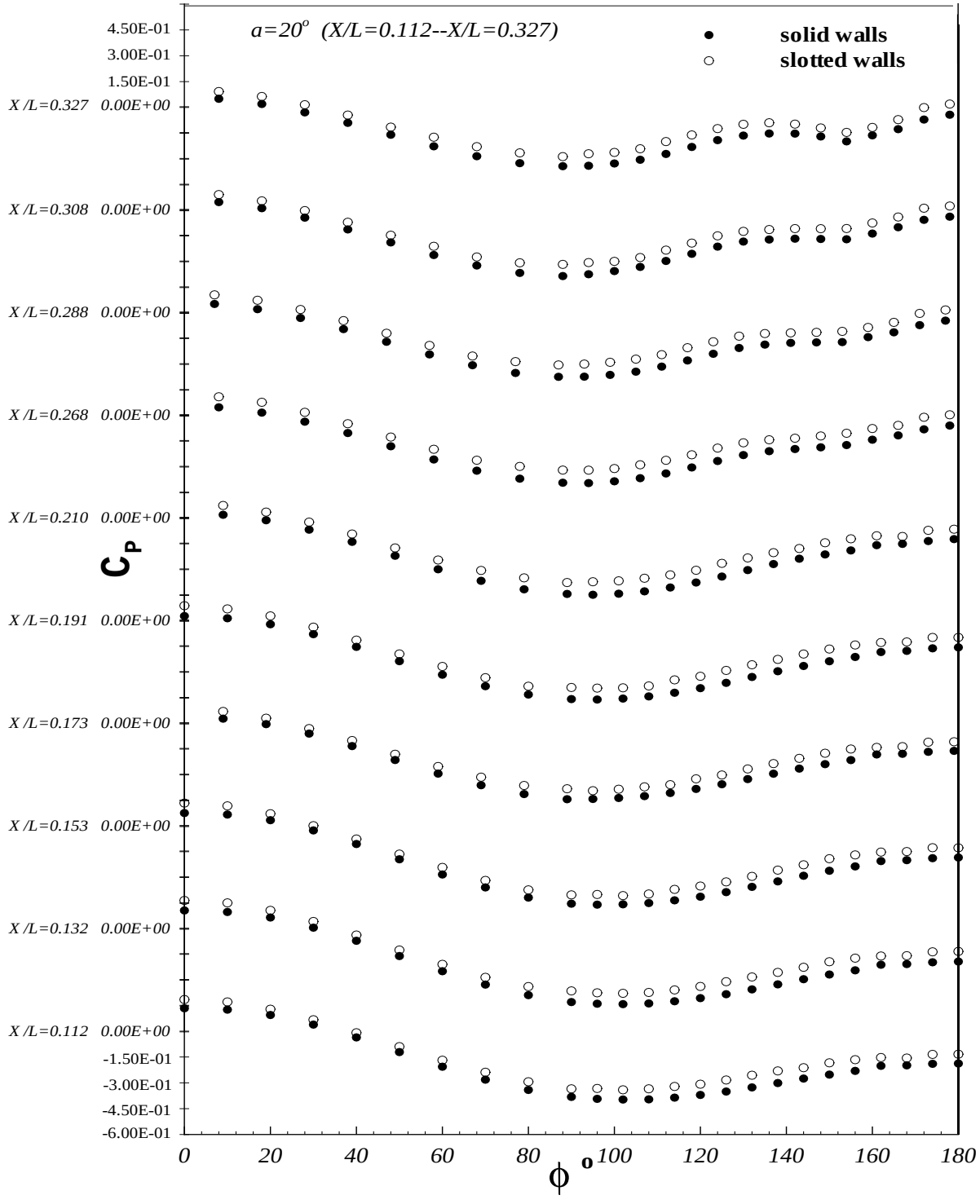

Figure 5.72: C_p vs. ϕ for the stations between $x/L = 0.112$ and $x/L = 0.327$ at $\alpha = 20.0\,^\circ$ for the barebody case. Solid and slotted wind tunnel wall configurations.

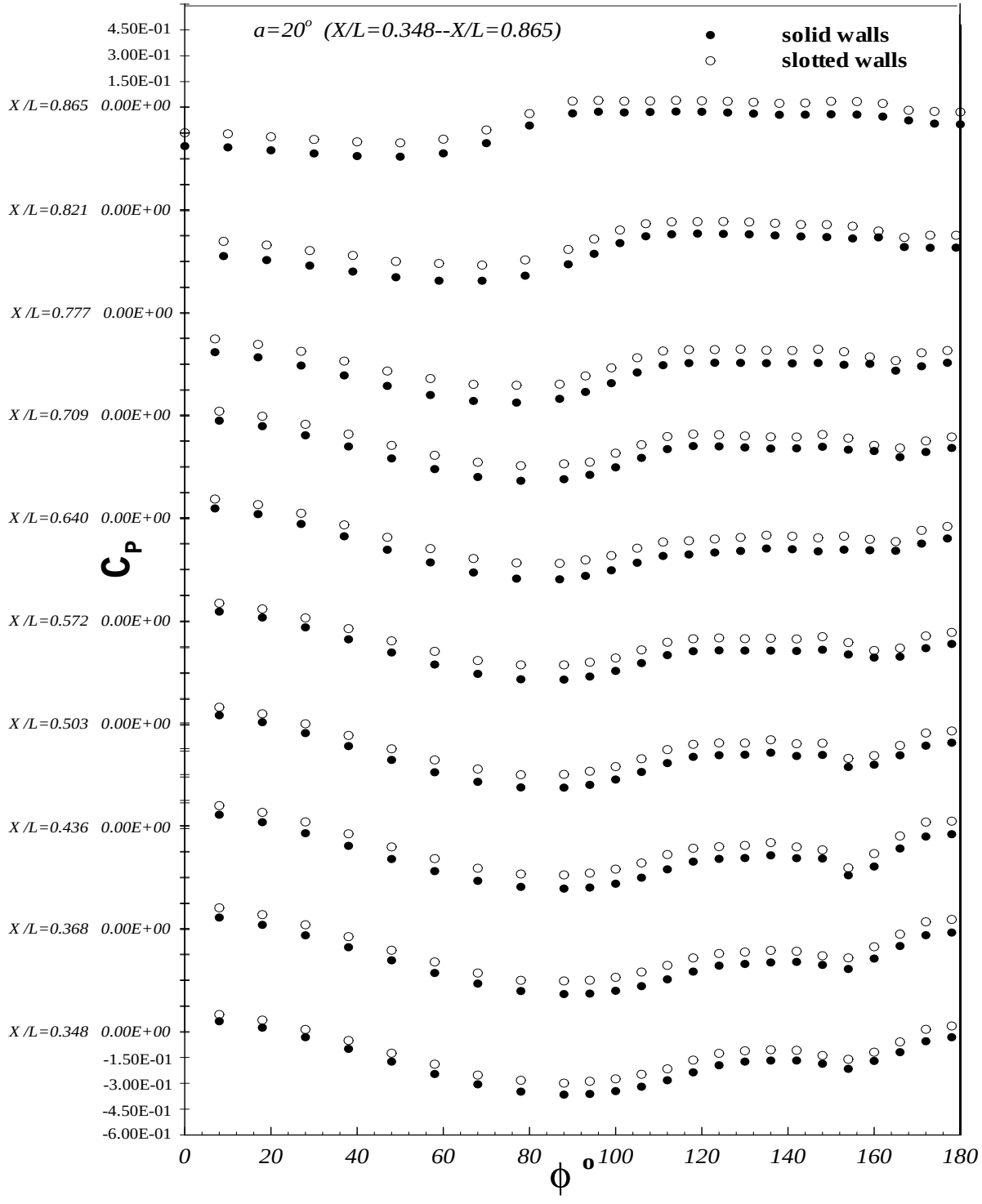

Figure 5.73: C_p vs. ϕ for the stations between $x/L = 0.348$ and $x/L = 0.865$ at $\alpha = 20.0\,^\circ$ for the barebody case. Solid and slotted wind tunnel wall configurations.

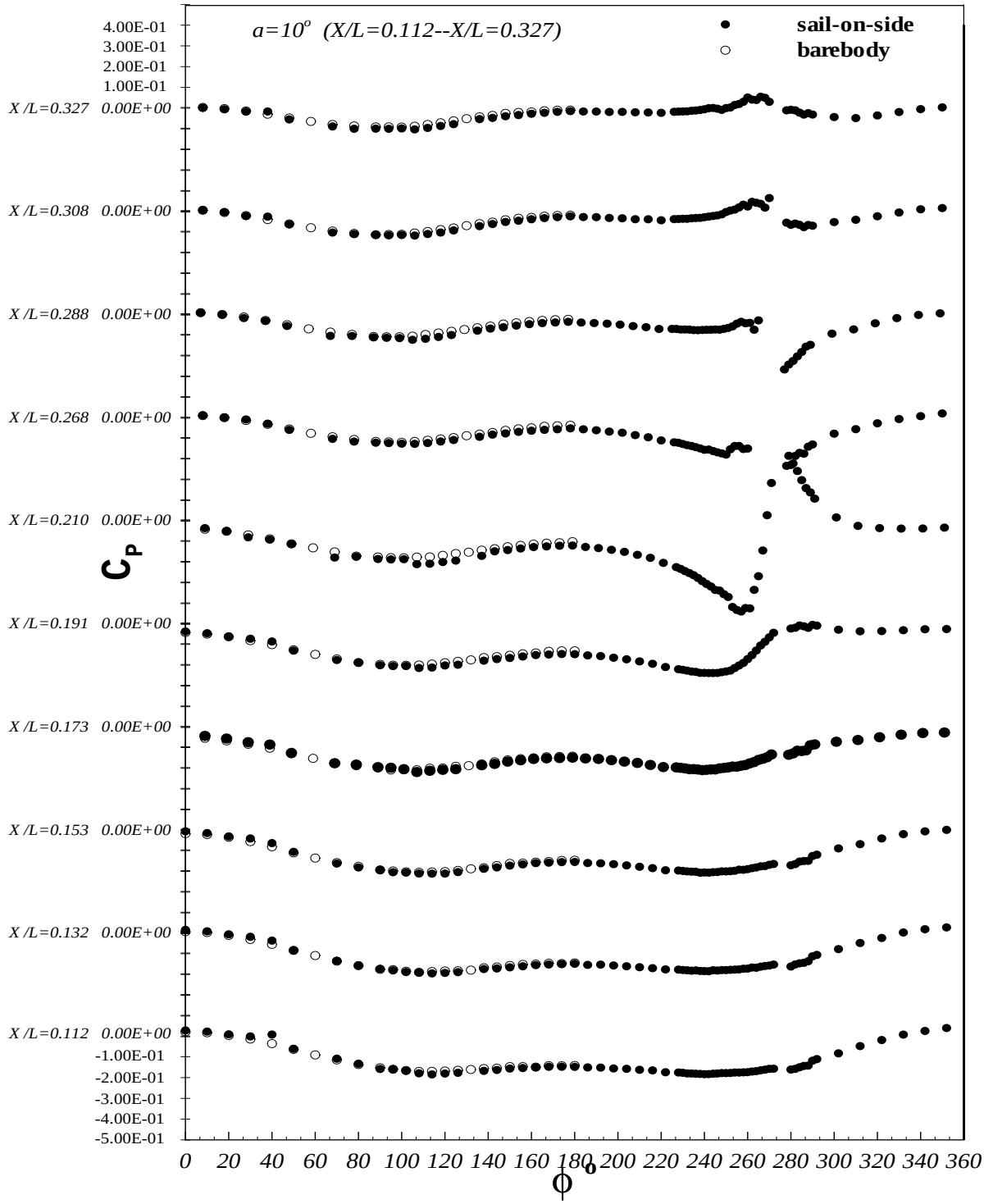

Figure 5.74: C_p vs. ϕ for the stations between $x/L = 0.112$ and $x/L = 0.327$ at $\alpha = 10.0\,^\circ$ for the barebody case and sail-on-side cases. Sail side on the right of the figure starting from $\phi = 180\,^\circ$. Slotted wind tunnel wall configuration.

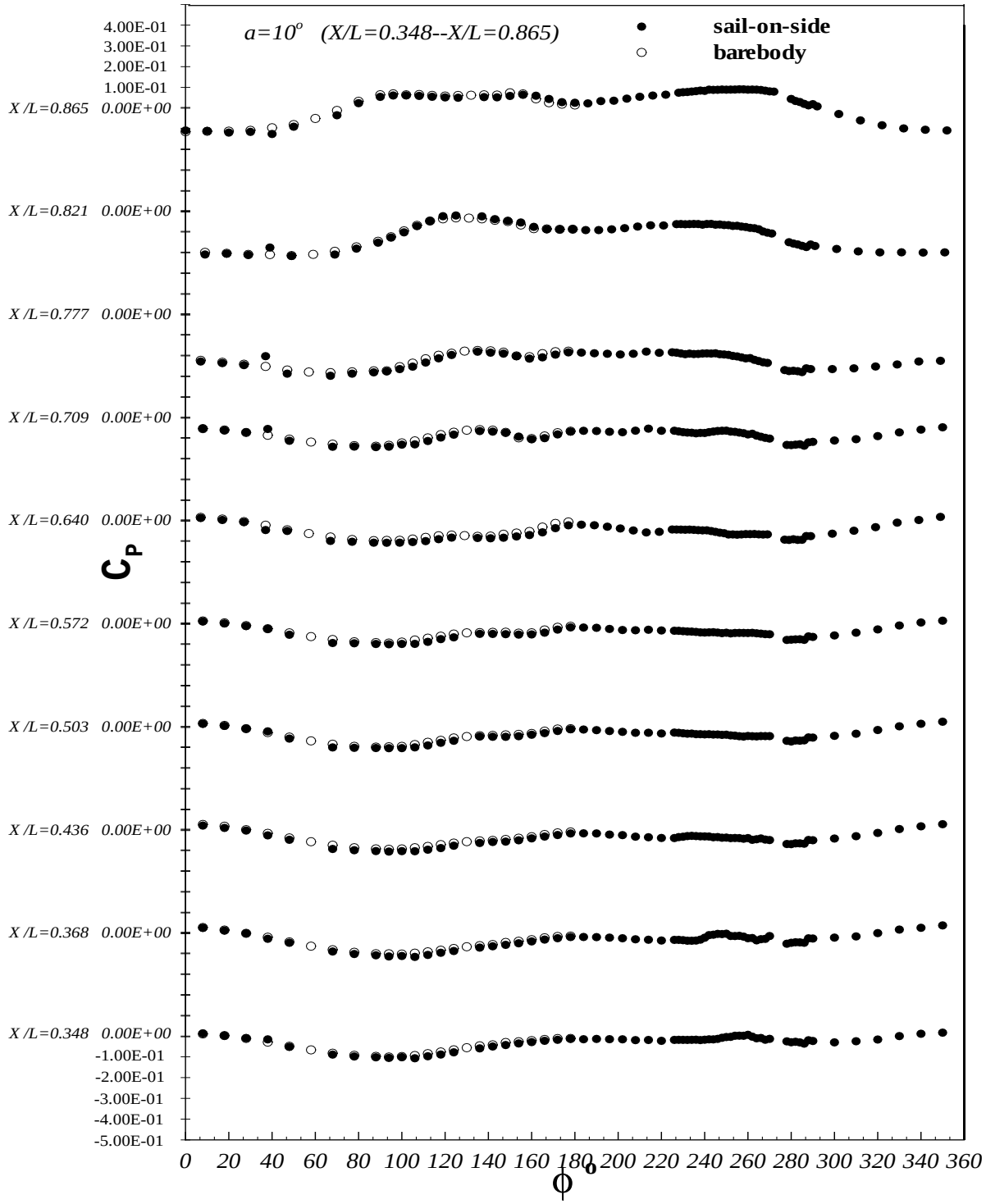

Figure 5.75: C_p vs. ϕ for the stations between $x/L = 0.348$ and $x/L = 0.865$ at $\alpha = 10.0\,^\circ$ for the barebody case and sail-on-side cases. Sail side on the right of the figure starting from $\phi = 180\,^\circ$. Slotted wind tunnel wall configuration.

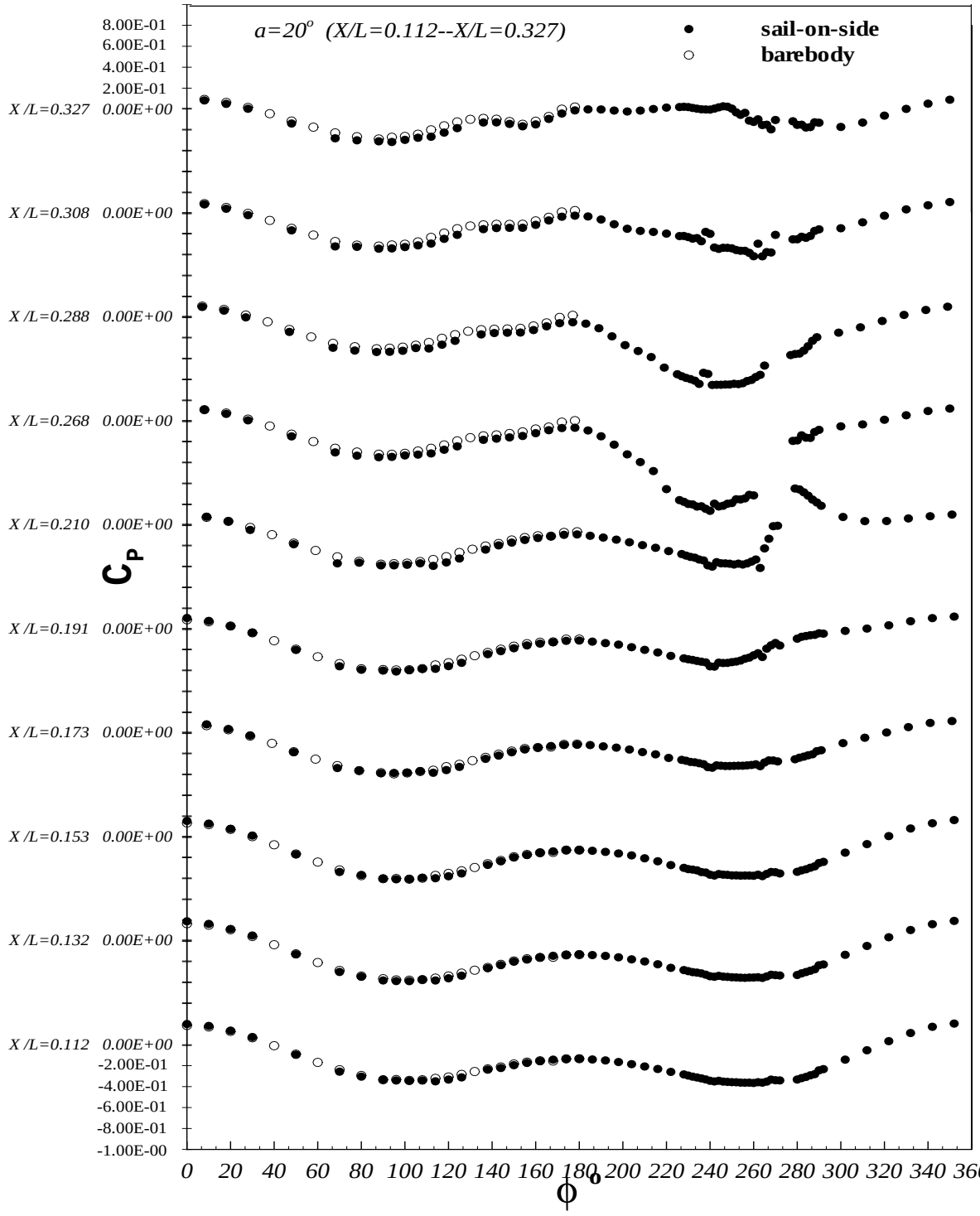

Figure 5.76: C_p vs. ϕ for the stations between $x/L = 0.112$ and $x/L = 0.327$ at $\alpha = 20.0\,^\circ$ for the barebody case and sail-on-side cases. Sail side on the right of the figure starting from $\phi = 180\,^\circ$. Slotted wind tunnel wall configuration.

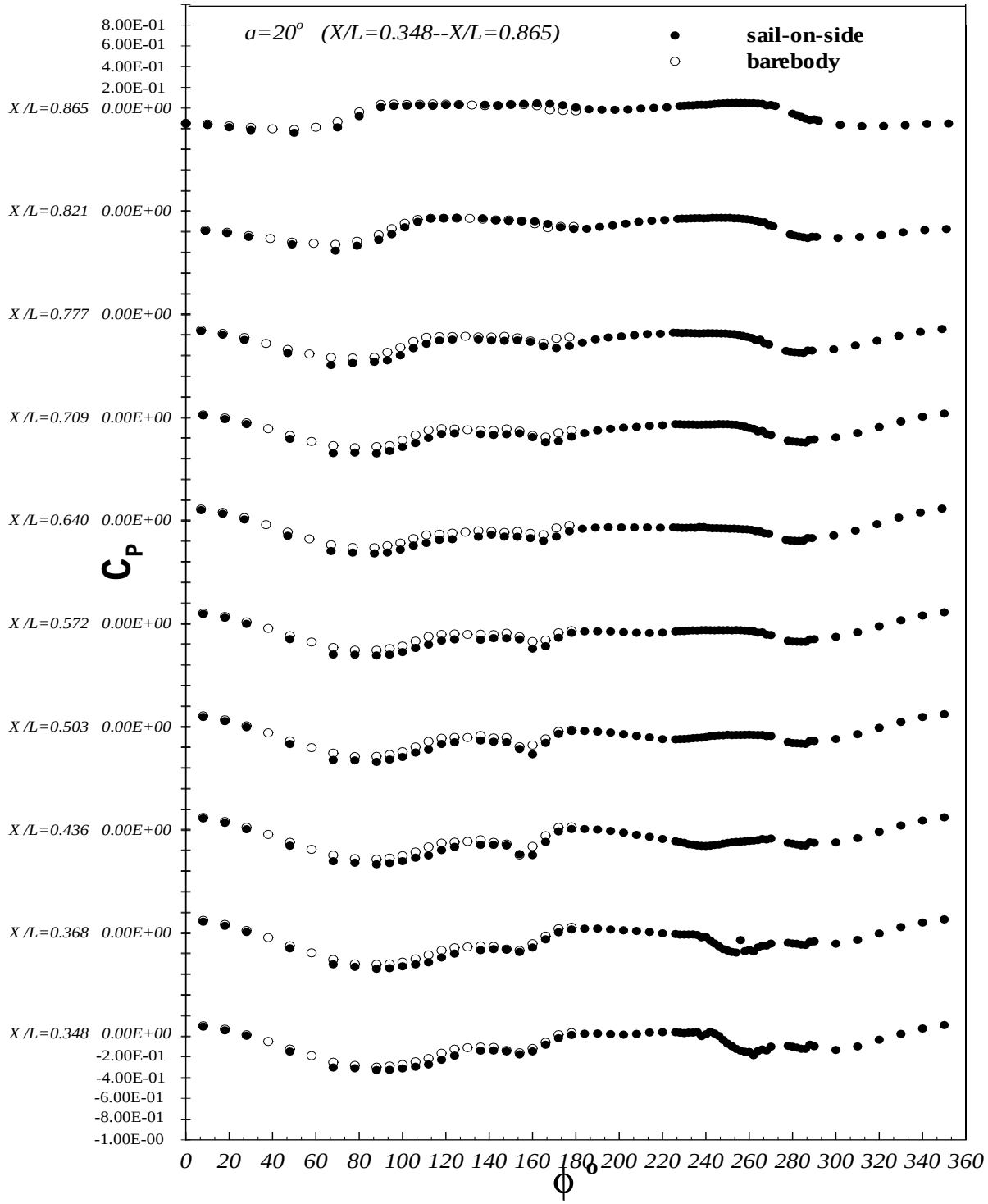

Figure 5.77: C_p vs. ϕ for the stations between $x/L = 0.348$ and $x/L = 0.865$ at $\alpha = 20.0\,^\circ$ for the barebody case and sail-on-side cases. Sail side on the right of the figure starting from $\phi = 180\,^\circ$. Slotted wind tunnel wall configuration.

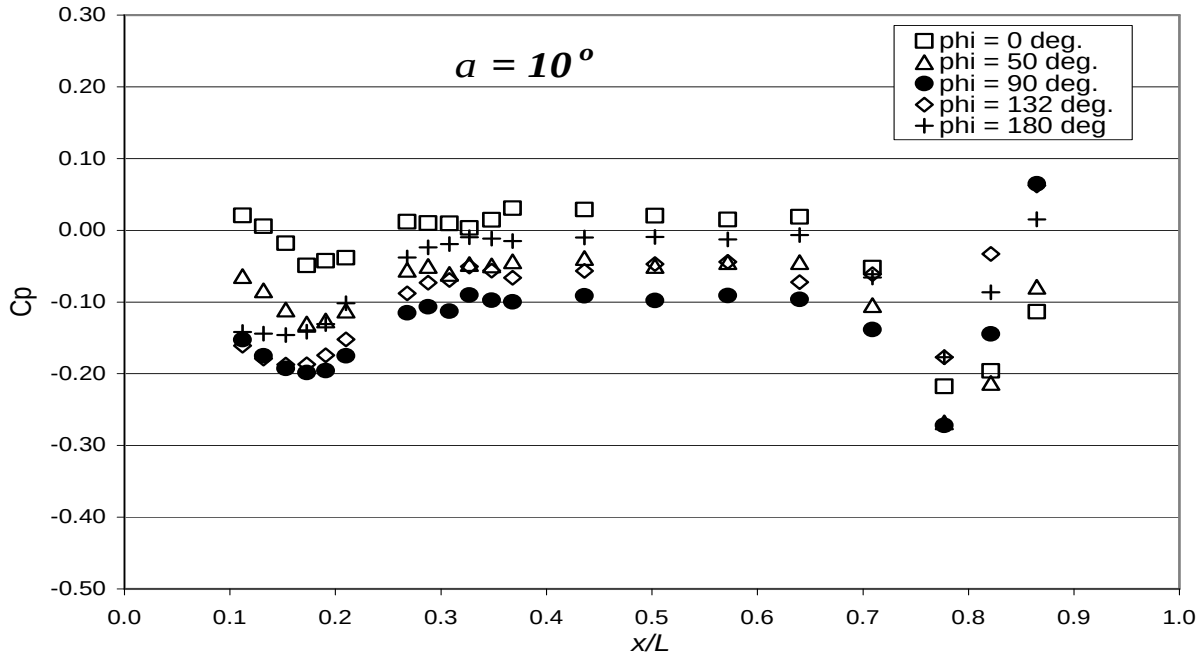

Figure 5.78: Barebody C_p vs. x/L distributions for different ϕ locations at $\alpha = 10\,^\circ$.

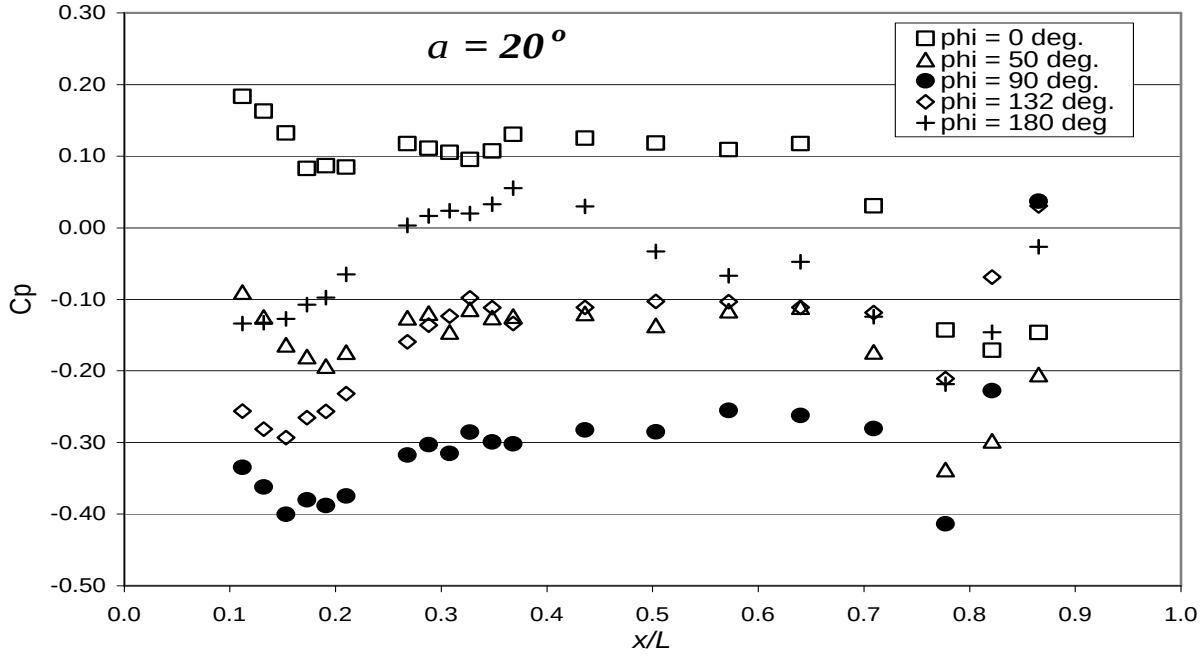

Figure 5.79: Barebody C_p vs. x/L distributions for different ϕ locations at $\alpha = 20\,^\circ$.

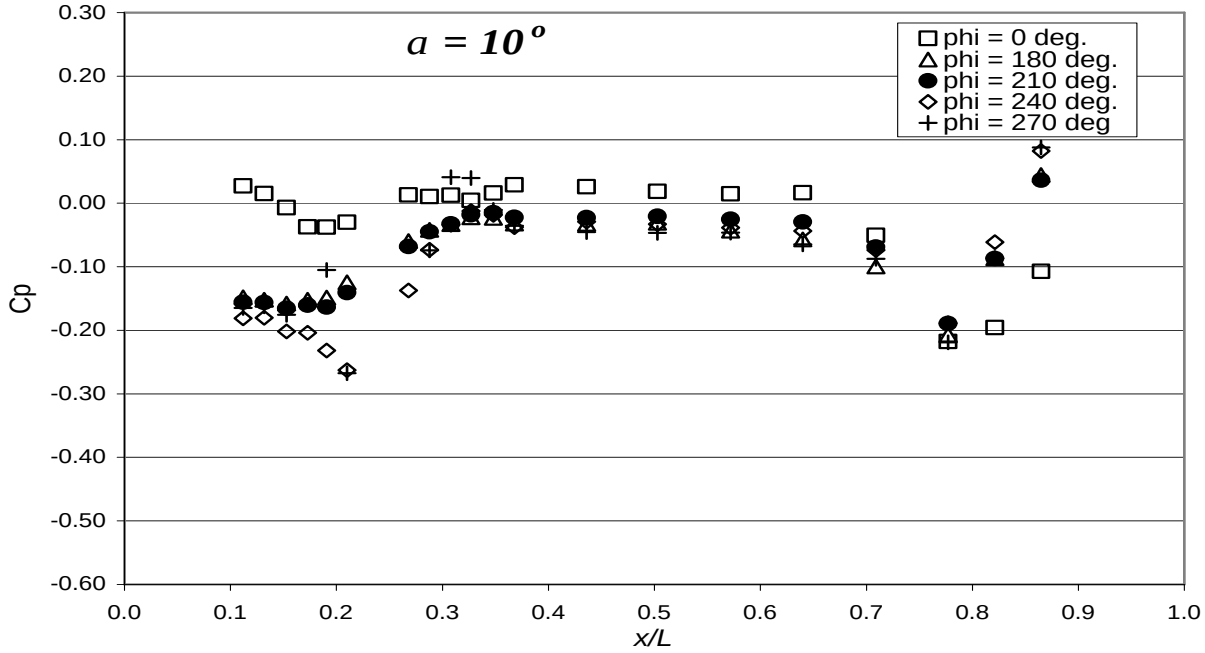

Figure 5.80: Sail-on-side C_p vs. x/L distributions for different ϕ locations at $\alpha = 10\,^\circ$.

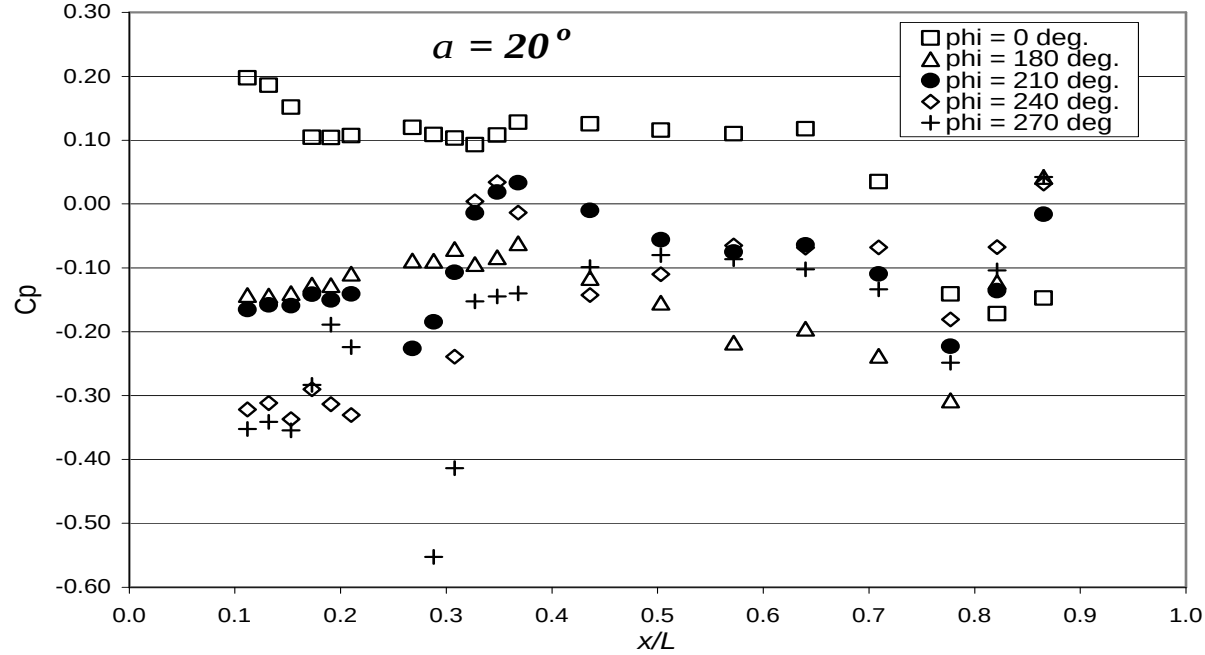

Figure 5.81: Sail-on-side C_p vs. x/L distributions for different ϕ locations at $\alpha = 20\,^\circ$.

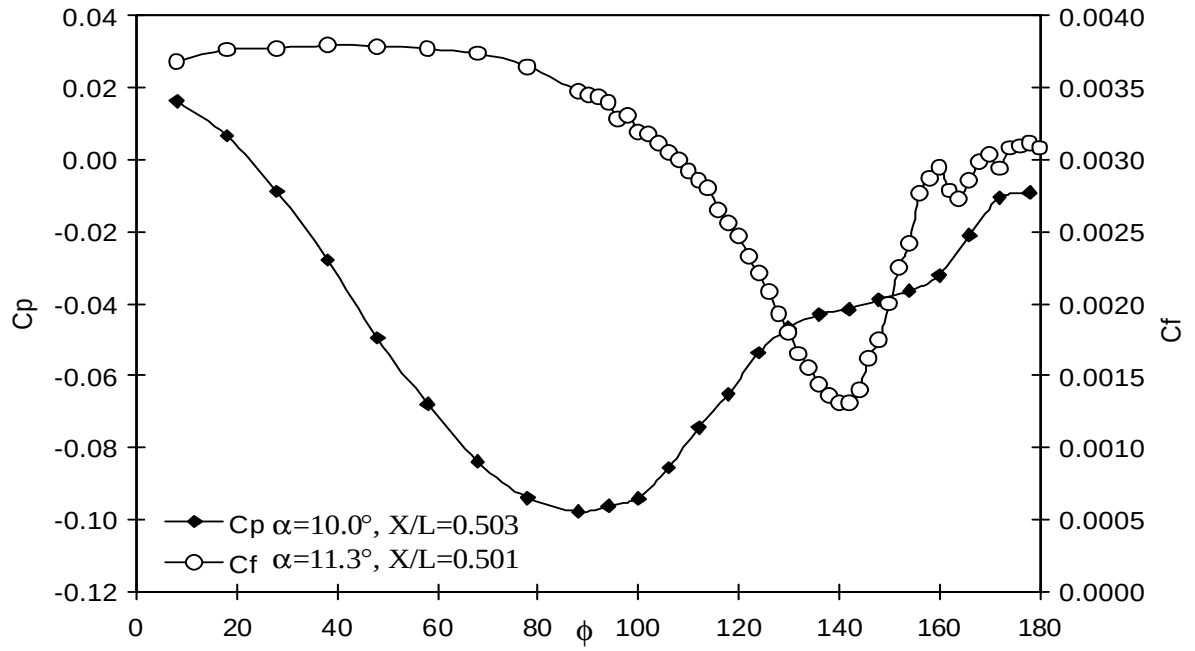

Figure 5.82: Steady C_p and C_f vs. ϕ for the barebody case. For C_p measurements $\alpha = 10.0°$ and $x/L = 0.503$. For C_f measurements $\alpha = 11.3\,°$ and $x/L = 0.501$.

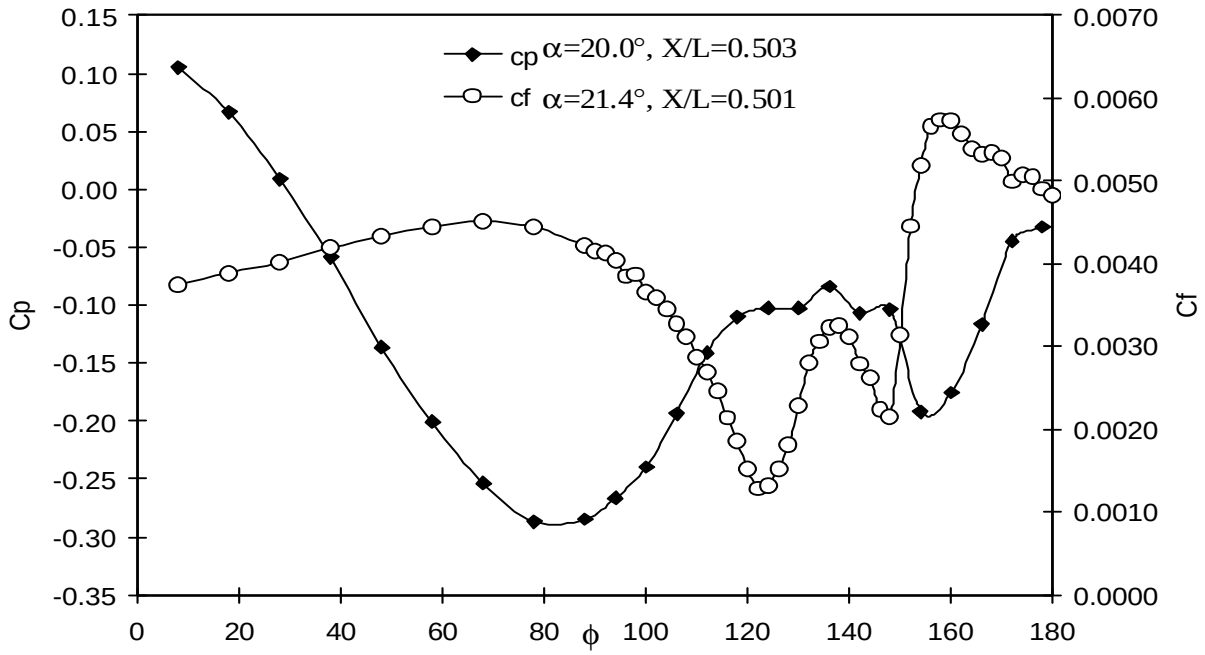

Figure 5.83: Steady C_p and C_f vs. ϕ for the barebody case. For C_p measurements $\alpha = 20.0°$ and $x/L = 0.503$. For C_f measurements $\alpha = 21.4\,°$ and $x/L = 0.501$.

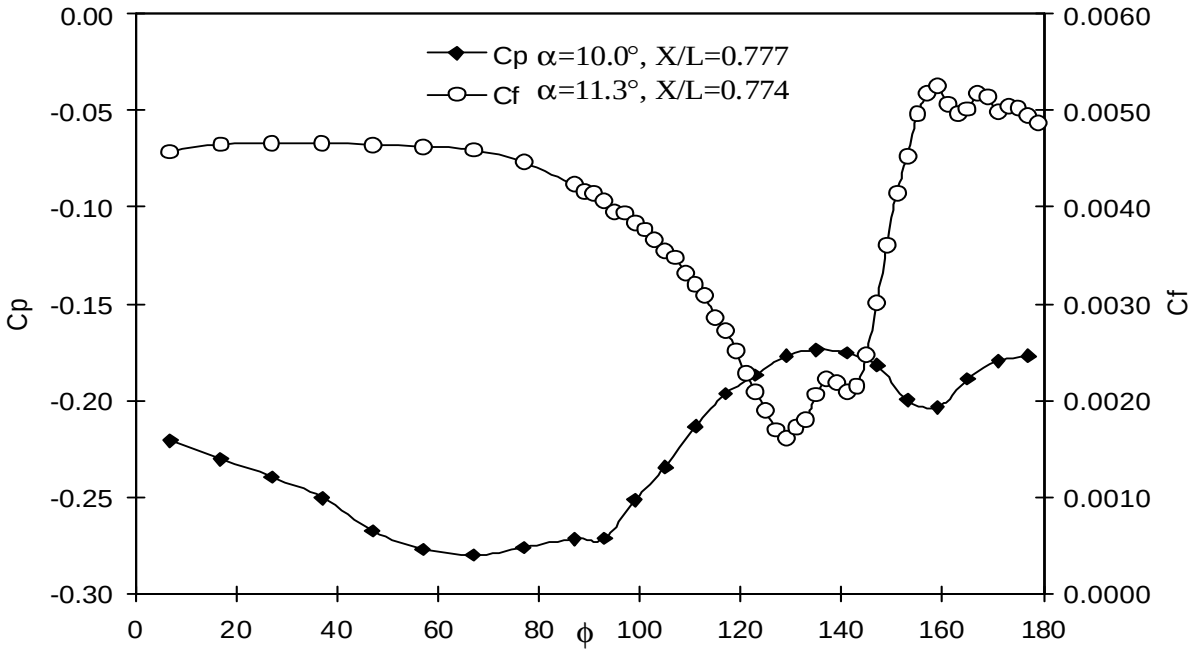

Figure 5.84: Steady C_p and C_f vs. ϕ for the barebody case. For C_p measurements $\alpha = 10.0°$ and $x/L = 0.777$. For C_f measurements $\alpha = 11.3\,°$ and $x/L = 0.774$.

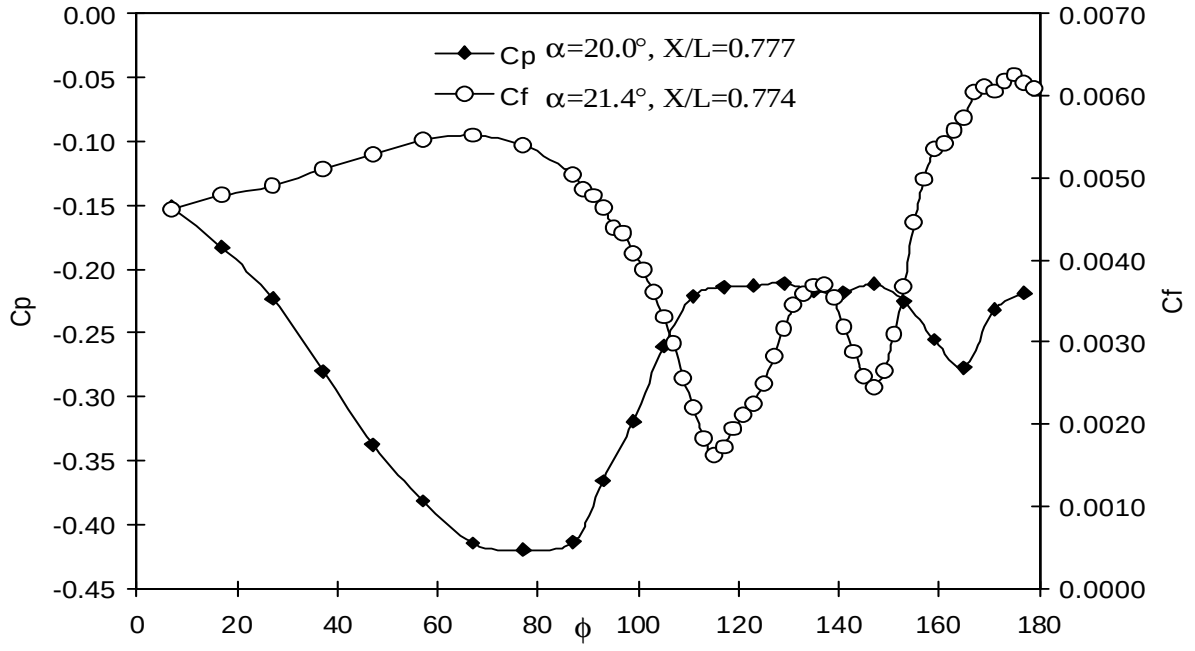

Figure 5.85: Steady C_p and C_f vs. ϕ for the barebody case. For C_p measurements $\alpha = 20.0°$ and $x/L = 0.777$. For C_f measurements $\alpha = 21.4\,°$ and $x/L = 0.774$.

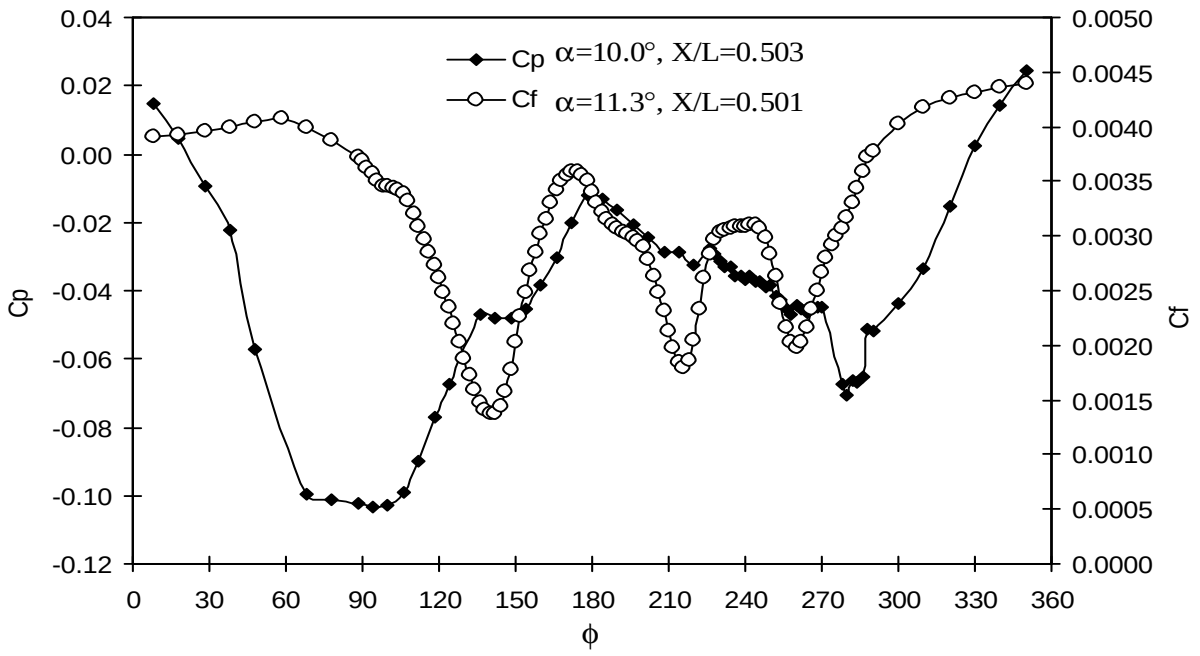

Figure 5.86: Steady C_p and C_f vs. ϕ for the sail-on-side case. For C_p measurements $\alpha = 10.0\,^\circ$ and $x/L = 0.503$. For C_f measurements $\alpha = 11.3\,^\circ$ and $x/L = 0.501$.

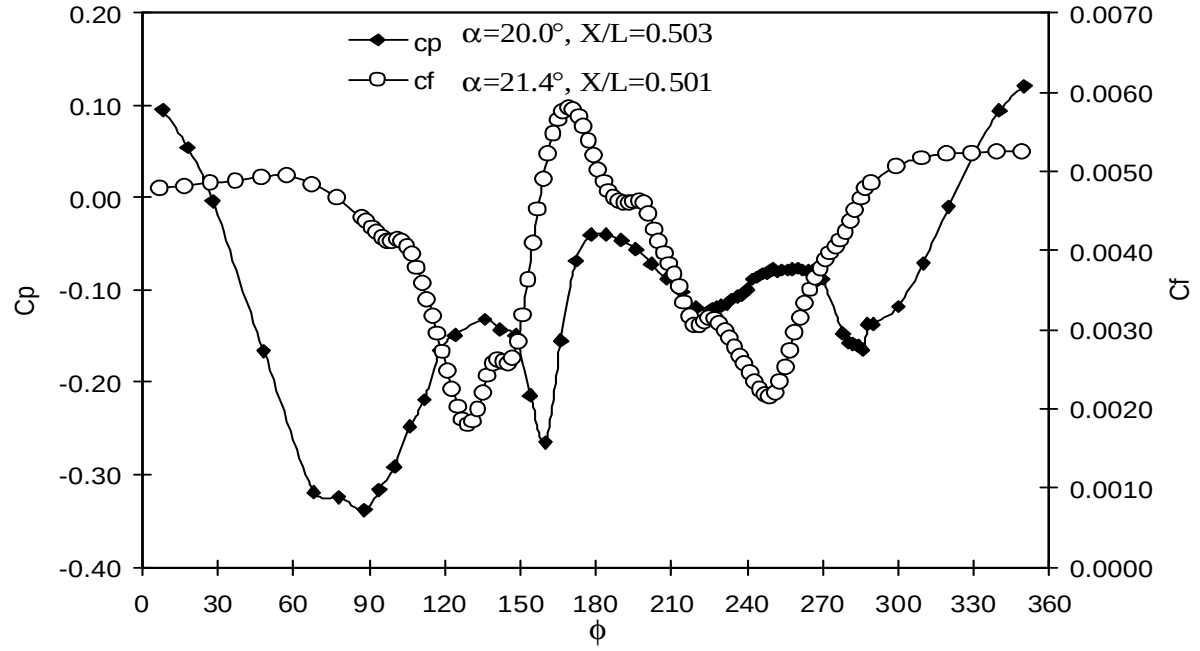

Figure 5.87: Steady C_p and C_f vs. ϕ for the sail-on-side case. For C_p measurements $\alpha = 20.0\,^\circ$ and $x/L = 0.503$. For C_f measurements $\alpha = 21.4\,^\circ$ and $x/L = 0.501$.

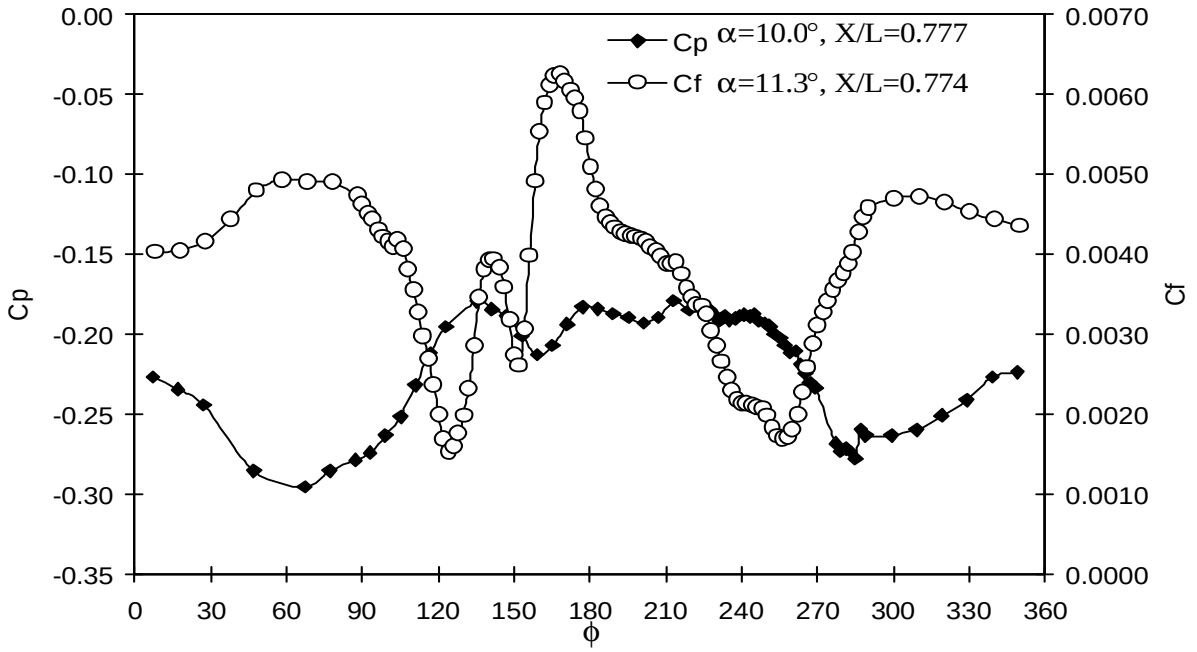

Figure 5.88: Steady C_p and C_f vs. ϕ for the sail-on-side case. For C_p measurements $\alpha = 10.0\,^\circ$ and $x/L = 0.777$. For C_f measurements $\alpha = 11.3\,^\circ$ and $x/L = 0.774$.

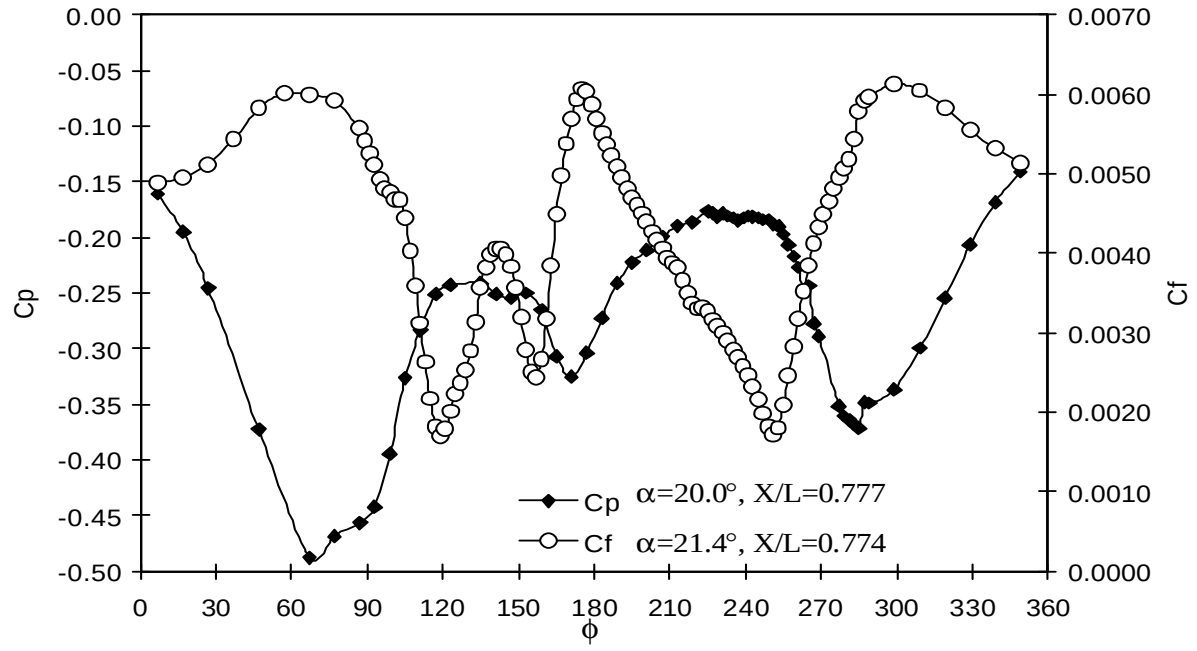

Figure 5.89: Steady C_p and C_f vs. ϕ for the sail-on-side case. For C_p measurements $\alpha = 20.0\,^\circ$ and $x/L = 0.777$. For C_f measurements $\alpha = 21.4\,^\circ$ and $x/L = 0.774$.